Ferroelectricity and magnetoelectric coupling in magnetic ferroelectrics and artificial multiferroic heterostructures

Ignasi Fina Martínez

ADVERTIMENT. La consulta d'aquesta tesi queda condicionada a l'acceptació de les següents condicions d'ús: La difusió d'aquesta tesi per mitjà del servei TDX (**www.tdx.cat**) ha estat autoritzada pels titulars dels drets de propietat intel·lectual únicament per a usos privats emmarcats en activitats d'investigació i docència. No s'autoritza la seva reproducció amb finalitats de lucre ni la seva difusió i posada a disposició des d'un lloc aliè al servei TDX. No s'autoritza la presentació del seu contingut en una finestra o marc aliè a TDX (framing). Aquesta reserva de drets afecta tant al resum de presentació de la tesi com als seus continguts. En la utilització o cita de parts de la tesi és obligat indicar el nom de la persona autora.

ADVERTENCIA. La consulta de esta tesis queda condicionada a la aceptación de las siguientes condiciones de uso: La difusión de esta tesis por medio del servicio TDR (**www.tdx.cat**) ha sido autorizada por los titulares de los derechos de propiedad intelectual únicamente para usos privados enmarcados en actividades de investigación y docencia. No se autoriza su reproducción con finalidades de lucro ni su difusión y puesta a disposición desde un sitio ajeno al servicio TDR. No se autoriza la presentación de su contenido en una ventana o marco ajeno a TDR (framing). Esta reserva de derechos afecta tanto al resumen de presentación de la tesis como a sus contenidos. En la utilización o cita de partes de la tesis es obligado indicar el nombre de la persona autora.

WARNING. On having consulted this thesis you're accepting the following use conditions: Spreading this thesis by the TDX (**www.tdx.cat**) service has been authorized by the titular of the intellectual property rights only for private uses placed in investigation and teaching activities. Reproduction with lucrative aims is not authorized neither its spreading and availability from a site foreign to the TDX service. Introducing its content in a window or frame foreign to the TDX service is not authorized (framing). This rights affect to the presentation summary of the thesis as well as to its contents. In the using or citation of parts of the thesis it's obliged to indicate the name of the author.

Ferroelectricity and magnetoelectric coupling in magnetic ferroelectrics and artificial multiferroic heterostructures

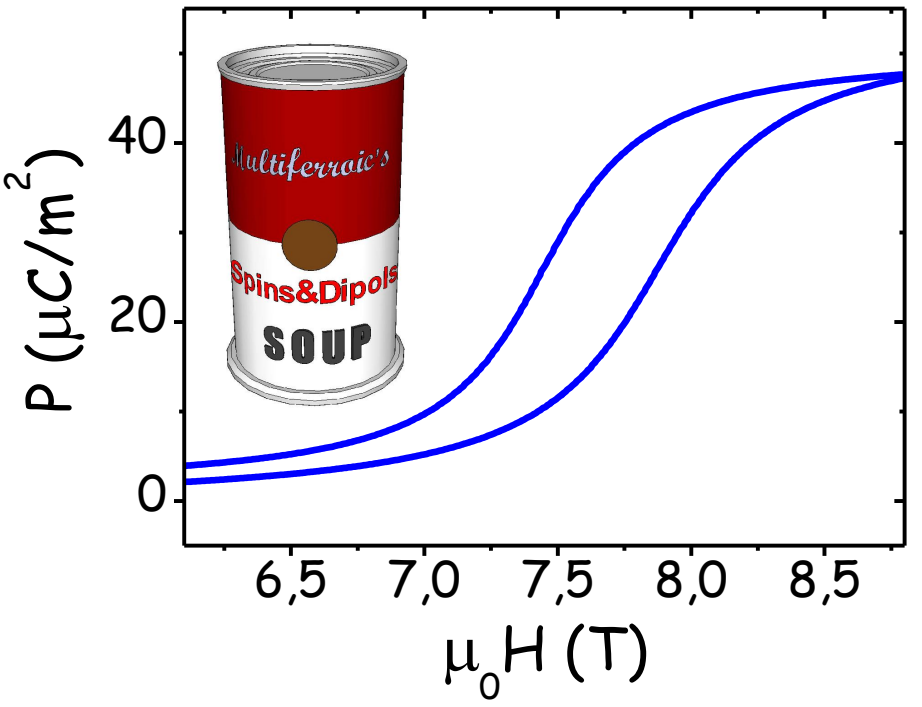

Ignasi Fina

PhD Thesis

2012

ICMAB
CSIC
Consejo Superior de Investigaciones Científicas
UNIVERSITAT DE BARCELONA

Lourdes Fàbrega i **Josep Fontcuberta**, ambdós investigadors del Consejo Superior de Investigaciones Científicas (CSIC) a l'Institut de Ciència de Materials de Barcelona (ICMAB).

CERTIFIQUEN:

Que Ignasi Fina Martínez, llicenciat en Ciències Físiques per la Universitat de Barcelona amb possesió del Màster en Enginyeria Física cursat a la Universitat de Barcelona, ha dut a terme sota la nostra direcció el treball que porta per títol *"Ferroelectricity and magnetoelectric coupling in magnetic ferroelectrics and artificial multiferroic heterostructures"*, i queda recollit en aquesta memòria per optar al grau de Doctor en Física per la Universitat de Barcelona.

I perquè així consti, signen el present certificat:

Dra. Lourdes Fàbrega
Co-directora

Prof. Josep Fontcuberta
Co-director

De la mateixa manera, **Cesar Ferrater**, professor titular de la Universitat de Barcelona, com a tutor de la present tesi, signa el present certificat:

Dr. Cesar Ferrater
Tutor

L'interessat,

Barcelona, 14 de març de 2012

Ferroelectricity and magnetoelectric coupling in magnetic ferroelectrics and artificial multiferroic heterostructures

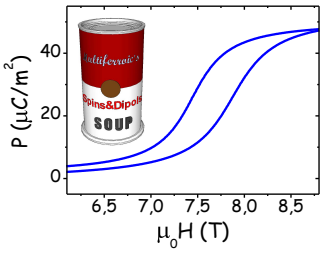

A thesis submitted in fulfilment of the requirements

for the degree of Doctor of Philosophy in Physics

Universitat de Barcelona, 2012

Ignasi Fina

Insitut de Ciència de Materials de Barcelona

Consejo Superior de Investigaciones Científicas

Spain

Als que hi eren, als que hi seran.

Abstract

Multiferroic materials are those materials in which more than one ferroic order coexist. The most technologically appealing multiferroic materials are those showing ferromagnetism and ferroelectricity. Coupling between the mentioned ferroic orders, called magnetoelectric coupling, can yield to new interesting functional applications. In spintronics this coupling would result in the possibility of building magnetic memories controlled by electric field, or transistors where charge is contact-less controlled by a magnetic field.

The ultimate goal of the present thesis is to explore the control of the ferroelectric polarization and dielectric properties by magnetic field in thin films. To that purpose dielectric, ferroelectric and magnetoelectric characterization methods of different multiferroic materials have been developed and used.

Two big groups of multiferroic materials can be found. On one hand, single-phase multiferroics are those that intrinsically display multiferroicity. On the other hand, multiferroic composites are those where multiferroicity results from the mixture of two different materials that display ferroelectric and ferromagnetic order separately.

Single-phase multiferroics can be divided in two subgroups: those where ferroic orders have different sources and those, called magnetic ferroelectrics, where magnetic order induces ferroelectricity and, consequently, larger magnetoelectric coupling is expected.

The single-phase multiferroic material studied in the present thesis is $YMnO_3$ in its orthorhombic phase, and it belongs to the magnetic ferroelectrics

family. Even though it shows collinear magnetic order in bulk, we will show that cycloidal order in thin film form can be stabilized, giving rise to the capability of controlling the ferroelectric polarization by magnetic field in a reversible manner.

Multiferroic composite thin films can be built mainly in two different architectures: vertical (ferromagnetic/ferroelectric columns embedded in a ferroelectric/ferromagnetic matrix) and horizontal (multilayered structures alternating ferromagnetic and ferroelectric materials). Here we compare both, using a ferroelectric perovskite ($BaTiO_3$) and a ferromagnetic spinel ($CoFe_2O_4$). We will show that horizontal heterostructures display better ferroelectric properties and larger magnetoelectric coupling, compared to vertical heterostructures, where leakage current is a limiting parameter. The control of dielectric/ferroelectric properties under appropriate heterostructure configuration (in horizontal heterostructures) or deposition conditions (in vertical heterostructures) has been also achieved.

Resum

Els materials multiferroics són aquells materials en què coexisteix més d'un ordre ferroic. D'aquests els més interessants són els que presenten ferromagnetisme i ferroelectricitat. La presencia d'acoblament entre aquests dos ordres ferroics, anomenat acoblament magnetoelectric, obre un nou camp d'aplicacions. En spintrònica, aquest acoblament significaria poder construir memòries magnètiques controlades mitjançant camp elèctric, o transistors on la càrrega es controlaria mitjançant camp magnètic.

L'objectiu final d'aquesta tesi és explorar el control de la polarització ferroelèctrica mitjançant camp magnètic en capes fines. Amb aquesta finalitat, s'han utilitzat mètodes de caracterització dielèctrica, ferroelèctrica i magnetoelèctrica en diferents materials multiferroics en capa fina.

Existeixen dos grans grups de materials multiferroics. D'una banda, els materials de fase única són aquells que presenten multiferroïcitat de manera intrínseca. D'altra banda, els multiferroics de fase mixta són aquells en els quals la multiferroïcitat és resultat de la barreja de dos materials diferents que presenten ordre ferroelèctric i ferromagnètic per separat.

Els materials de fase única es poden dividir en dos subgrups: aquells en què els ordres ferroics tenen diferent origen i aquells, anomenats ferroelèctrics magnètics, en què l'ordre magnètic indueix ferroelectricitat i, de manera conseqüent, s'espera un major acoblament magnetoelèctric.

El material multiferroic de fase única estudiat en la present tesi és la o-$YMnO_3$ en la seva fase ortoròmbica que pertany a la família dels ferroelèctrics

magnètics. Tot i que presenta ordre magnètic col·lineal en forma màssica, mostrarem que es pot estabilitzar l'odre cicloïdal en capa fina, permetent el control de la polarització ferroelèctrica mitjançant camp magnètic de manera reversible.

Els multiferroics de fase mixta en capa fina es poden créixer utilitzant principalment dues arquitectures diferents: vertical (les columnes ferromagnètiques/ferroelèctriques en una matriu ferroelèctrica/ferromagnètica) i horitzontal (estructures multicapa alternant materials ferromagnètics i ferroelèctrics). Aquí comparem aquestes dues arquitectures, utilitzant una perovskita ferroelèctrica ($BaTiO_3$) i una espinela ferromagnètica ($CoFe_2O_4$). Demostrarem que les heteroestructures horitzontals presenten millors propietats ferroelèctriques i un major acoblament magnetoelèctric comparades amb les heteroestructures verticals, en les quals el corrent de pèrdues sembla ser un paràmetre limitant. També s'han aconseguit controlar les propietats dielèctriques/ferroelèctriques mitjançant la modificació de la configuració en les heteroestructures horitzontals o mitjançant la modificació de les condicions de dipòsit en heteroestructures verticals.

Resumen

Los materiales multiferroicos son aquellos en los que coexiste más de un orden ferroico. DE estos los más interesantes son los que presentan ferromagnetismo y ferroelectricidad. Su acoplamiento, llamado acoplamiento magnetoeléctrico, puede permitir la aplicación de nuevas funcionalidades en el campo de la tecnología. En espintrónica, este acoplamiento significaría poder construir memorias magnéticas controladas mediante campo eléctrico, o transistores donde la carga se controlaría mediante campo magnético.

El objetivo final de esta tesis es explorar el control de la polarización ferroeléctrica mediante campo magnético en capas finas. Con este fin, se han utilizado métodos de caracterización dieléctrica, ferroeléctrica y magnetoeléctrica en diferentes materiales multiferroicos en capa fina.

Existen dos grandes grupos de materiales multiferroicos. Por un lado, los materiales de fase única son aquellos que presentan multiferroicidad de forma intrínseca. Por otro lado, los multiferroicos de fase mixta son aquellos en los cuales la multiferroicidad es el resultado de la mezcla de dos materiales diferentes que presentan orden ferroeléctrico y ferromagnético por separado.

Los materiales de fase única se pueden dividir en dos subgrupos: aquellos en los que los órdenes ferroicos tienen diferente origen y aquellos llamados ferroeléctricos magnéticos en los que el orden magnético induce ferroelectricidad y, por consiguiente, se espera un mayor acoplamiento magnetoeléctrico.

El material multiferroico de fase única que se ha estudiado en esta tesis es la o-$YMnO_3$ en su fase ortorrómbica y pertenece a la familia de los

ferroeléctricos magnéticos. Aunque presenta orden magnético colineal en forma másica, mostraremos que se puede estabilizar el orden cicloidal en capa fina, permitiendo el control de la polarización ferroeléctrica mediante campo magnético de forma reversible.

Los multiferroicos de fase mixta en capa fina se pueden crecer utilizando principalmente dos arquitecturas diferentes: vertical (las columnas ferromagnéticas/ferroeléctricas en una matriz ferroeléctrica/ferromagnética) y horizontal (estructuras multicapa alternando materiales ferromagnéticos y ferroeléctricos). Aquí comparamos ambas, utilizando una perovskita ferroeléctrica ($BaTiO_3$) y una espinela ferromagnética ($CoFe_2O_4$). Demostraremos que las heteroestructuras horizontales presentan mejores propiedades ferroeléctricas y un mayor acoplamiento magnetoeléctrico comparadas con las heteroestructuras verticales, en las cuales la corriente de pérdidas parece ser un parámetro limitante. También se han conseguido controlar las propiedades dieléctricas/ferroeléctricas mediante el cambio de configuración en heteroestructuras horizontales o mediante el cambio de las condiciones de deposito en heteroestructuras verticales.

Acknowledgments

En primer lloc, un agraïment especial als meus directors de tesi, la Dra. Lourdes Fàbrega i el Prof. Josep Fontcuberta. No només els vull agrair l'oportunitat d'entrar al món de la recerca científica i el seu treball durant de supervisió de la meva tesi doctoral. Sobretot, vull destacar que gràcies a ells ara veig que un camí d'oportunitats s'obre davant meu, i que m'han ensenyat que després de més de quatre anys de feina sóc una mica més ignorant del que era al principi.

També vull agrair als meus predecessors en la feina realitzada durant la present tesi: Dr. Xavier Martí i Nico Dix. No només perquè ells m'han proporcionat el material indispensable per a realitzar la tesi (les mostres), i no només perquè han realitzat gran part de la caracterització estructural i magnètica, sinó perquè les nostres discussions ens han permès entendre millor els nostres problemes i per tant ens han ajudat a anar més enllà de les conclusions que podríem haver obtingut per seperat. De la mateixa manera, vull agrair la feina del seu supervisor de tesi, el Dr. Florencio Sánchez, la presència del qual ha estat indispensable a l'hora d'obtenir mostres d'alta qualitat que m'han permès anar molt lluny en les conclusions de la present tesi.

Vull agrair la disposició del meu tutor de la Universitat de Barcelona, el Dr. Cèsar Ferrater.

Vull agrair la forta implicació que han tingut els meus supervisors, la Lourdes Fàbrega i el Josep Fontcuberta, i el Xavier Martí en l'elaboració de

la present memòria.

I also would like to acknowledge Prof. Vassil Skumryev and Prof. Vladimir Laukhin, from ICREA. I think that working with scientifics like them should be a requirement to obtain the Ph.D. degree. In less intensity but with the right advices, I also would like to acknowledge Prof. Gustau Catalan and Ph.D. Marin Alexe, whose expertise in the field of ferroelectrics has been essential in my learning process.

Essential in this thesis has been Ph.D. David Habrovsky, who helped me in the automation of the measurement system used in the present thesis.

També agrair al Bernat Bozzo, no només pel seu recolzament i ajuda en la modificació dels sistemes del laboratori de baixes temperatures, sinó també per evitar l'avorriment durant les llargues hores de mesura al laboratori de baixes temperatures de l'Institut.

També vull agrair a la gent present i no present al grup de recerca en el qual s'ha realitzat aquesta tesi que no he anomenat ja: Mateusz Scigaj, Ekaterina Khestanova, Diego Gutiérrez, Carles Carrillo, David Pesquera, Ondrej Vlasin, Dr. Franco Rigato, Dr. Michael Foerster, Dra. Ingrid Cañero Infante, Dr. Romain Bachelet, Dr. Miquel Rubio, i Dr. Gervasi Herranz. Amb tots he interactuat, d'una forma o d'una altra, permetent-me aprendre més com a persona i com a intent de científic.

També de la Universitat de Barcelona vull agrair a Eric Langenberg, Jofre Ventura i Emerson Coy, i el seus directors de tesi Dr. Cèsar Ferrater i Prof. Manuel Varela, amb qui he portat a terme enriquidores discussions científiques, i amb els quals he col·laborat estretament en treballs no inclosos en la present tesi.

Acknowledge also the financial support by the Spanish Government (Project Nos. MAT2008-06761-C03, MAT2011-29269-C03, and CSD2007-00041), by the Generalitat de Catalunya (Grant No. 2009-SGR-00376), and by the European Union [Project MaCoMuFi (Grant No. FP6-03321) and FEDER].

Voldria agrair també a nivell personal al Pep i a la Lourdes que, a part d'ensenyar-me infinites coses, també m'hagin ensenyat a ser millor persona en el món del la ciència. Vull agrair els esmorzars amb la Mariona, la Jessica, l'Anna, la Silvia, la Noemí, l'Aura, la Roberta i la Regina; les discussions sobre ciència, política, futbol i... amb el Carlos. A TOTA la gent que he conegut a l'ICMAB i que m'ha ofert moments fantàstics. I als meus amics de Xurruc (groc i negre sempre), especialment al Dídac, al Guiu, i a l'Andreu, i al Xavi i al Xavi.

Finalment, agrair al Cooper, a la Mariona (devoted to) i a l'Encarna, sense els quals simplement res no és possible, i a les persones (passades i futures) a les quals he modestament dedicat el present treball.

Contents

Part I

Introduction

Chapter 1

Introduction

Complex oxides are very appealing materials from a functional point of view, because they can show a wide range of properties: ferroelectricity, ferromagnetism, ferroelasticity, etc. and can be metals, insulators, semiconductors, superconductors, etc. Furthermore, the coupling between some of these properties can give rise to new applications. Perhaps one of the best known examples is magnetoresistance (coupling between conductivity and magnetic order), which has boosted the development of fundamental physics in the frame of spintronics.

Multiferroics are materials in which two or more ferroic orders exist. However, the term multiferroic is usually referred to the materials that display coexistence of magnetic and electric order. In these materials coupling between the different ferroic orders can occur (fig. 1.1), and it is called magnetoelectric coupling. In the presence of magnetoelectric coupling, it is possible to control magnetic properties by electric field [1] and vice versa [2], thus bringing up new possibilities in the field of transducers, sensors, magnetic memories, and other technological applications [3, 4]).

The interplay between electricity and magnetism was demonstrated in 19^{th} century, culminating in Maxwell equations [5, 6]. However, during many years they were considered separately in solid state physics: electronic

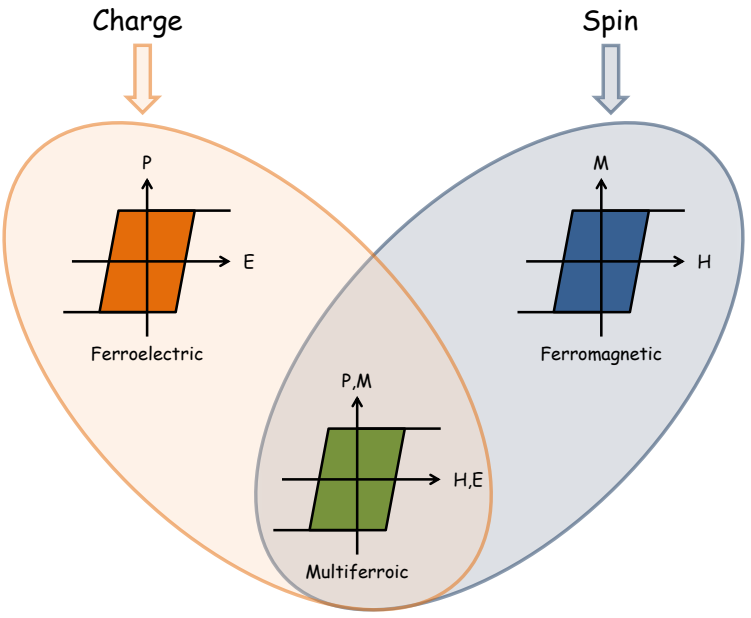

Figure 1.1: *Multiferroics materials are those that present more than one ferroic order. Multiferroics combining ferroelectric (left-orange) and ferromagnetic (right-blue) properties are very appealing materials because the possible presence of magnetoelectric coupling (magnetic control of polarization or electric control of magnetization, bottom-green) can give rise to new technological functionalities.*

charges of ions and electrons were univocally responsible for the electric properties, and spins of the atoms were univocally responsible for the magnetic properties. In 1894, Curie introduced the possibility of intrinsic coupling between magnetic and electric properties on the basis of magnetic symmetry reasons [7]. Conceptually "magnetoelectric" coupling was introduced in 1926 by Debye [8]. In 1959 Landau and Lifshitz stated that linear coupling between magnetic and electric orders can exist for certain classes of magnetic symmetry. Later on, Dzyaloshinskii -only two years after completing his Ph.D. dissertation!- predicted [9] this type of coupling, which was observed afterward by Astrov [10]. Multiferroicity was observed for the first time 6 years after in nickel-iodine boracite by Ascher et al. [11]. However, the concept of "multiferroicity" was not coined until 1994 by Schmid [12], completing the basis of the current knowledge on multiferroic/magnetoelectric materials field.

Magnetoelectricity as a hot topic reached its peak in 1973, with the celebration of the "1st Magnetoelectric Interaction Phenomena In Crystals" conference (MEIPIC-1); however, the fact that large enough magnetoelectric effects were not found together with the lack of compounds that display such effect and the difficulties of growing them, resulted in decreasing interest on magnetoelectric coupling phenomenon. This lack of interest lasted until 1985, when the publications involving magnetoelectric or multiferroic phenomena revived (see fig. 1.2); however, this little renascence can be ascribed only to the exponential growth of the scientific community (as can be inferred from fig. 1.2).

A requirement of the spintronics industry, the electric control of magnetization, triggered the revival of multiferroic materials at the beginning of 00's decade (a representative paper of this renascence is "Why Are There so Few Magnetic Ferroelectrics?" by N.Hill [13], which is focused on the scarcity of multiferroic materials). Important improvements on the crystal and epitaxial thin film growth techniques also took an important role in the reemerging, allowing the identification of new kinds of multiferroics. Some milestones in

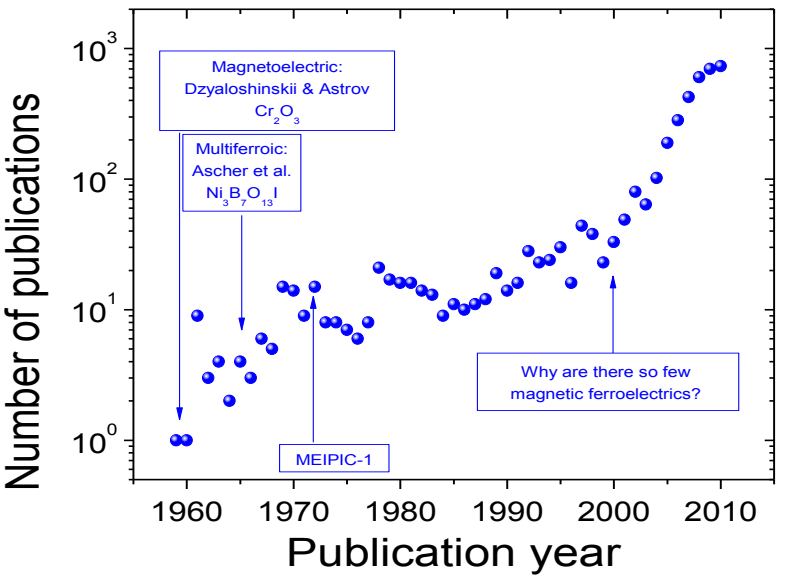

Figure 1.2: *Evolution of the interest in magnetoelectric/multiferroic materials measured by the publications per year with "magnetoelectric" or "multiferroic" as keyword according to* Web of Science. *Some milestones are labeled: i) prediction and observation of magnetoelectric coupling by Dsyaloshinski [9] and Astrov [10], ii) discovery of multiferroicity by Ascher et al. [11], iii) celebration of first MEIPIC conference, and iv) publication of the paper "Why Are There so Few Magnetic Ferroelectrics?" [13].*

the discovery of these new multiferroic/magnetoelectric materials are: i) the discovery of the first single-phase multiferroic material at room temperature ($BiFeO_3$ [14]), ii) the discovery of the first material where ferroelectricity arises from magnetic order ($TbMnO_3$ [2]), and iii) the fabrication of the first two-phase multiferroic material at room temperature displaying magnetoelectric coupling ($BaTiO_3$-$CoFe_2O_4$, [15]).

After this brief historical introduction, the focus turns on the classification of multiferroic materials. These can be divided in single-phase (section 1.1) and composite multiferroics (section 1.2).

1.1 Single phase multiferroics

Single-phase multiferroics are those materials that show both ferroelectric and ferromagnetic order [16–23]. Thus multiferroicity is intrinsic of the material. Khomskii classified single-phase multiferroics in two big groups and other subgroups [24], according to the physical mechanism behind ferroelectricity.

Type I single phase multiferroics: ferroelectric multiferroics[1]

Type-I multiferroics are those materials in which ferroelectricity and magnetism have different sources; usually they show large polarization values and ferroelectricity appears at much higher temperatures than magnetism. This difference in transition temperatures reveals that both orders involve different energy scales and mechanisms, which provokes the occurrence of weak magnetoelectric coupling. These materials are in turn separated in several subgroups:

[1] We have called this group "ferroelectric multiferroics" in analogy with the type-II multiferroics, which are magnetic multiferroics. However, we should stress that here multiferroicity is not due to ferroelectricity, because magnetic and ferroelectric order have two different sources. On the contrary, in magnetic multiferroics, multiferroicity is due to magnetic order, because magnetic order is at the origin of ferroelectricity.

i) *Ferroelectricity due to lone pair:* In these materials, one of the cations (i.e. Bi^{3+}, Pb^{3+},...) has two electrons in a s orbital far from the core and without being part of any chemical bond. These electrons generate an electric dipole, which is the origin of ferroelectric order. Other cations (i.e. Fe^{3+}, Mn^{3+}, Ni^{2+},...) are responsible for magnetic properties. The most relevant example of this class is $BiFeO_3$ [14]. These materials are antiferromagnetic; however double perovskites, such as $BiNiMnO_6$ [25–28], offer a unique possibility to combine ferroelectricity due to lone pair and ferromagnetism arising from the ferromagnetic order of B cations, in the mentioned example Ni^{2+} and Mn^{4+}.

ii) *Ferroelectricity due to charge ordering:* Charge ordering can occur in compounds having similar cations in the same structural site but having different valence. After they become ordered both sites and bonds of the transition metals turn out to be inequivalent. This can lead in some cases to ferroelectricity [29]. One example is $TbMn_2O_5$ [30].

iii) *"Geometric" ferroelectricity:* In hexagonal manganites (ABO_3 with A=Y, Lu, ...) ferroelectricity occurs because the tilting of the MnO_5 polyhedron provides a closer packing. As a result, the oxygen ions move closer to the rather small A ions, leading to the formation of an electric dipole [31, 32].

Type-II single phase multiferroics: magnetic multiferroics[2]

Type-II multiferroics correspond to materials in which magnetism causes ferroelectricity, implying an strong coupling between them. These show smaller electric polarization values and ferroelectricity always appears at lower temperature than magnetic order (always antiferromagnetic). These are:

[2]These materials are also called magnetic ferroelectrics as in the title of the present thesis.

i) *Spiral magnets:* Spiral magnets are those where atomic spin rotate across the lattice in a defined plane, this breaks the symmetry and allows ferroelectricity. However, ferroelectricity only takes place in spiral magnets when the so-called cycloidal spin arrangement sets, that is spins rotate in the plane of the propagation of the spiral. In this case, ferroelectricity arises in the plane of the cycloid and perpendicular to the propagation vector of the cycloid due to the so-called inverse Dzyaloshinsky-Moriya interaction ($\mathbf{P} = A \sum \mathbf{r}_{ij} \times (\mathbf{S}_i \times \mathbf{S}_j)$, being $\mathbf{r}_{ij}$ the vector connecting the $\mathbf{S}_i$ and $\mathbf{S}_j$ spins). Here, sizable spin-orbit interaction is needed (A), if A is large the magnetoelectric coupling is strong. The cycloid is sensible to the application of a magnetic field, which can produce rotation of cycloid plane by 90^o (so-called flopping), inducing a change in the direction of the ferroelectric polarization. $TbMnO_3$ is the archetype of this class of multiferroic materials [2].

ii) *Collinear magnets:* In these materials one-dimensional chains of up-up-down-down spins are formed due to the exchange striction. The distortion induced by up-up (down-down) or up-down (down-up) bonds is different, which provokes the formation of ordered electric dipoles. An example is Ca_3CoMnO_6 [33], or E-type rare earth manganites [34], f.i. $HoMnO_3$ [35].

1.2 Composite multiferroics

The scarcity of single phase multiferroic materials make composite materials an interesting alternative [23, 36–43]. In opposition to single-phase multiferroics, multiferroic order is not intrinsic but results from the combination of two materials that are ferroelectric and ferromagnetic, separately. Therefore, the availability of ferromagnetic and ferroelectric materials at room temperature makes easy to obtain multiferroic composite materials at room temperature.

In composites, magnetoelectric coupling can occur via different interface mechanisms [37]:

- *Strain mediated coupling:* This arises from an elastic coupling between ferromagnetic and ferroelectric materials, when the materials are magnetostrictive and piezoelectric [44]. Here, application of either magnetic or electric external fields can result in changes of polarization and magnetization, respectively. This is the case of $CoFe_2O_4$ columns embedded in a $BaTiO_3$ matrix [15] or a $La_{2/3}Sr_{1/3}MnO_3$ film grown on top of a (001) oriented $BaTiO_3$ single-crystal [45]. Multiferroic composites containing a rare earth-iron alloy are another important example [the most important: Terfenol-D ($Tb_{1-x}Dy_xFe_2$)], and a piezoelectric phase that show giant magnetoelectric effect [46] due to the large magnetostrictive coefficient of the metallic alloy.

- *Charge mediated coupling:* The coupling occurs because the ferroelectric accumulates charge at the interface and the magnetic state of ferromagnet is sensitive to changes in the valence state of their components (f.i. $La_{1-x}Sr_xMnO_3$). Therefore, a change in the interfacial charge (produced by the electric switching of the ferroelectric) would induce a change in the magnetization. This is the case of $La_{0.8}Sr_{0.2}MnO_3$ thin film on top of a $PbZr_{0.2}Ti_{0.8}O_3$ single-crystal [47], where the valence state of the Mn is modulated by the electrically switchable surface charge of $PbZr_{0.2}Ti_{0.8}O_3$.

- *Exchange bias mediated coupling:* Exchange bias is produced at the antiferromagnetic/ferromagnetic interface. One of the origins of exchange bias can be the pinning of the domain walls of the antiferromagnet, which display net magnetic moment, to the ferromagnetic domains of the ferromagnet. Taking advantage of that, in antiferromagnetic multiferroics, antiferromagnetic domain walls are coupled to ferroelectric

domain walls [48], the changes in the ferroelectric domains configuration induced by application of an electric field in the antiferromagnet are converted in magnetization changes in the ferromagnet, resulting in magnetoelectric effect.

This is the case for instance of Permalloy (NiFe alloy) thin film grown on top of and hexagonal manganite [49, 50]. Note that here the effective magnetoelectric coupling results from the combination of an interfacial effect (here only magnetic), and the intrinsic magnetoelectric coupling present in the antiferromagnet. The fact that the most studied multiferroic materials display antiferromagnetic order, rather than ferromagnetism, and ferroelectricity at room temperatures makes exchange bias a suitable mechanism to take profit of them.

- *Interface bonding reconstruction mediated coupling:* The ferroelectric control of interfacial magnetization or spin polarization in a ferromagnet has also been observed in a $Fe/BaTiO_3/La_{1/3}Sr_{2/3}MnO_3$ artificial multiferroic tunnel junction [51] wherein the $BaTiO_3$ is the ferroelectric tunnel barrier, and the half-metallic $La_{1/3}Sr_{2/3}MnO_3$ bottom electrode serves as a spin detector. The results showed that the interfacial modifications of the spin-polarized carriers of the Fe electrode at the $Fe/BaTiO_3$ interface can be induced by electrically switching the polarization states in the $BaTiO_3$ layer. Thus, the interplay between the two non-volatile polarization states and their influence on the spin polarization can lead to a change in the tunnel magnetoresistance (TMR) of this magnetic trilayer.

Note that all the discussed mechanisms that give rise to magnetoelectric coupling take place at the interface between the ferroelectric and the ferromagnetic material. If the contact area between them is larger, the resulting magnetoelectric coupling is expected to be also larger. The architecture of the

composite will determine the contact area between the two materials. That is the reason why composites are also classified according to their architecture [39]:

i) *Layered (horizontal) heterostructures:* These heterostructures are composed by n alternating layers of a ferroelectric and a ferromagnetic material, where n can be between two (bilayers) and a very large number (multilayers). See for instance: thin film bilayered structure of $Pb(Zr_{0.53}Ti_{0.48})O_3$-$Co_{0.9}Zn_{0.1}Fe_2O_4$ [52], or bulk bilayered structure of $La_{2/3}Sr_{1/3}MnO_3$ on 0.72PMN-0.28PT (001) single-crystal [53].

ii) *Self-assembled nanocomposites with vertical geometry:* The prototypical vertical heterostructure consists of a magnetic spinel phase epitaxially embedded into the ferroelectric matrix. See for instance: $BaTiO_3$-$CoFe_2O_4$ vertical composites [15].

Particulate composite are also a possible architecture in thin film form (see f.i. [54–56]); however, they are not so relevant compared to the other two mentioned architectures. Other architectures are the three phase composites [57], rod-array composite (the bulk equivalent of vertical composite thin films) [58, 59] or core-shell composite [60].

1.3 The present thesis

1.3.1 Goal

The goal of the present thesis is to control the ferroelectric polarization by the application of a magnetic field in thin films of multiferroic oxides.

1.3.2 Materials

The materials and architectures of the analyzed multiferroic systems have been chosen in order to compare the advantages and disadvantages of relevant different classes of multiferroic materials, i.e. composite and single-phase multiferroics.

From the single-phase multiferroics group, a type-II multiferroic material has been chosen, because larger coupling between electric and magnetic order is expected compared to type-I multiferroics. The selected material has been the orthorhombic (o-) phase of $YMnO_3$. In bulk it displays collinear spin alignemt, (E-type antiferromagnet), with Néel temperature ≈42 K. The antiferromagnetic structure draws a zig-zag spin alignment in the plane where the Mn ions are contained (*ab*-plane, *Pbnm* notation). Ferroelectricity, in this case due to exchange striction, emerges at the so-called lock-in temperature ≈30 K, with rather low polarization (≈220 nC/cm^2), contained in the *ab*-plane [61]. This material is also interesting because the rare-earth is non-magnetic, which allows the interpretation of the multiferroic properties only in terms of structural and magnetic properties of the Mn's sublattice. Moreover, changes in magnetic properties respect to the bulk in epitaxially strained o-$YMnO_3$ thin films have been already observed [62, 63]. This has been ascribed to the presence of spin-canting as a result of the modification of the angles and distances between Mn and O, making this material even more interesting.

In composites, we have explored both horizontal and vertical architectures, and we have disregarded those where the substrate has an active contribution.

From the comparison of horizontal and vertical architectures it is found that both present some advantages and disadvantages. In layered structures, samples displaying good magnetic and ferroelectric properties have been produced [52, 64, 65]. However, here the contact area is limited by the number of layers, and consequently it strikes on the resulting magnetoelectric coupling. In addition, the effect of substrate clamping limits the

resulting magnetoelectric effect (if it is mediated by strain coupling). In vertical heterostructures the substrate clamping is reduced at once with the maximization of ferroelectric-magnetic interface area. This should lead to larger magnetoelectric coupling, as shown by microscopy in refs. [66, 67]. However the large leakage often present in these composites do not allow to perform magnetoelectric measurements at the microscale (i.e using electric contacts with diameters on the scale of microns).

Among the variety of materials used to grow multiferroic nanocomposite thin films [37, 39], one of the most studied systems is that formed by a ferromagnetic spinel (AB_2O_4) and ferroelectric perovskite (ABO_3). Here, we have chosen $CoFe_2O_4$ and $BaTiO_3$ because they are well-known ferromagnetic and ferroelectric materials, respectively, and they, as single-layer thin films, show excellent functional properties at room temperature. $BaTiO_3$ is one of the most well-known ferroelectric materials, with good ferroelectric properties, P = 26 μC/cm^2 (room temperature), T_c = 393 K, and sizable piezoelectric coefficients [68]. In addition to paraelectric - ferroelectric transition (where cubic $BaTiO_3$ becomes tetragonal), $BaTiO_3$ displays two additional structural transitions: from tetragonal to orthorhombic (278 K) and from orthorhombic to romboedric (183 K). $CoFe_2O_4$ is an insulating ferromagnetic[3] spinel with M = 3 μ_B / f.u. and T_c above 700 K, and large magnetostrictive coefficient [69]. The selection of the composite has also been done based upon the expertise in growing thin films of perovskite and spinel oxides of the group in which this thesis has been developed. Also, because $BaTiO_3$-$CoFe_2O_4$ is expected to display lower losses than other nanocomposites with multiferroic phases, such as $BiFeO_3$, which are poorer insulators.

[3]Remark that $CoFe_2O_4$ is ferrimagnetic instead of ferromagnetic; however, in the present thesis distinguish between ferromagnetism and ferrimagnetism is not relevant. That is the reason why we have used the term ferromagnetic to describe the magnetic nature of $CoFe_2O_4$.

1.3.3 Methods

In order to achieve the final objective of the present thesis, different methods, enumerated as follows, have been used.

i) *Ferroelectric/Dielectric characterization:* Knowing ferroelectric and dielectric properties is crucial in multiferroic characterization. This permits the verification of multiferroic properties of the studied materials. This characterization is based on the measurement of the dielectric constant, P-E and ϵ-E loops, and pyroelectric current. The corresponding experimental systems have been set up for the first time at Institut de Ciència de Materials de Barcelona within this thesis.

ii) *Magnetoelectric characterization:* Coupling between ferroelectric and magnetic order has been analyzed by means of magnetodielectric measurements. Magnetocurrent and ferroelectric loops under applied magnetic field measurements have also been used to the same purpose. The corresponding experimental systems have been set up for the first time at Institut de Ciència de Materials de Barcelona within this thesis.

iii) *Strain engineering:* The effects of the structural changes induced by strain engineering on the final dielectric/ferroelectric/magnetoelectric properties have been also analyzed. Epitaxial strain has been modified changing the deposition conditions and/or thickness.

Details about structural, morphological and magnetic data are given in the introduction of each chapter or in the referred references, further information can be found in X. Martí [62] and N. Dix [70] theses.

1.3.4 Thesis structure

As this thesis is the first one of our research group containing extensive dielectric/ferroelectric/magnetoelectric characterization of thin films, chapter

2 contains a detailed description of the experimental methods, which are expected to be useful in the future. Expert reader may not need reading it. This chapter contains sections devoted to the experimental set-up (section 2.1), dielectric, ferroelectric and magnetoelectric characterization (in sections 2.2, 2.3 and 2.4, respectively).

The aim of the following chapters is to describe the most relevant obtained results. Chapter 3 describes the results in the characterization of the o-$YMnO_3$ thin films, we will see that cycloidal order stabilizes in thin film form and that polarization can be partially controlled by an external magnetic field. Moreover, we will give hints about the control of magnetic order by strain engineering. Chapters 4 and 5 describe the results obtained in the $BaTiO_3$-$CoFe_2O_4$ composites in their horizontal and vertical architecture, respectively. In these we will see that both configurations show multiferroic properties at room temperature, with presence of magnetodielectric response. In both we will explore the effects of epitaxial strain on their dielectric/ferroelectric properties.

Conclusions of the thesis are given at the end.

Part II

Experimental methods

Chapter 2

Dielectric, ferroelectric and magnetoelectric characterization of multiferroic thin films

The electric characterization performed in this thesis includes the dielectric and ferroelectric measurements. Even though dielectrics and ferroelectrics have been characterized since long time ago (f.i. [71, 72]), the electric characterization of multiferroic thin films implies many new challenges, that have been considered in detail.

We will start describing the experimental procedures and experimental setups, at room and cryogenic temperatures, designed with the specific purpose of ferroelectric, dielectric and magnetodielectric characterization of multiferroic films (section 2.1). Afterwards, the dielectric and ferroelectric characterization measurement methods are described in sections 2.2 and 2.3, respectively. Both sections start with a brief summary, without the aim of being exhaustive, of the dielectric and ferroelectric phenomena. This is followed by the description of the performed measurements: measurement of dielectric permittivity (ϵ), electric polarization (P), or equivalent electric displacement (D) and their dependence on electric field (E), frequency (ν) or temperature (T). This description includes the analysis of the distinct contributions (intrinsic and

extrinsic) that can be relevant in the measured magnitudes, and the protocols used to discriminate them. Finally, in section 2.4 we describe the measurement methods used to evaluate the magnetoelectric coupling, thus variations of dielectric permittivity and/or ferroelectric polarization under the application of a magnetic field.

2.1 Experimental

The experimental set-up described here has been designed in the framework of the present thesis to measure relevant dielectric and ferroelectric parameters, i.e. dielectric permittivity (ϵ) and polarization (P) of multiferroic thin films, as a function of applied electric field, temperature, and magnetic field.

The experimental methods and experimental set-up used will be described as follows: i) description of samples preparation to perform electric measurements, ii) description of the measurement configurations, iii) description of the measurement experimental set-up.

2.1.1 Samples preparation for electric measurements

Plano-parallel capacitor is the most suitable geometry for the measurement of dielectric permittivity and polarization in bulk ceramics or thin films. The measured dielectric/ferroelectric material of thickness t is embedded in between two equal electrodes with a defined area A, which are parallel (depicted in figure 2.1). In a plano-parallel capacitor, these geometrical parameters determine the relation between ϵ or P and the measured magnitudes (these relations will be in the section of dielectric and ferroelectric characterization, respectively). Therefore, samples have been prepared for the purpose of obtaining plano-parallel capacitors, with the characterized thin film acting as a dielectric (fig. 2.1).

Thin films have been grown on a suitable conductive electrode adapted to

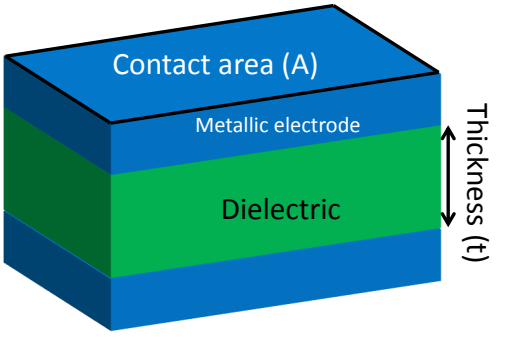

Figure 2.1: *Sketch of a plano-parallel capacitor.*

the objective on each chapter. The details about the growth conditions of films or heterostructure are specified in the corresponding chapter. Pt top electrodes (with areas between 0.01 and 0.30 mm^2 and a thickness of $\approx$ 100 nm) were deposited ex-situ by rf sputtering, through a shadow mask. The Pt deposition conditions are 20 W of rf sputtering power, and 0.01 mbar of Ar atmosphere. Pt has been chosen because it is a novel metal (easy to grow without impurities and difficult to be degraded) and has displayed to be appropriate as a top electrode while measuring ferroelectricity [73]. Previous to Pt growth, the sample had been cleaned with acetone and ethanol, and subsequent exposition to an ozone atmosphere plus ultraviolet light during 10 min (UVO Cleaner: 42, Jelight Company Inc.).

2.1.2 Measurement configuration

We call "measurement configuration" the manner in which the thin film is electrically contacted. We have used two measurement configurations: the bottom-top and the top-top (b), as described in the following.

In the bottom-top configuration [figure 2.2(a)] the bottom and top electrodes are contacted. This is an asymmetric configuration, because bottom electrode - insulator and insulator - top electrode interfaces can be different, owing to the fact that top and bottom electrode materials are different. An

asymmetric contact configuration [scheme in fig. 2.2(a)] can lead to very asymmetric P-E or ϵ-E loops or polarity dependent impedance. Exceptionally, in chapter 4 we have used this technique, because of the interest of the asymmetry itself.

In the top-top configuration [figure 2.2(b)], which has been used in most of the cases, two top electrodes are contacted. Therefore, the measured capacitance should correspond to a series of two identical capacitors contacted through the bottom electrode [scheme in fig. 2.2(b)]. This is equivalent to the measurement of a single thin film capacitor with double thickness. With this configuration, the asymmetries due to the different metal-insulator interfaces cancel out.

2.1.3 Experimental set-up

The different dielectric parameters characterized and the equipments used are:

- Dielectric characterization. It has been performed using an impedancemeter HP4192A LF (Agilent Co.), which measures the impedance and the phase of the the connected circuit (which includes the sample and the wiring). After a suitable analysis (described in section 2.2), dielectric properties of the sample can be extracted. The available measuring frequency range is between 5 Hz - 13 x10^6 Hz and the oscillating voltage has been set to 300 mV in all the experiments. With the impedancemeter we have performed impedance spectroscopy, i.e. analysis of ϵ-ν, ϵ-T, and ϵ-E measurements.

- Ferroelectric loops have been performed using a TFAnalyser2000 (Aix-ACCT Systems GmbH. Co.), which measures the current versus the applied voltages up to 25 V at frequencies between 5 x10^{-4} Hz and

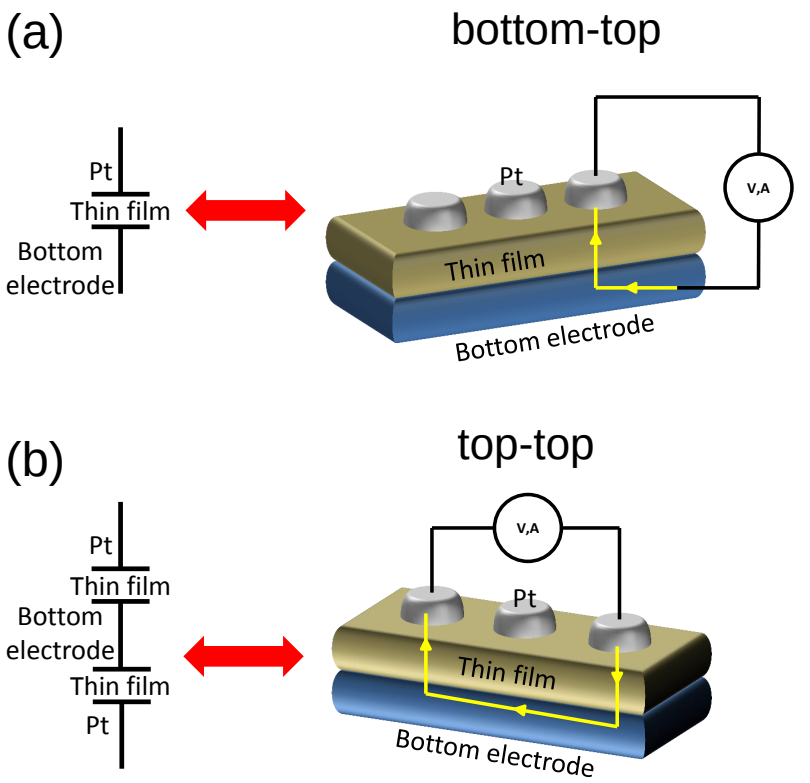

Figure 2.2: *Schemes (left) and sketches (right) of bottom-top (a) and top-top measurement configuration.*

2 x10^6 Hz. From the integration through time of the current, the polarization can be obtained (described in section 2.2).

- Pyrocurrent (and magnetocurrent) measurements have been performed using an electrometer (Model 617, Keithley Co.). From the measurement of the current, polarization dependence on temperature and magnetic field can be obtained similarly to P-E measurements.

When using the impedancemeter, the connections between the metering device and the part of the experimental set-up placed near the sample has been done with the three terminal configuration [74]. We have used this measurement configuration for two reasons. First, because it is the most simple configuration that gives accurate values for impedance range between 10 Ω and 20 MΩ. This range corresponds to the measured values in the samples characterized in the present thesis at the used frequencies. Second, this configuration allows to use only two cables (two wires with their respective shield) to perform the measurement, this makes simpler the needed experimental system. The three terminal configuration [sketched in fig. 2.3(a)] consists in the short circuit of low current with low voltage and high current with high voltage terminals near the apparatus. At the same time that current and voltage are short circuited, their respective shields are also short circuit. The three terminal configuration name is because near the sample we have three wires: the high output, the low output and the shield.

In measurements performed with TFAnalyser2000, the sample has been contacted to the metering device using shielded wires [sketched in fig. 2.3(b)]. The wiring in the measurements performed with the electrometer is very similar to that used in TFAnalyser2000; however, here low-voltage low-current cable and high-voltage high-current cable [L and H of fig. 2.3(b)] to HI and LO outputs of the electrometer, and the shielding is connected to the PPMS chamber.

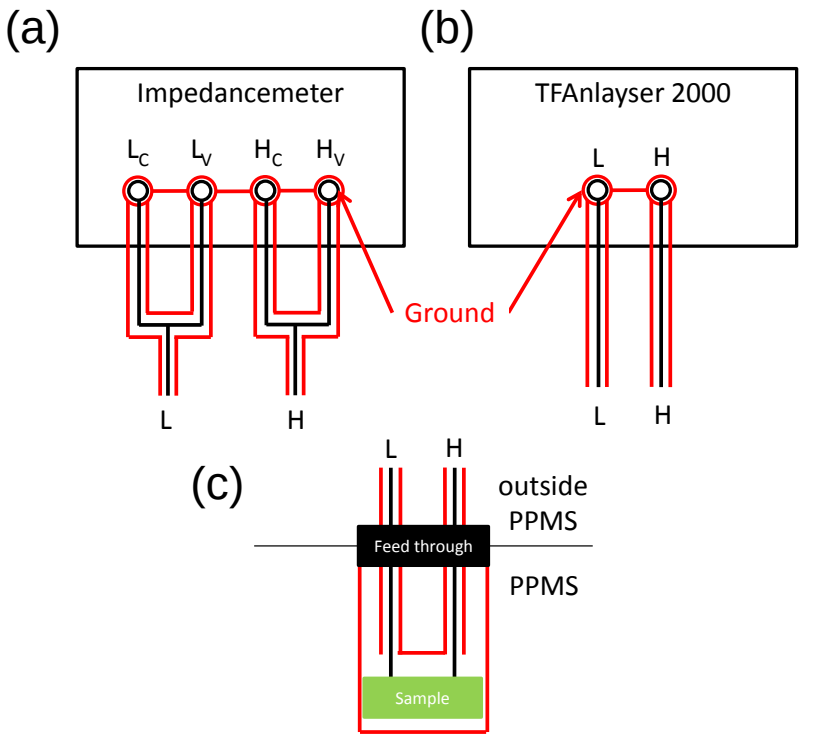

Figure 2.3: *Schemes for wiring configuration while using the impedancemeter (a) and the TFAnalyser2000 or the electrometer (b). (a) High voltage (H_V) and current (H_C) and low voltage (L_V) and current (L_C) outputs are shortcircuited, near the impedancemeter. Also near the impedancemeter the shielding of the four wires is shortcircuited. Two final outputs are obtained L (low) and H (high), with their corresponding shields. Near the sample, the shields of the two wires are shortcircuited again. (b) Here, there are only two outputs H and L, equivalent to those described in (a). (c) Scheme of the feed-through connections while using PPMS set-up.*

The shields of the wires get as close as possible to the sample [as sketched in figs. 2.4 for each experimental set-up]. Notice that in this measurement the series resistance and inductance of the contacts and the wires are contributing to the measured signal. Therefore, their contribution should be taken into account.

The connection between the cables and the sample has been done using two particular experimental set-ups, which have been built and used, respectively for room temperature and cryogenic temperatures and/or measurements under magnetic field. These are described as follows:

- *Room temperature* [Fig. 2.4(a)]: Room temperature measurements with top-top configuration have been performed using tungsten needles (SE-20TB, Signatone Co.) with a diameter of 20 μm, which are placed on the top electrodes using a micropositioner (S-2 + S-725 , Signatone Co.). When a bottom-top configuration has been required, the bottom electrode has been contacted using silver paste and connected directly to the metering device. Shielded and as short as possible connections from needles to metering device have always been used. The shielding covers the wires till the needles (as indicated in the fig. 2.4(a)). A Faraday box can be used for low capacitance measurements, when the low measured impedance makes the environment noise important; this is not the case of the samples used in the present work.

- *In PPMS* [Fig. 2.4(b)]: Measurements performed in a PPMS (Quantum Design Co.) have been done using a purpose-designed sample holder. In the holder, the top electrodes are contacted with silver paste (standard silver paste solved by 4-Methyl-2-Pentanone) to a set of pads through Pt wire (annealed 25 μm wire with purity of 99.99 %, GoodFellow Co.), two of these pads (chosen for the measurement) are contacted to two shielded cables with low thermal losses (Cryo cable - type SS, Lakeshore Co.) through Cu wires. Two feed-through connections bring

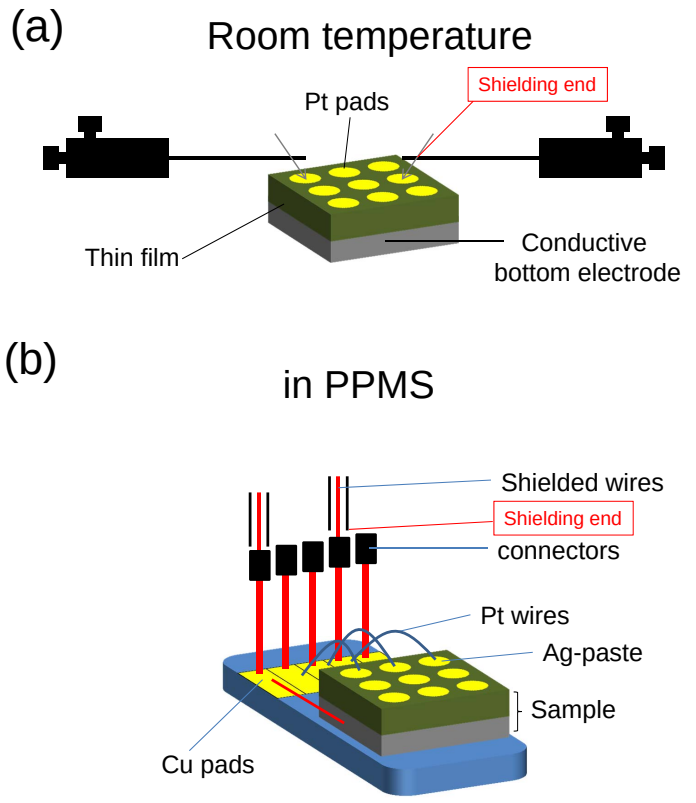

Figure 2.4: *Sketches of contacting procedures used in room temperature measurements (a) and measurements performed in PPMS (b).*

the shielded wires from the PPMS to the metering device [see fig. 2.3(c)], using the respective contact configuration depending on the metering device. Therefore, the shielding covers the wires till the pads connection (as indicated in the fig. 2.4(b)). In order to harden the contacts, the holder is heated at 100^{o}C during 10 min inside an oven. The designed holder is placed on a Multi-Function Probe (Quantum Design Co.). All is inserted in the PPMS and its cavity is connected to the cables shield; therefore, the PPMS cavity acts as a Faraday box. The PPMS measures in the temperature range between 2.0 and 400K. In this system, the magnetic field can be controlled from -9 to +9 T, and applied in and out of the thin film plane.

2.2 Dielectric characterization

Dielectric materials have the ability of sustaining an electric field. This inner electric field provokes a redistribution of the internal charges inducing a polarization (P) on the surface. In these materials the electric displacement field is defined as:

$$D \equiv \epsilon_0 E + P \tag{2.1}$$

where ϵ_0 is the vacuum permittivity.

In linear, homogeneous, isotropic dielectrics the polarization of the material is defined as

$$P = \epsilon_0 \chi E \tag{2.2}$$

where χ is the electric susceptibility. Therefore:

$$D = \epsilon_0 E + \epsilon_0 \chi E = \epsilon_0 (1 + \chi) E = \epsilon_0 \epsilon_r E = \epsilon E \tag{2.3}$$

where ϵ is the material dielectric permittivity and ϵ_r is the material relative permittivity.

When dielectric materials are under the influence of a time-dependent electric stimulus [E(t) or E(ν)], the dielectric permittivity response contains two terms: a component that is in-phase with the stimulus (ϵ') and a component that is out-of-phase (ϵ''). ϵ'' represents the dielectric losses, due to the disability of the field-induced dipoles to follow the variations of an applied electric field. Therefore, dielectric permittivity is defined as a complex number ($\widetilde{\epsilon}$) with a real and an imaginary part.

$$\widetilde{\epsilon} = \epsilon' - i\epsilon'' \tag{2.4}$$

In engineering applications it is customary to define the loss angle (δ), corresponding to the lag of the induced polarization behind the driving electric field. tanδ is the ratio between the imaginary and real part of dielectric permittivity.

$$tan\delta = \frac{\epsilon''}{\epsilon'} \tag{2.5}$$

This value is taken as the figure of merit of the material.

In dielectric materials in principle there are no free charge carriers. If electric transport is present, the definition of the imaginary part of the dielectric permittivity is usually completed adding the electronic transport term (σ), which corresponds to the conductivity of the dielectric under the application of constant bias, thus to the charges that travel across the dielectric, and it is inversely proportional to the frequency (ω).

$$\widetilde{\epsilon} = \epsilon' - i(\epsilon'' + \frac{\sigma}{\omega}) \tag{2.6}$$

2.2.1 Dielectric permittivity measurement

Dielectric permittivity is the relevant parameter in dielectric characterization. We have extracted the permittivity from capacitance measurements using the well-known relation between dielectric permittivity and capacitance for a plano-parallel capacitor $C = \epsilon \cdot A/t$, where A is the electrode area and t the thickness.

The capacitance is calculated from the measured value of the impedance as:

$$\widetilde{C} = \frac{1}{i\omega\widetilde{Z}} \tag{2.7}$$

where ω is the measurement frequency in radians.

Impedance is the value obtained by the impedancemeter, which measures the coefficient between the corresponding complex applied ac voltage ($V(t) = V_0 sin(\omega t) \rightarrow \widetilde{V}(\omega) = V_0 e^{i\omega t}$, where V_0 is the amplitude of the ac signal) and the output current.

$$\widetilde{V}(\omega) = \widetilde{Z}(\omega)\widetilde{I}(\omega) \tag{2.8}$$

That is equivalent to the Ohm's law for applied dc voltages, and $\widetilde{Z}$ is a complex number with real (Z') and imaginary part (Z'') equivalent to a dc resistance (R).

In the measurement of the impedance vector in a thin film extrinsic contributions [75] can become relevant; this is simply because (in thin film) intrinsic contribution is reduced owing to the reduced measured amount of material. These extrinsic contributions are due to the experimental set-up (wiring, contact resistance and others). Moreover, dielectric conductivity is usually larger than in bulk because short circuits between the two contact electrodes are more likely due to the reduced thickness, which can also lead to ficticious values of measured permittivity [76]. Finally, extrinsic

contributions of the studied material such as grain boundaries, depletion layer at the electrode, and others, also present in bulk, can also yield to the wrong determination of the dielectric permittivity. Finally, these extrinsic effects are more relevant in multiferroics mainly because they are usually poorer insulators (with larger dielectric conductivity) and show small dielectric permittivity (reducing even more the bulk contribution).

These extrinsic contributions should be always identified. In the next section, we will explain in detail how the extrinsic contributions can be identified using impedance spectroscopy, and how dielectric permittivity values can be safely inferred.

2.2.2 Impedance spectroscopy

In impedance spectroscopy [77, 78], the dependence of the impedance vector on frequency (impedance spectrum) is measured. It is a common tool in dielectric characterization where the obtained data are analyzed in order to distinguish the different electrical contributions to the dielectric response. In short, impedance spectroscopy allows to distinguish the bulk contribution from other extrinsic effects, such as grain boundaries, contact-material interfaces, etc.

Equivalent circuit results from the combination of different circuit elements. These are three:

- *Resistor*: the current is in phase with the applied voltage ($\widetilde{Z} = R$).
- *Capacitor*: the current leads the applied voltage by 90^o ($\widetilde{Z} = \frac{1}{i\omega C}$).
- *Inductance*: the current lags the applied voltage by 90^o ($\widetilde{Z} = i\omega L$).

These circuit elements can be equivalent to real elements of the experimental set-up, f.i. the wires resistance are equivalent to a resistance. Or their

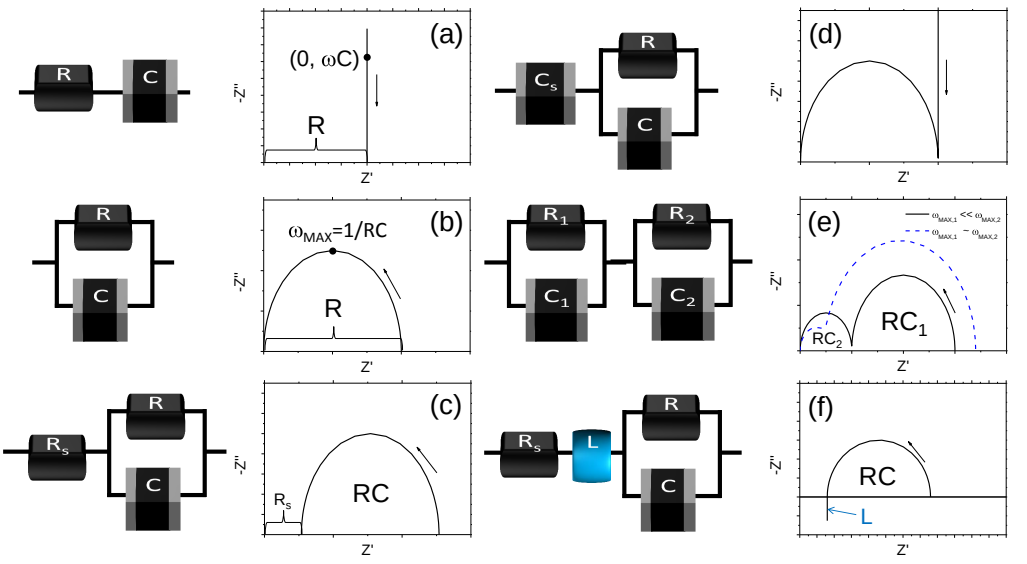

Figure 2.5: *Nqvist diagrams of the most used equivalent circuits to fit dielectric behave in multiferroic thin film. Arrows indicate increasing frequency.*

combination can represent a particular dielectric response, f.i. a grain boundary contribution to the measured impedance is represented by a capacitor in parallel with a resistor.

The impedance vector can be represented in polar or in cartesian coordinates as a function of frequency. However, in impedance spectroscopy analysis by means of equivalent circuit Nqvist diagram, in which the imaginary part is plotted as a function of the real part of the impedance, is commonly used. Nqvist diagrams corresponding to the most common equivalent circuits are plotted in figure 2.5. Clearly, the shape of the diagram helps to determine the elements of the equivalent circuit.

The semicircle shape of a RC contribution comes from the impedance vector dependence on frequency. For instance, we can deduce the equation for the Nqvist diagram of the equivalent circuit of figure 2.5(c) from the

impedance of the circuit:

$$\widetilde{Z}(\omega) = R_s + ((\frac{1}{i\omega C})^{-1} + (\frac{1}{R})^{-1})^{-1} \quad (2.9)$$

if the Z' and Z'' are related, it turns out that :

$$(Z' - (R_s + R/2))^2 + Z''^2 = (R/2)^2 \quad (2.10)$$

which is the equation of the circumference centered in $(R_s + R/2)$, and with R diameter of figure 2.5(c). The maximum of this circumference takes place at frequency $\omega_{MAX} = 1/RC$.

Next sections will be devoted to describe the different parts of the equivalent circuits that are commonly found in impedance measurements. First, the details about equivalent circuit part representing the experimental set-up, applicable in all dielectric measurements, are given. Second, the equivalent circuit that corresponds to a usual (non-ideal) dielectric is described. Third, this description is extended for more than one contribution, with the so-called Maxwell-Wagner effect. A brief description of how the different circuit elements are identified with the different contributions of a real impedance spectrum, and the protocol to identify an ideal frequency range to measure intrinsic dielectric permittivity are given at the end.

i) Equivalent circuit of experimental set-up

The circuit elements that contribute to all the impedance measurements are those that correspond to the experimental set-up (fig. 2.6). Even though depending on the device under test and the measurement frequency their contribution can be very small or even negligible, these circuit elements introduce the following contributions (sketched in figure 2.6):

- Series resistance (R_s) corresponding to the resistance of the measurement probes, leads, electrodes. Typical values for the data in the present

thesis are up to 80 Ω.

- Series inductance (L_s) corresponding to the inductance of the leads. Typical values for the data in the present thesis are in the order of 1 μH.
- Parallel capacitance (C_p) corresponding to the probe holder and environment capacitance. $C_p \approx 0$.
- Parallel resistance (R_p) corresponding to the probe holder and environment resistance. $R_p \to \infty$.

The last two contributions are in our experimental set-up those that correspond to the air resistance and capacitance, as it can be inferred from the sketch of figure 2.6. $R_p \approx \infty$ because it corresponds to the resistance of the air, between the two contacts. C_p is very low, compared with the capacitance of the measured thin film. This is because, as it can be inferred from the figure, this capacitance (named straight capacitance) will be approximately at least 10000 times less than the capacitance of the measured film, since the thickness of the film is in the order of 100 nm and the distance between the electrodes is the order of 1 mm. Therefore, both (R_p and C_p) can be neglected.

ii) Equivalent circuit of a non-ideal dielectric

In a non-ideal dielectric, the dielectric permittivity displays an imaginary part due to dielectric losses and conductivity. The impedance in this case can be represented by a resistance in parallel with a capacitance (RC circuit element). Simplifying, the physical meaning of the mentioned capacitance and resistance elements are:

- *Resistor*: long range migration of charge (electrons, ions, or holes); thus a resistor is equivalent to the dielectric conductivity, or dielectric losses.

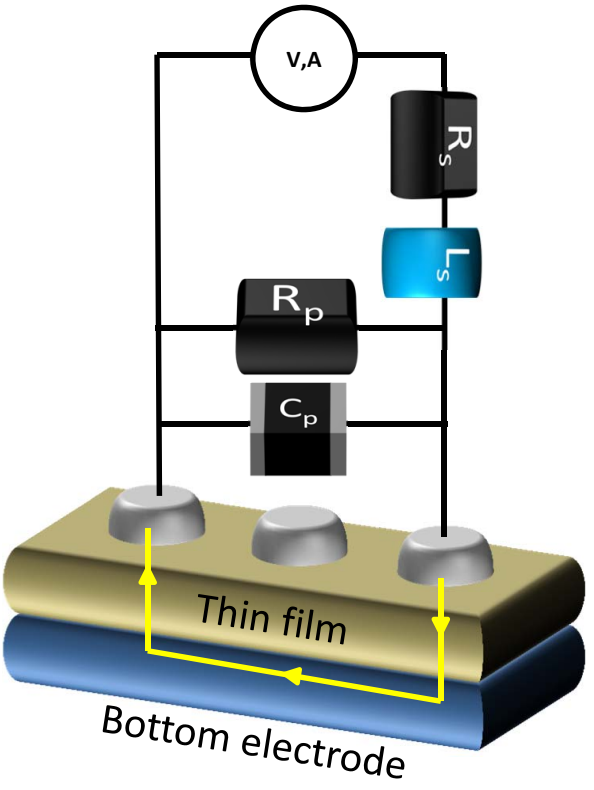

Figure 2.6: *Experimental set-up configuration and elements of the corresponding equivalent circuit.*

- *Capacitor*: polarization process.

The Nqvist diagram that corresponds to this equivalent circuit is plotted in figure 2.7 (solid line); it can be seen that it corresponds to a semicircle, the diameter of which is the resistance and its maximum takes place at ω_{MAX}=1/RC, as it is shown by equations 2.9 and 2.10 for $R_s = 0$.

Often this RC circuit is not enough to describe the impedance dependence on frequency of a real dielectric (in particular of a multiferroic thin film [79]). The distribution of relaxation times [80] due to the common presence of inhomogeneities in the dielectric (ceramic or thin film) makes necessary an extended version of the capacitance, that is, the so-called constant phase element (CPE). The CPE contains itself a dependence on frequency, which can better mimic the impedance dependence on frequency of a real dielectric, as follows:

$$CPE(\omega) = C_0(i\omega)^{n-1} \tag{2.11}$$

$$\widetilde{Z} = \frac{1}{i\omega CPE} \tag{2.12}$$

where C_0 corresponds to the modulus of the CPE and n to its phase. Note that C_0 is not a capacitance magnitude, in fact its units are $F \cdot s^{n-1}$. If n=1 the CPE is an ideal capacitor, and if n=0 the capacitor becomes a resistor. Therefore, n "measures" how far the measured dielectric from the ideal is. This CPE contribution includes the intrinsic dielectric losses of the capacitor. In a typical multiferroic the different electroactive contributions can be well-fitted by a R in parallel with a CPE. In figure 2.7 (dashed and dotted lines), it can be seen that for lower values of n the semicircle gets progressively more squashed, denoting that it is progressively less ideal.

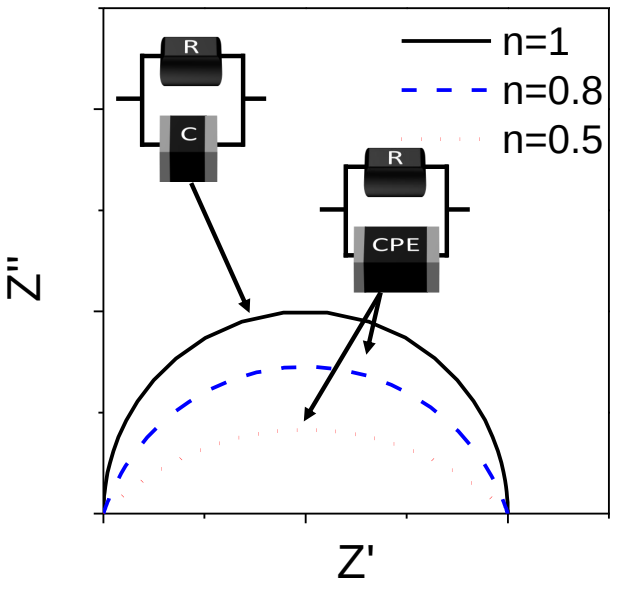

Figure 2.7: *Comparison between different CPE with the same C_0 and different n.*

iii) Equivalent circuit in presence of Maxwell-Wagner effect

Classically the Maxwell-Wagner effect is a phenomenon caused by interfacial polarization [72]. Due to its contribution, the dielectric can actually be described as two parallel sheets of different dielectrics [figure 2.8(a)], characterized by their respective dielectric constants and conductivities.

The equivalent circuit that corresponds to this Maxwell-Wagner phenomenon is formed by two RC elements in series (double RC). This description can also be useful for a bilayered or a superlattice structure, where two intrinsically different dielectrics are present [figure 2.8(b)]. It can also describe the brickwork model [82], which corresponds to a granular ceramic or thin film. In this case grains and grain boundaries are taken into account [figure 2.8(c)], and ascribed to the two contributions of the Maxwell-Wagner effect.

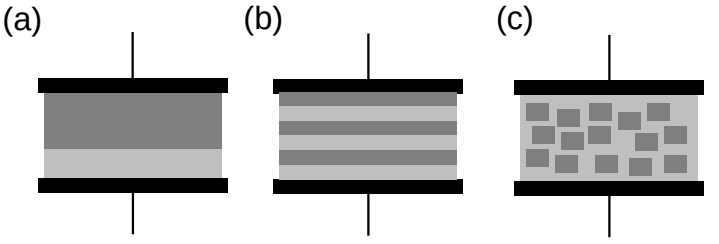

Figure 2.8: *Capacitor systems with Maxwell-Wagner behavior: (a) homogeneous material with charge-depleted interfacial layers, (b) superlattice, and (c) brickwork model for a grained ceramic or thin film. Adapted from [72, 81].*

iv) Impedance spectra fitting by equivalent circuit

Up to here, the typical different circuit parts that can be distinguished in the measured impedance on a multiferroic thin film have been described. Therefore, it is possible to fit a suitable equivalent circuit for a real impedance spectra. The results obtained in the fit allows us to identify the origin of the different contributions to the impedance spectra. The typical values for the different contributions resistance and capacitance (corresponding to a parallel RC circuit element) in a multiferroic thin film are summarized in table 2.1. However, usually this identification should be done in combination with structural, morphological, or other characterizations that allow to cross-check the correspondence between different contributions to the impedance spectra and the properties of the material. F.i.: a typical grain boundary contribution can be relevant in a granular film, and less relevant in a single-crystalline film.

Experimental $\widetilde{Z}$ data have been analyzed by the fitting of the expected response for a given circuit model, selected and built on the basis of physical criteria and with physical sense. The fittings have been performed using the ® Zview program [83], which does a simultaneous fit of Z' and Z'' dependence on ν by using a least-squares algorithm.

From the fitting results, the intrinsic values for the dielectric permittiv-

Table 2.1: *Typical values for capacitance and resistance of the different electroactive contributions (whose equivalent circuit correspond to an RC element) in a multiferroic thin film. Resistance of bulk contribution in multiferroic thin films depends strongly on thin film quality. Adapted from ref. [82].*

Contribution	Capacitance (F/cm)	Resistance ($\Omega\cdot$ cm)
Bulk	10^{-9}-10^{-12}	wide range
Grain boundary	10^{-8}-10^{-11}	10^{5}-10^{6}
Sample-electrode interface	10^{-5}-10^{-7}	$>10^{6}$

ity and conductivity for the bulk contribution can be extracted, using the given plano parallel geometry of the measured capacitor (A and t). For a general RCPE contribution, the conductivity (σ) and the permittivity ($\widetilde{\epsilon}$) are calculated as:

$$\sigma = \frac{t}{A \cdot R}$$
$$\epsilon' = \frac{t}{A}\Re(CPE) = \frac{t}{A}C_0\omega^{n-1}[cos(n-1)\frac{\pi}{2}]$$
$$\epsilon'' = \frac{t}{A}\Im(CPE) = \frac{t}{A}C_0\omega^{n-1}[sin(n-1)\frac{\pi}{2}] \qquad (2.13)$$

v) Ideal frequency measurement range

We have seen that impedance spectroscopy analysis by means of equivalent circuit allows us to infer the properties of the films under study. As we will see below this previous analysis may permit the determination of an ideal frequency range where intrinsic contribution of the films dominates in the measured impedance.

To illustrate that ideal frequency range can be identified, in figure 2.9, it has been plotted a calculated impedance spectrum for a typical equivalent circuit of a multiferroic thin film (line with squares). This is a series resistance

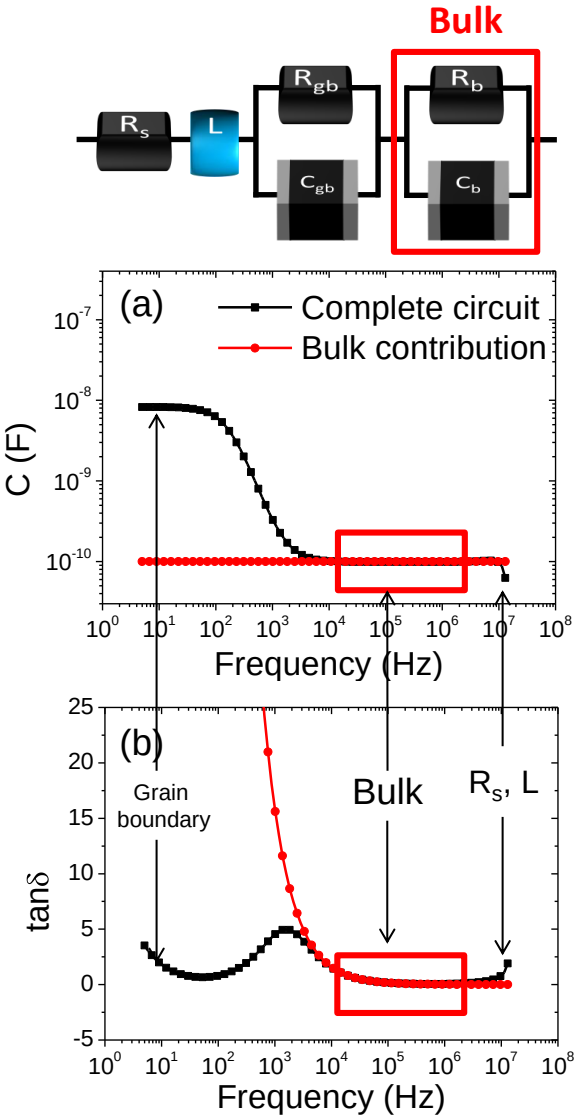

Figure 2.9: *Simulated impedance spectra -(a) Capacitance and (b) tanδ- for the sketched equivalent circuit and for the bulk contribution with the values indicated in the text. "gb" and "b" subindex refer to grain boundary and bulk simulated contributions.*

and inductance of 80 Ω and 1 μH (representing the wiring), a RC (grain boundary contribution) with C = 10 nF, and R = 10 MΩ, and a RC (bulk contribution) with C = 100 pF and a R = 100 kΩ. In the same figure 2.9, only the bulk contribution (without the other contributions) has also been plotted (line with circles). As it can be inferred from the figure there is a frequency range, where both lines merge. Consequently, this is the frequency range where the intrinsic values for the bulk contribution can be extracted. Moreover, the grain boundary contribution (at low frequencies) and the series resistance and inductance contributions (at high frequencies) can also be inferred from the figure (both are labeled). [1] This "ideal" frequency range will depend on the material properties, and, if it is not present, makes mandatory the analysis of the impedance spectra by the fitting of an equivalent circuit.

Summarizing, we have seen that impedance spectroscopy analysis combined with the fittings with equivalent circuit allows us to identify the different electroactive contributions present in our measurement. This analysis also allows to determine the most suitable frequencies at which bulk contribution can be more safely measured.

2.3 Ferroelectric characterization

Ferroelectricity is a phenomenon that takes place in materials that present the capability to display switchable spontaneous polarization. Therefore, a ferroelectric is more than a dielectric because it can keep a finite polarization in absence of an external applied electric field, even after zeroing it. The presence of switchable polarization is concomitant to the presence of ferroelectric domains with different sign. The presence of the domains results in a hysteresis

[1] Similar analysis can be done using typical values of Sample-Electrode interface extrinsic contribution.

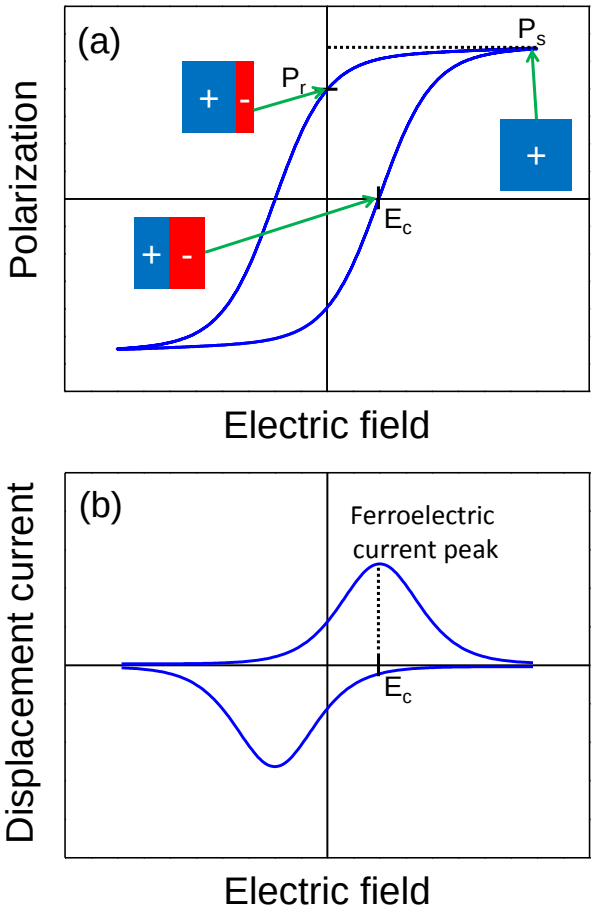

Figure 2.10: *(a) D-E loop for a standard ferroelectric. Ferroelectric domain configuration at different points of the ferroelectric loop is sketched. (b) I-V loop measurement for an standard ferroelectric.*

of the polarization while cycling the ferroelectric by an external electric field. This hysteresis is depicted in figure 2.10(a). First, saturation polarization (P_s) is achieved after applying a large electric field. After zeroing the external field, the polarization decreases to the remanence (P_r), or remanent polarization. The electric field required to change the polarization sign is called the electric coercitivity, or electric coercive field (E_c).

Ferroelectric characterization in thin films [75] is particularly problematic, mainly because films often can display high leakage currents[2]. This is mainly due to a thickness effect, because conductive pinholes caused by different kind of defects can easily cross the sample favoring leakage currents. Leakage, if not reduced, makes the characterization of ferroelectric thin films more difficult, since the contribution to the hysteresis loops may be considerable, leading to fictitious values of relevant ferroelectric parameters, such as the remanent polarization, the coercive field, Curie temperature, and others, and even to the incorrect determination of the ferroelectric character. The electric characterization of multiferroic thin films is even more challenging than that of ferroelectric films [84], because most multiferroic materials appear to be poor dielectrics and have rather low polarization. These two features (leakage and low polarization) imply that the relevance of losses with regard to the ferroelectric polarization in hysteresis cycles is greatly enhanced.

Ferroelectric properties of the studied samples are characterized obtaining P-E loops via current measurements, which are described in section 2.3.1. In this section the extrinsic effects that can appear in these measurements and the methods used to elucidate their contribution on the measurement are described in detail.

Moreover, ϵ-E loops and pyrocurrent measurements have also been used as complementary tool for ferroelectric characterization and to determine other characteristic values such as remanent polarization, and Curie temperature.

[2]Leakage current is that term used in ferroelectric characterization equivalent to the dielectric conductivity in dielectric characterization.

These are described in sections 2.3.2 and 2.3.3, respectively.

2.3.1 Ferroelectric hysteresis loops

The hysteresis loop is naturally one of the key measurements of ferroelectric characterization. There are two measurement schemes commonly used. A capacitance bridge has been traditionally used, as first described by Sawyer and Tower [85]. This method is not very suitable in practice for various reasons; for example, the need to compensate for dielectric loss and the fact that the film is being continuously cycled. Most suitable is the measurement of the I-V characteristics (explained in detail in next section), which provide an abrupt current peak where the ferroelectric switching (switching between P^+ and P^- at coercive field) occurs, and allows to easily disclose the extrinsic ferroelectric effects [figure2.10(b)]. Charge is afterwards obtained integrating the current through the time. When a plano-parallel capacitor with known geometry (area, A, and thickness, t) is used, the polarization and electric field can be obtained. Polarization is the charge per unit surface, and the electric field is obtained by dividing the applied voltage (V) by the thickness.

$$P = \frac{\int I(t)dt}{A} \tag{2.14}$$

$$E = \frac{V}{t} \tag{2.15}$$

We should stress that in an ideal ferroelectric the measured charge value obtained by the integration of the current flowing through the circuit does not correspond to the polarization of the material, but to the electric displacement (D). Therefore, to obtain P from the measured D-E loop the $\epsilon_0 E$ term should be subtracted, as shown by equation 2.1. However, in ferroelectrics high χ is expected, thus $\epsilon = \epsilon_0(1+\chi) \approx \epsilon_0\chi$, and consequently $\epsilon_r = \chi$, implying $P \approx D$. When describing the results in the present thesis (not in the present chapter) D has approximated to -and called- P. This simplification is common

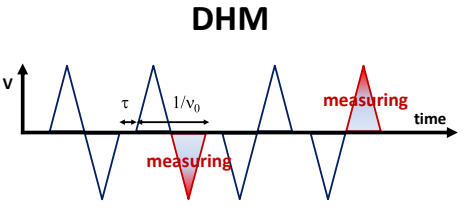

Figure 2.11: *Voltage train pulses that are applied in DHM, shaded areas correspond to the pulses at which the current measurement is performed. ν_0 corresponds to the measurement frequency and τ to the delay time between pulses.*

in literature and it has also been used in order to make easier the description and comparison of the data.

In the following sections (i-iv) sections we describe:

- i) the measurement of ferroelectric I-V loops.
- ii) the extrinsic contributions to ferroelectric loops.
- iii) the PUND compensation technique.
- iv) the DLCC compensation technique.

i) Ferroelectric I-V loops

The measurement of an I-V loop consists in applying a time-dependent electric field on the sample while recording the current. The electric field is usually successively cycled from $-E_{MAX}$ to $+E_{MAX}$. Note that the charge change between P^+ and P^- (ΔP) produces a current that depends on switching time as $I = \frac{\Delta P}{\Delta t}$. Therefore, the resulting current peak is larger if the cycling of the electric field is done faster.

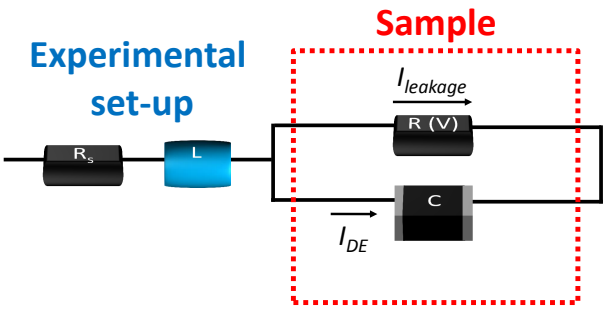

Figure 2.12: *Equivalent circuit on ferroelectric measurements.*

I-V loops in the present work have been recorded using the so-called Dynamic Hysteresis Mode (DHM) [86]: four bipolar triangular excitation signals of frequency ν_0 are applied with delay time ($\tau = 1$ s in our case) between them, as shown in figure 2.11. The first (third) bipolar voltage (V) pulse pre-polarizes the sample in the negative (positive) state. The final I-V loop is obtained from the combination of the currents measured while applying the negative voltage during the second pulse and the positive voltage during the fourth pulse (negative and positive voltages, respectivily), as indicated in figure 2.11 (shaded areas). The first and the third pulses are necessary in order to obtain the same measurement conditions while recording the positive and the negative part of the final loop. This method is specially convenient because it does not continuously cycle the sample, avoiding the aging (fatigue).

ii) Extrinsic effects in ferroelectric hysteresis loops

The simplest equivalent circuit corresponding to the measuring set-up is shown in figure 2.12, where all the contributions to the measured current are indicated. Basically, we can discern between the contributions arising from the sample and the contributions due to the experimental set-up. The sample may be regarded as a lossy capacitor (RC element, equal to what is shown in

the previous section 2.2), and therefore it produces two current contributions: the displacement current ($I_{DE} = \frac{\partial D}{\partial t}$), and that arising from leakage ($I_{leakage}$).

$$I = I_{leakage} + I_{DE} \tag{2.16}$$

As stated by equation 2.1, the electric displacement field contains the vacuum contribution ($\epsilon_0 E$) and the material contribution (P). In a ferroelectric, we can separate P in two terms: one that linearly depends on the electric field (P_χ) and another that is non-linear (P_{FE}):

$$P = P_{FE} + P_\chi = P_{FE} + \epsilon_0 \chi E \tag{2.17}$$

Then, D can be rewritten as:

$$D = \epsilon_0 E + P = \epsilon_0 E + P_{FE} + P_\chi = \epsilon_0 E + P_{FE} + \epsilon_0 \chi E \tag{2.18}$$

$$= \epsilon_0 (1 + \chi) E + P_{FE} = \epsilon E + P_{FE} \tag{2.19}$$

Note that here ϵ has been taken as constant (in fact it is the permittivity at electric fields above the coercive field), and P_{FE} contains the non-linear terms due to the ferroelectric nature of the material.

Therefore, the derived displacement current also contains two contributions:

$$I_{DE} = \frac{\partial D}{\partial t} = \frac{\partial (\epsilon E + P_{FE})}{\partial t} = I_\epsilon + I_{FE} \tag{2.20}$$

where I_ϵ and I_{FE} correspond respectively to the currents derived from ϵE and P_{FE} terms. The current I_{FE} is caused by the ferroelectric domain switching, while the dielectric current I_ϵ corresponds to the charging current of the material, and $I_{leakage}$ is the current caused by the electrons that flow through or come from the sample because it is not a perfect insulator. Contributions

from the experimental set-up are taken into account by L and R_s (inductance and resistance in series respectively), mainly coming from the wiring and electrodes.

In order to clarify the extrinsic contributions that commonly appear in I-V characteristics, a simulation assuming a leaky ferroelectric with low polarization (typical features of multiferroic thin films) has been carried out. In the simulation the voltage has been cycled using constant voltage ramps, thus applying triangular pulses, which is equivalent to the voltage pulse train used in DHM (fig. 2.11). The electric field increases $E_n = E_{n-1} * \Delta E$, where n is each simulated point. Therefore, measured polarization and current are calculated at each n point (P_n and I_n).

The different contributions to the measured current, already discussed, have been implemented by using different models (summarized in table 2.2):

- *Ferroelectric contribution:* After Miller et al. [87], polarization for a common ferroelectric can be written as:

$$P_{FE} = P_0 \cdot tanh(\frac{E - Ec}{\delta}) \tag{2.21}$$

  where δ is a characteristic constant of the ferroelectric, which takes into account the distribution of coercive fields in the material.

- *Dielectric contribution:* Corresponding to the constant part of dielectric permittivity of the ferroelectric.

$$P_\epsilon = \epsilon E \tag{2.22}$$

- *Leakage:* Here we have used a general exponential behavior for the leakage,

$$I_{leakage} = I_0 e^{\frac{E}{E_0}} \tag{2.23}$$

where E_0 and I_0 are characteristic constants. This proposed leakage behavior can effectively describe the most common leakage mechanisms in ferroelectrics. The use of more specific leakage mechanism, such as interfacial Schottky emission [88, 89] or bulk Poole-Frenkel emission [90], will not change significantly the performed analysis.

- *Series resistance effect:* The delay time due to the series resistance is not usually taken into account in ferroelectric measurements. Note that this effect is not the same as the intrinsic relaxation time that occurs in a ferroelectric material during the switching process (see f.i. ref. [91]). The delay induced by the series resistance results in that the intrinsic electric displacement field ($D_{intrinsic} = P_\epsilon + P_{FE}$) of the ferroelectric is not the measured ($D_{measured}$). At each n point $D_{measured}$ can not reach the value of $D_{intrinsic}$ because the resistance in series produces a delay in the charge needed to neutralize the intrinsic polarization on the surface between the ferroelectric and the electrode. Therefore, at each n point $D_{measured}$ would be that similar to that resulting from the charging of a capacitor with a resistance in series [92].

$$Q(t) = Q_f(1 - e^{-t/R_sC}) \tag{2.24}$$

where Q_f is the final charge. The delay is equal to R_sC product.

In the case of a ferroelectric hysteresis loop Q_f wants to be $D_{intrinsic}$. As the initial charge is not zero, we have calculated the $D_{measured}$ at each point (n) of the simulated loop as follows:

$$D_{measured,n} = D_{measured,n-1} + (D_{intrinsic,n-1} - D_{measured,n-1}) * (1 - e^{-t/R_sC}) \tag{2.25}$$

This effect results in a delay of the polarization of the loop. In figure

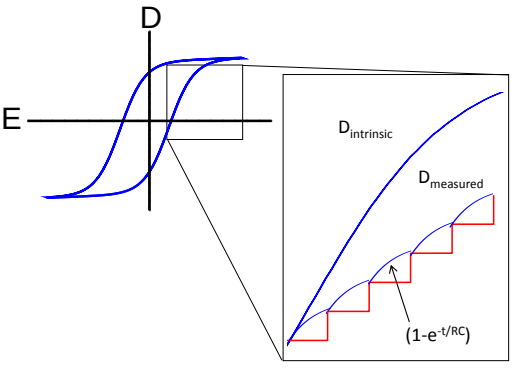

Figure 2.13: *Scheme of the effect of series resistance. Figure shows that in this fragment of the loop $D_{measured}$ is lower than $D_{intrinsic}$ because the provided current is not enough to compensate the surface induced charge due to the series resistance that induces a delay.*

2.13 the $D_{measured}$ that results during the polarization change from P^- to P^+ is plotted. Here, it is clearly seen that (in this particular fragment of the loop) $D_{measured}$ can not achieve the value of $D_{intrinsic}$.

Summarizing, the final measured current, would be:

$$I = I_{leakage} + I_{DE} = I_0 e^{\frac{E}{E_0}} + \frac{\partial D_{measured}}{\partial t} \tag{2.26}$$

In this relation only leakage is a frequency independent term. The $D_{measured}$ would be that obtained after taking into account the series resistance contribution on $D_{intrinsic}$, i.e. applying the equation 2.25 to $D_{intrinsic}$ obtaining $D_{measured}$.

$$D_{intrinsic} = P_\epsilon + P_{FE} = \epsilon E + P_0 * tanh(\frac{E - Ec}{\delta}) \tag{2.27}$$

Simulated D-E and I-V loops using the above expressions are depicted in figures 2.14, for various frequencies. The plotted value is the $D_{measured}$, which

Table 2.2: *Different contributions and parameter values used in the simulated I-V curves depicted in figure 2.14. The area (A) and the thickness (t) of the simulated capacitor have been 0.15 mm^2 and 165 nm, respectively. The used values are similar to those obtained in o-$YMnO_3$ thin film of ref. [93], except R_s which is smaller in order to obtain a wider frequency range without extrinsic effects. The series resistance term is added to the total calculated electric displacement field as shown in equation 2.26.*

Contribution	Term	Parameters
Ferroelectric	$P_{FE} = P_0 \cdot tanh(\frac{E-E_c}{\delta}))$	$P_0 = 0.1\mu C/cm^2$ $E_c = 100kV/cm$ $\delta = 50kV/cm$
Dielectric	$P_\epsilon = \epsilon E$	$\epsilon_r = 40$
Leakage	$I_{leakage} = I_0 e^{\frac{E}{E_0}}$	$I_0 = 10nA$ $E_0 = 50kV/cm$
Series resistance	$Q = Q_f(1 - e^{-t/R_s C})$	$R_s = 10\Omega$

contains all the mentioned contributions. Simulations have been carried out using similar values to those obtained in the characterization of o-$YMnO_3$ thin film in ref. [93], summarized in table 2.2.

The detailed inspection of these D-E and I-V curves (fig. 2.14) provides information on the relevance of the different non-FE contributions to hysteresis as a function of frequency. Three ranges can be clearly distinguished:

- *Low frequency range*: In figure 2.14(b) the I-V curve is dominated by leakage as it can be inferred by the exponential increase of current with electric field (labeled with $I_{leakage}$). This provokes the rugby ball shape in the D-E loop of figure 2.14(a) typical for a short-circuit contact or resistance loops. Since the switching current I_{FE} is proportional to frequency, in samples with important leakage its contribution hinders the observation of the ferroelectric current peak at low frequencies. This can be seen in the small current peaks at coercive field (dashed

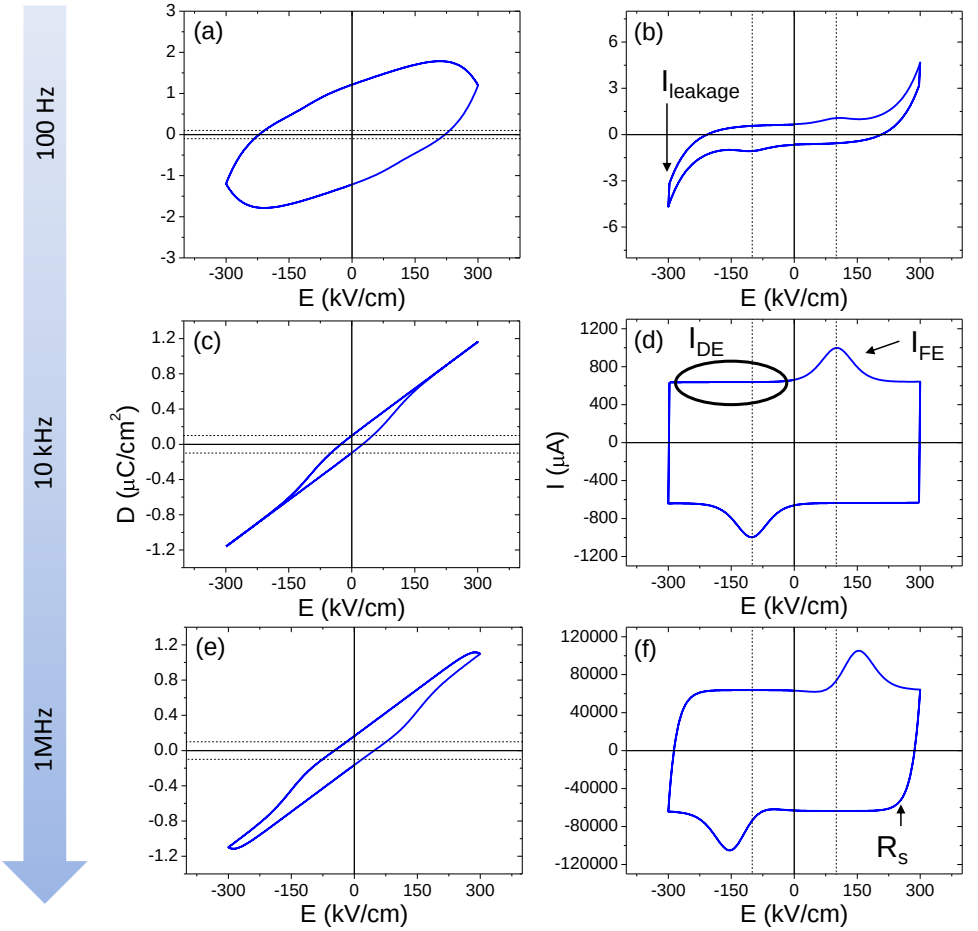

Figure 2.14: *Simulated I-V and D-E loops using the values summarized in table 2.2. The loops have been simulated at 100 Hz (a,b), 10 kHz (c,d) and 1 MHz (e,f).*

lines), which in a real measurement can be below the current noise and, therefore, impossible to distinguish. As a consequence, this frequency range is not suitable to obtain reliable values of polarization. The coercive field extracted from D-E loop would be also overestimated [as inferred from fig. 2.14(a)]. However, this does not apply if the coercive field is taken as the electric field at which the ferroelectric current peak takes place.

- *Middle frequency range*: As frequency increases the D-E loop becomes gradually free of extrinsic contributions [figure 2.14(c)]. This is because, as it can be inferred from I-V loops of figure 2.14(d), two other contributions become more important than leakage: (i) the dielectric current (I_ϵ) of the capacitor, which can be identified because it is field independent, and (ii) the ferroelectric switching current peak, coming from I_{FE}. Both currents are proportional to frequency; thus, the frequency increasing provokes that leakage becomes progressively less important. That is the reason why figure 2.14(c) can be ascribed to a genuine ferroelectric loop, being ideal to extract polarization and coercive field values. However, this loop differs from a text-book example in the non-saturation of the D at high fields. This is because the dielectric contribution $P = \epsilon E$ is always added to the "pure" ferroelectric polarization. Here, it is well visible because both contributions (P_{FE} and P_ϵ) are comparable. This is not the case of a standard ferroelectric, in which $\frac{\epsilon E}{P_r}$ coefficient is nearly zero. This results in a more square-like loop; however, the ϵE slope should be always present.

- *High frequency range*: As frequency is further increased, the D-E loop becomes wider again [figure 2.14(e)]. This is because another extrinsic contribution appears. First, in figure 2.14(f) a non abrupt change in the sign of I_ϵ can be observed when the change of field derivative occurs (this means, where electric field reaches its maximum and starts to

decrease, labeled R_s in the figure); this contribution comes from the series resistance of the instrumental set-up. This results in the vertical widening of the D-E loop. Second, and more dramatic, is the fact that the coercive field is larger than the intrinsic one (dashed line), which results in the horizontal widening of the D-E loop. This is also because of the series resistance, which delays the current needed to allow the polarization sign change at E_c, resulting in a non-intrinsic variation of E_c .

Besides this, actual I-V curves can develop a tail at higher applied fields [93]; this is due to the circuit inductance L, which introduces a time shift between current and applied voltage. Extrinsic contributions due to series resistance usually appear at lower frequencies than this inductance contribution. Therefore, L becomes important only at much higher frequencies, beyond what it has been called *high frequency range*, and that is the reason why we have not included this effect in our simulations.

From the measured D-E loops at any frequency, the remanent polarization, P_r, can be extracted. The obtained values for the simulations are shown in figure 2.15(a). As expected from the above discussion and from the inspection of figures 2.14, at low frequencies P_r is overestimated because of the leakage contribution; this overestimate decreases for increasing frequencies, as the weight of the leakage contribution is reduced; finally, P_r reaches a constant value at frequencies where the effect of losses may be considered irrelevant. Figure 2.15(a) shows as well that at high frequencies P_r is again being overestimated. Now, it is because of the effect of the resistance in series.

A similar analysis can be done for E_c. In figure 2.15(b), the dependence on frequency of E_c is plotted. As mentioned, E_c is taken as the electric field where the ferroelectric current peak occurs. From the figure, it can be inferred that in the low frequency range E_c can be always safely extracted. However, in the high frequency range, E_c is overestimated due to series resistance, as

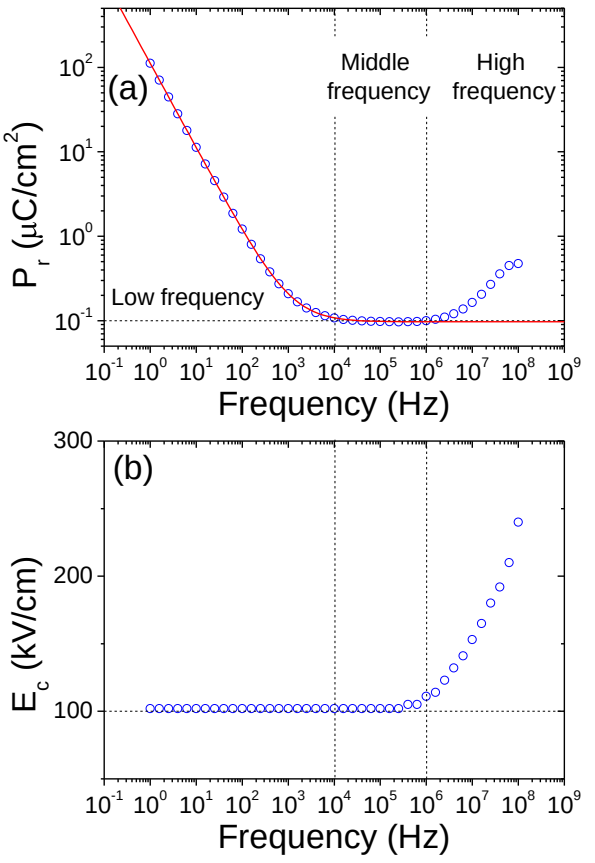

Figure 2.15: *Frequency dependence of the remanent polarization (a) and coercive electric field (b) for loops simulated at various frequencies with values of table 2.2. The solid lines are fits to equation 2.32.*

we have already discussed.

Now, let us focus on the overestimate of P_r in the low frequency regime due to leakage. Since the actual ferroelectric remanent polarization (in this section called $P_{r,0}$) should be frequency independent, and assuming frequency independent losses [94], we can try to separate both contributions to the measured remanent polarization. Therefore, the measured remanent polarization P_r including the leakage contribution can be written as:

$$P_r = P_{r,0} + P_{leakage} \tag{2.28}$$

If we assume leakage current symmetric and non-hysteretic, for the positive polarity of a triangular pulse we have:

$$2 \cdot P_{leakage} = \int_0^{t_f} I_{leakage}(V(t))dt = \int_0^{t_f} I_{leakage}(V)\frac{dt}{dV}dV \tag{2.29}$$

where $t_f = \frac{1}{2\nu}$ is the duration time of the triangular pulse, and $\frac{dt}{dV}$ is the inverse of the voltage ramp, which is constant in a triangular pulse ($\frac{dt}{dV} = \frac{V_{max}}{1/2\nu}$). As we assume that the loop is symmetric, we only need to integrate $1/2$ of the loop, which corresponds to the positive applied field. Therefore, the integral can be written as:

$$2 \cdot P_{leakage} = \int_0^{halfloop} I_{leakage}(V)\frac{V_{max}}{1/2\nu}dV \tag{2.30}$$

and, finally

$$P_r = \frac{1}{2}\frac{V_{max}}{1/2\nu} \cdot const. \equiv \frac{\overline{Q}}{\nu} \tag{2.31}$$

where $\overline{Q}$ is defined as the integrated leakage charge per time and area units. Thus equation 2.28 can be written:

$$P_{leakage} = P_{r,0} + \frac{\overline{Q}}{\nu} \tag{2.32}$$

This expression reveals that the contribution of leakage to the measured remanent polarization decreases with $1/\nu$, as observed in data of figure 2.15(a). In fact, the dashed red lines in figures 2.15(a) are fittings of the simulated data using equation 2.32. This fitting in a real measurement would allow us to obtain accurate values of $P_{r,0}$ taking into account a wide measured frequency range. Therefore, this is an extended version of the "Dielectric leakage current compensation" (DLCC) technique, discussed in section 2.3.1. We say "extended" because the $P_{r,0}$ value obtained from our fitting would account for the measurements done at various frequencies. Contrary to this, P obtained from DLCC method only accounts for two measurement frequencies.

iii) PUND technique

Positive-Up-Negative-Down (PUND) technique is a well-known method to obtain reliable values for remanent polarization [95]. In the used PUND measurement five voltage pulses are applied to the sample (figure 2.16). The first is negative and pre-polarizes the sample to a negative polar state. The second and the third pulses are positive: the second (P) polarizes the sample and therefore the corresponding current contains the ferroelectric and non-ferroelectric contributions, while current during the third (U) pulse only contains the non-ferroelectric contributions; therefore, their subtraction allows to obtain, in principle, only the ferroelectric contribution. The same applies for the fourth (N) and fifth pulses (D), for the negative state, so that the current loop $I_{PUND} - V$ is obtained from $I_P - I_U$ for the positive voltages and from $I_N - I_D$ for the negative voltages. Consequently, PUND current only contains the switchable ferroelectric contribution and all the other contributions are excluded, $I_{PUND} = I_{FE}$; even I_ϵ contribution, which is also intrinsic from the material, is excluded.

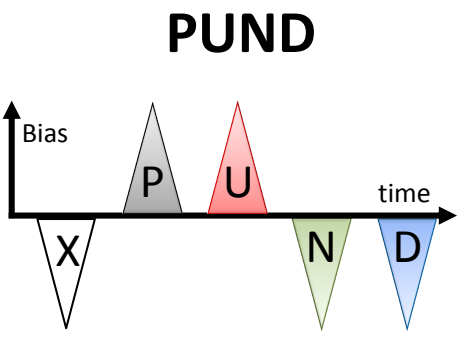

Figure 2.16: *Voltage train pulses during PUND (Positive-Up-Negative-Down).*

This compensation technique should be used only if accurate values of remanent polarization are needed or in the presence of large leakage. However, it has been demonstrated that it is not absolutely effective in presence of leakage [93], yielding to an overestimation of remanent polarization. The physical mechanism that induce this overestimation has not been yet elucidated.

Estimated error of the P_r obtained by PUND

To obtain an accurate error bar in PUND technique is important since FE peak may be very weak and the noise of the measured current can influence the final obtained value. We propose a method to evaluate the error on remanent polarization measured by PUND, taking into account the different error sources that can be present in the measurement. The charge is simply calculated as follows during the integration of the measured current:

$$Q(i) = Q(i-1) + (t(i) - t(i-1)) \cdot I(i) + \frac{(I(i) - I(i-1)) \cdot (t(i) - t(i-1))}{2} \tag{2.33}$$

where i corresponds to the integration step. During the integration of the PUND current that results in the D-E loop the propagation of the error of

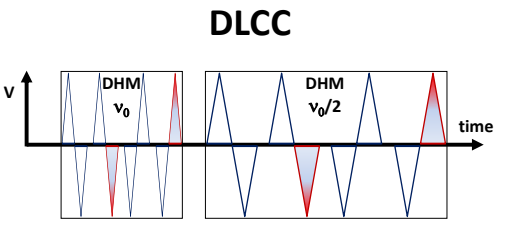

Figure 2.17: *Voltage train pulses during DLCC (Dielectric Leakage Current Compensation).*

the current noise (roughly 1% of the used measuring current range) and the time step (1/2 of the time between each current measurement) are computed, giving δQ.

The error of the geometry of the capacitor (electrode area) is also taken into account, δA. Therefore, as $D = \frac{Q}{A}$, the experimental δD_{exp} error can be calculated as:

$$\delta D_{exp} = D \cdot \sqrt{(\frac{\delta Q}{Q})^2 + (\frac{\delta A}{A})^2} \tag{2.34}$$

The statistical deviation (normal deviation) of different measurements is also taken into account (δD_{stat}). Finally, the error would be given by:

$$\delta D = \sqrt{\delta D_{exp}^2 + \delta D_{stat}^2} \tag{2.35}$$

iv) Dielectric leakage current compensation

Dielectric Leakage Current Compensation (DLCC) method was a compensation technique developed by Meyer et al. [86, 94]. This is often used when only the leakage contribution is desired to be extracted, thus f.i. to know P_s, PUND can not be used because it extracts the P_ϵ term, so DLCC is necessary.

In DLCC the I-V curves obtained by DHM are corrected for leakage effects using two assumptions: that the leakage current $I_{leakage}$ is independent of frequency and that the dielectric current I_ϵ and the current due to the ferroelectric switching I_{FE} are both linearly depending on frequency. Under these hypotheses, measuring the DHM cycles at two frequencies (ν_0 and $\nu_0/2$, figure 2.17) allows subtraction of $I_{leakage}$, and thus only the displacement current remains. Consequently, $I_{DLCC} = I_\epsilon + I_{FE}$, at low and middle frequency range. At high frequencies the series resistance can still affect the loop after the compensation due to its frequency dependent contribution.

DLCC allows to obtain reliable ferroelectric parameters from the D-E loops. However, as we reported in [93], if after the compensation the leakage is not completely compensated the technique can give rise to ambiguous determination of remanent polarization. This happen in cases where $I_{leakage}$ is not frequency independent, and/or I_{DE} does not depend linearly on frequency.

Summarizing, we have seen that the presence of extrinsic contributions in I-V loops can be well subtracted by measuring loops in a wide frequency range. Moreover, hints and methods about how the extrinsic effects can be avoided have been given.

2.3.2 ϵ-E and ϵ-T dielectric measurements

Ferroelectric characterization can also be made by measuring the dielectric permittivity. Contrary to dielectric measurements and impedance spectroscopy, already explained in detail, here we measure the dielectric permittivity while cycling an applied electric field (ϵ-E), or changing the sample temperature (ϵ-T).

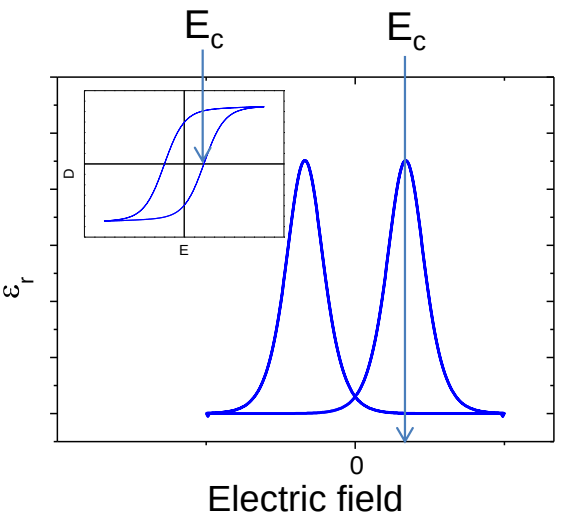

Figure 2.18: *ϵ-E loop for a standard ferroelectric. (inset) D-E loop for a standard ferroelectric.*

i) ϵ-E loops

The dielectric permittivity and losses can be calculated from the impedance (chapter 2.2). If a voltage bias is applied to the sample ($V(t) = V_{bias} + V_0 sin(\omega t)$), the dependence on electric field of the impedance and consequently of the dielectric permittivity can be obtained. Ferroelectric samples display a characteristic "butterfly loop" in their ϵ-E (equivalent to C-V) curves, because the dielectric permittivity should display a divergence near the coercive field (fig. 2.18). In this measurement the sample is cycled from the maximum applied field (E_{MAX}) to $-E_{MAX}$ and from $-E_{MAX}$ to E_{MAX}.

The ϵ-E measurement is not exactly equivalent to the hysteresis measurement (P-E loop). In a capacitance-voltage measurement a static bias is applied and the capacitance measured, whereas in a hysteresis measurement the voltage is being varied in a continuous way. Therefore, ϵ-E measurement is almost static ($\nu \to 0$) and leakage effects, if present, can not be avoided, so it is not strictly true that $\epsilon = \frac{dP}{dE}$, since the frequency is not the same

in measurements of ϵ and P, which can change the resulting values. Consequently, interpretation of these results must be taken carefully, as artifacts can arise from many contributions and, even when this is not the case, elements of the system (electrodes, grain boundaries, leads, etc.) can contribute to the impedance in complex ways (f.i. a change in the capacitance with field can arise from change in the depletion width with negligible changes in ϵ). Therefore, the ϵ-E can not be considered as the most suitable tool to extract ferroelectric parameters as P_r or E_c. However, it is a very useful complementary measurement since some of the artifacts that can appear in ferroelectric hysteresis loops, such as back to back Schottky diode [96] or, simply, a lossy linear dielectric [84], would never produce an hysteresis in ϵ-E characteristics.

ii) ϵ-T dependence

The measurement of dielectric permittivity as a function of temperature is also a common approach to identify a phase transition in a ferroelectric material. Here, we measure again the dependence of the impedance on temperature, and after that the ϵ-T curve is calculated. This technique allows to infer the temperatures at which ferroelectric transitions take place. This is because, either if the transition is first or second order, the permittivity of the ferroelectric near the transition presents a huge increase due to the large correlations that the system presents near these critical points.

Frequency independent peaks displayed in ϵ-T characteristics should be taken as a signature of FE transition (in most common cases). However, in bulk [97] and in thin films [76] there are significant complications, such as Maxwell-Wagner effect, that can produce fake transitions, or fake shifts in the temperature at which the dielectric peak takes place [98].

2.3.3 Pyrocurrent

To complete ferroelectric characterization pyrocurrent measurements are also a useful technique. This old technique [99] allows to know the dependence of ferroelectric polarization on temperature.

In pyrocurrent measurement the sample is cooled from a temperature above the transition temperature under the application of an electric field (with the electrometer), resulting in a poled sample at low temperature. Afterwards, the sample is connected to an electrometer that measures the current while the sample is being heated (this means that the current goes through the electrometer from one plate to the other plate of the capacitor). During the sample heating at a well defined heating rate ($dT/dt = const.$), the material goes through the transition, it depolarizes inducing a current that goes through the electrometer from one plate to the other plate of the capacitor. From the integral of this current through time, the charge (polarization) dependence on temperature is extracted.

One of the main advantages of this technique is that it does not require the application of large electric fields. In fact, while measuring the polarization, no electric field is applied avoiding the leakage contribution. However, obtaining well-defined and reliable current peaks requires high polarization values, long retention times (which means that polarization should be retained at least during the measurement time) and high heating ramps.

2.4 Magnetoelectric coupling characterization

In the previous sections we have described in detail dielectric and ferroelectric measurements performed, and the protocols used to analyze the obtained data. However, with the purpose of achieving the final goal of the thesis, magnetoelectric coupling needs also to be characterized. In this section we describe the measurement of dielectric and ferroelectric properties under

applied magnetic field, which will be the tool used to evaluate the presence of magnetoelectric coupling.

We have emphasized the analysis of the data obtained in the dielectric permittivity dependence on magnetic field, since this technique usually can lead to measure misleading artifacts that can result in erroneous determination of magnetoelectric nature of the material under study.

2.4.1 Magnetodielectric measurements

Magnetodielectric measurement consists in the measurement of the variations of the dielectric permittivity as a function of an external applied magnetic field. First, we define magnetodielectric variation ($\Delta\epsilon$), or equivalent magnetocapacitance (ΔC) as the variation of permittivity (capacitance) under applied magnetic field:

$$\Delta\epsilon = \frac{\epsilon(\mu_0 H) - \epsilon(\mu_0 H = 0)}{\epsilon(\mu_0 H = 0)} \tag{2.36}$$

Equivalently, magnetolosses ($\Delta tan\delta$) are defined.

Finally, we define the magnetodielectric coefficient χ_E[3] as the the magnetocapacitance variation per magnetic field unit.

$$\chi_E = \frac{\epsilon(\mu_0 H) - \epsilon(\mu_0 H = 0)}{\epsilon(\mu_0 H = 0) \cdot \mu_0 H} = \frac{\Delta\epsilon}{\mu_0 H} \tag{2.37}$$

Magnetodielectric effect without magnetoelectric coupling

Strong magnetodielectric effects can also be achieved through a combination of magnetoresistance and the Maxwell-Wagner effect, unrelated to true magnetoelectric coupling [81, 100–103]. Analysis of the impedance spectra by means of equivalent circuit for different applied magnetic fields is imperative

[3]Note that this is not the conventional magnetoelectric coefficient defined as $\alpha_E = \frac{dV}{dH}$.

to disclose non-genuine magnetoelectric effects.

First, impedance spectroscopy allows to identify the presence of Maxwell-Wagner behavior. If there is not Maxwell-Wagner effect the magnetoresistance can not lead to any huge magnetodielectric effect; consequently if magnetodielectric effect is measured it can be taken as reliable. This only happens while measuring highly insulating samples, where the extrinsic effects contribute only slightly to the final measured impedance (f.i. samples measured in chapter 3).

Otherwise, in presence of Maxwell-Wagner effect the results obtained by the equivalent circuit fitting of the impedance spectra at various magnetic fields allow us to distinguish which contribution is the main responsible for the measured magnetodielectric effect (f.i. samples measured in chapter 4). Our protocol consists in the fit of the impedance spectrum at various magnetic fields, with the previous identification of the bulk contribution (intrinsic from the material). The bulk contribution is often equivalent to a RCPE equivalent circuit. Then, the resistance element (R) is ascribed to the conductivity of the material, and the constant phase element (CPE) to the dielectric permittivity (with both real an imaginary part), using the equations 2.13. If a substantial variation of the resistance (ϵ-H) or (R-H) is found, we conclude that it is because of intrinsic magnetodielectric or magnetoresistive effect, respectively.

Note that this protocol allows to safely infer if some magnetoresistive or magnetodielectric contribution is present, but not to discard if their are not present. This is because in these cases the found variations are below the error bar of the fitted values.

As Catalan stated in ref. [81], huge magnetodielectric effect can be measured in presence of Maxwell-Wagner behavior and a magnetoresistive contribution. In figure 2.19 the dependencies of the magnetodielectric effect ($\Delta\epsilon$) and magnetolosses ($\Delta tan\delta$) as a function of frequency for two particular examples of magnetoresistance are simulated. The response of the double RC circuit has been computed by using typical element values obtained in

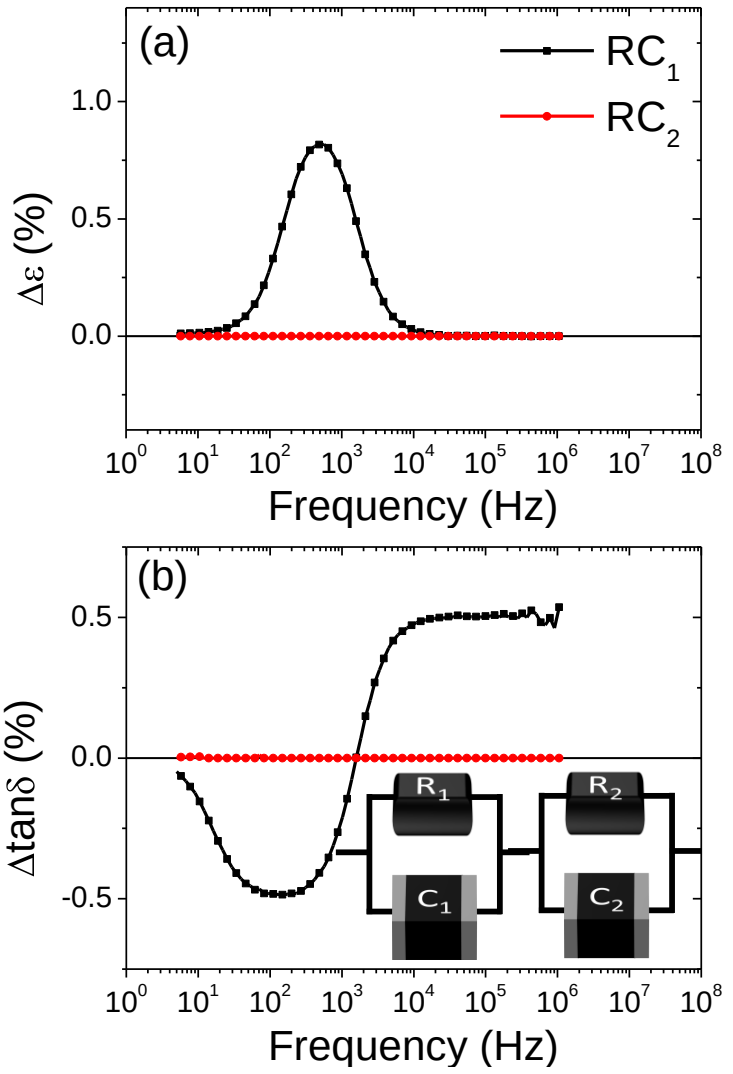

Figure 2.19: *Calculated magnetocapacitance (a) and magnetolosses (b) at different frequencies, for the sketched equivalent circuit where the resistance of the RC_1 (line with squares) and RC_2 (line with circles) is decreased in 100 Ω, simulating a magnetoresistive contribution. Values for the equivalent circuit are RC_1 = 100 pF, 100 kΩ and RC_2 = 10 nF, 10 MΩ.*

multiferroic thin films (RC_1 = 100 pF, 100 kΩ and RC_2 = 10 nF, 10 MΩ). Additionally, we have assumed that the total resistance can vary below ≈ 0.005%, which implies a variation of the resistance of 500 Ω. Under this condition, the outgoing magnetodielectric effect would be due to magnetoresistance, and it would not be easy to be measured with a magnetoresistive measurement. However, we have computed the effects of such a variation in either element of the circuit (RC_1 and RC_2). By modifying the resistance of the high resistive RC element (RC_2), no magnetocapacitive effect is observed (line with circles). However, if we modify the resistance of the low resistive RC element (RC_1) a peak in the magnetocapacitance of around 1 % arises at some frequencies (line with squares), and the magnetolosses are zero at the frequency where the magnetocapacitance peak takes place. As corollary, it follows that the presence of a Maxwell-Wagner behavior and magnetoresistance may mask any genuine magnetoelectric effect.

2.4.2 Ferroelectric loops under magnetic field

This method consists in measuring ferroelectric hysteresis loops under magnetic field. If the measured hysteresis loops are free of extrinsic effects, as discussed in section 2.3, measuring them under different applied magnetic fields can not yield to fictitious variations of ferroelectric order.

2.4.3 Magnetocurrent

The so-called magnetocurrent measurement is equivalent to that of pyrocurrent, but here the temperature is fixed and the polarization is measured while varying the magnetic field. In magnetocurrent measurements the sample is poled at certain magnetic field; afterwards, it is connected to an electrometer that measures the current while the magnetic field is modified at well-defined rate ($dH/dt = const.$). When the material goes through a transition, it depo-

larizes inducing a current that goes through the electrometer from one plate to the other plate of the capacitor. From the integral of this current through time, the charge (polarization) dependence on magnetic field is extracted.

Magnetocurrent measurement is used to know the polarization changes under the application of a magnetic field, contrary to what happens in the measurements of the ferroelectric loops dependence on magnetic field, where the P-H curve can not be obtained due to the poling of the sample while measuring. Moreover, it presents the advantage that no electric field is applied while measuring, avoiding the leakage contribution.

Part III

Results

Chapter 3

Magnetic multiferroic: Orthorhombic $YMnO_3$

Orthorhombic $REMnO_3$ (RE = Y, rare-earth) oxides have fuelled a lot of research efforts because of their interesting multiferroic properties, stemming from their particular antiferromagnetic ordering that can result in ferroelectricity, and the subsequent inherent strong coupling between both ferroic orders.

For large RE (i.e. $LaMnO_3$), the Mn-O-Mn bond angle and the a/b (where a,b,c are the cell parameters, for $LaMnO_3$ a=5.5367, b=5.7473, c=7.6929 [104]) ratio are large ($a/b = 0.963$), indicating a small distortion of the cell. For these compounds the antiferromagnetic structure is collinear A-type (the first neighbor interactions within the ab-plane are ferromagnetic but antiferromagnetic along the c-axis). As the size of the RE is reduced (i.e. $TbMnO_3$), the distortion increases leading to the closing of the bond angle, and a reduction of a/b ($a/b = 0.907$ [104]). This distortion favors the magnetic interactions among next-neighbours within the ab-plane (antiferromagnetic in nature); consequently, there is an increasing competition of magnetic interactions, which yields to the stabilization of a cycloidal magnetic order, which will be detailed below. When the size of RE is further reduced (i.e.

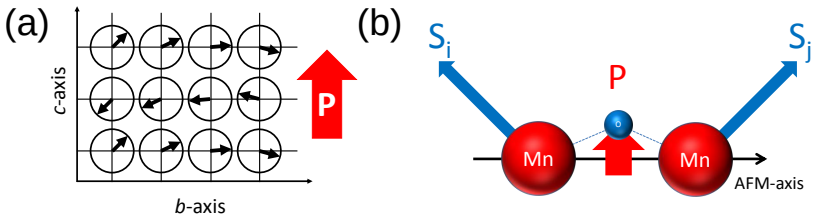

Figure 3.1: *(a) Sketch of the magnetic cycloidal alignment for $TbMnO_3$ adapted from ref. [108] (b) Sketch of microscopic mechanism origin of creation of electric dipole in a cycloidal antiferromagnet, adapted from ref. [109].*

$HoMnO_3$) the bond angle and a/b lower further ($a/b = 0.901$ [104]). In this latter case the in-plane magnetic structure turns to a collinear E-type order (explained below). From the three possible magnetic arrangements depending on RE, ferroelectricity can only exist in E-type or cycloidal magnets.

i) E-type magnetic ordering

E-type magnetic order shows characteristic ferromagnetic zig-zag chains along the a-axis and antiferromagnetic coupling along the b-axis. Ferroelectricity in the collinear E-type antiferromagnets is driven by the asymmetric magnetostriction along the b- and a-axes which breaks the center of symmetry of the lattice producing a characteristic finite polarization along the a-axis [34]. In these materials the expected magnitude of the polarization is of the order of 1 $\mu C/cm^2$; larger than the reported results in bulk, around 100 nC/cm^2 [105–107].

ii) Cycloidal magnetic ordering

More complex is the case of cycloidal magnetic order [2, 19, 110, 111]. In cycloidal spin magnetic alignment the atomic spins rotate[1] across the lattice

[1]Note that "spins rotate" refers to a spacial change of orientation, not temporal. Thus the spin vector remains static, and the rotation refers to the rotation of one spin with respect its neighbor.

as depicted in 3.1(a). This non-collinear magnetic order was reported for the first time by Kenzelmann et al. [108] in $TbMnO_3$ by neutron diffraction experiments. In $TbMnO_3$ the propagation vector of the cycloid is along the antiferromagnetic axis (b-axis, Pbnm notation) and the spins rotation plane is contained in the bc-plane.

Katsura, Nagaosa, and Balatsky [109], based on the duality of electricity and magnetism, suggested that the spin current (proportional to its chirality $\mathbf{Q}_{ij} = \frac{\mathbf{S}_i \times \mathbf{S}_j}{|\mathbf{S}_i \cdot \mathbf{S}_j|}$) could be a source of electric dipole moment in an insulator, as sketched in figure 3.1(b). The outgoing polarization would be that resulting from the expression:

$$\mathbf{P} = A \sum \mathbf{r}_{ij} \times (\mathbf{S}_i \times \mathbf{S}_j) \tag{3.1}$$

where $\mathbf{r}_{ij}$ is the vector (the propagation vector) connecting the spins $\mathbf{S}_i$ and $\mathbf{S}_j$. The A coefficient takes into account the spin-orbit coupling; consequently, spin-orbit coupling is determining the intensity of the coupling between magnetic and electric order, and polarization magnitude.

Later, Sergienko, and Dagotto [112] suggested that the inverse Dzyaloshinsky-Moriya effect [113, 114] would provoke the displacement of the oxygens through the lattice, as sketched in figure 3.1(b), which results in the formation of an electric dipole. The polarization would be that resulting from the same expression obtained by Katsura et al. (eqn. 3.1).

Therefore, both theories point to the same equation 3.1, showing that polarization should emerge contained in the plane of the cycloid and perpendicular to its propagation vector. This has been already observed in $TbMnO_3$ [2], where polarization emerges along the c-axis and the cycloid is contained in the bc-plane.

Cycloidal spin alignment in $REMnO_3$ has been only reported to be contained in the bc-plane in pure $REMnO_3$, (RE=Tb, Dy in ref. [115]). However, some mixed compounds (f.i. $Eu_{1-x}Y_xMnO_3$ [116]) show cycloidal spin align-

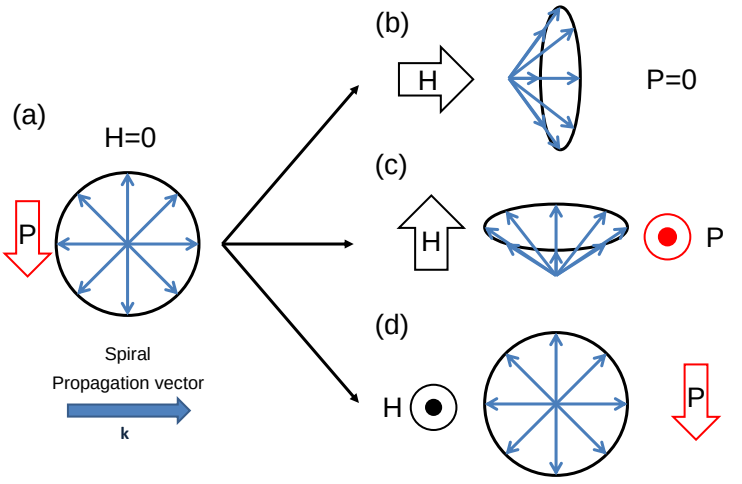

Figure 3.2: *Sketch of the behavior of the spiral order under magnetic field. (a) In zero field spins rotate in a defined plane. (b,c) A magnetic field applied in the plane of the spiral induces a change on its rotation plane. The resulting rotation plane is always perpendicular to the applied magnetic field. (d) If the magnetic field is applied perpendicular to the rotation plane no-effect is expected. In the case, where the invers Dzyaloshinsky-Moriya effect is present, this effect would result in the change of the direction (flop) of the electric polarization vector by 90^o as indicated by arrows, in the case of fig. (c) and a suppression of polarization, in the case of fig. (b). Adapted from ref. [117].*

ment contained in the *ab*-plane with the resulting ferroelectric polarization along the *a*-axis.

Spiral spin alignment can change its rotation plane by the application of a magnetic field in the plane of the spiral; this effect has been called flop [2]. In figure 3.2(a), a cycloid has been represented by merging all the spins of one cycloid rotation period in one point in order to better visualize the flop. Let us focus in the case of a magnetic field applied in the cycloid plane and perpendicular to the propagation vector [fig. 3.2(c)]. When a large magnetic field is applied the spins should become aligned with it, consequently spins should display a component parallel to H different from zero. This effect

yields to the change of the rotation plane, now perpendicular to the applied magnetic field. Therefore, the resulting rotation plane would be perpendicular to the applied magnetic field. The same applies for magnetic field applied along the propagation vector (fig. 3.2(b)). In the case of that magnetic field is applied perpendicular to the plane of the cycloid, no flop is expected. The spins rotation plane flop implies that in the case of cycloidal spin alignment and in presence of inverse Dzyaloshinsky-Moriya effect, electric polarization should have the capability to rotate under the presence of magnetic field [117]. The direction of the magnetic field will determine 3 possible final states for polarization:

- If the magnetic field is applied in the plane of the cycloid and in the direction of the propagation vector [fig. 3.2(b)], the resulting magnetic order is a helix. As $\mathbf{Q}_{ij}$ is parallel to $\mathbf{r}_{ij}$, the resulting polarization is zero, according to eqn. 3.1.

- If the magnetic field is applied in the plane of the cycloid and perpendicular to the direction of the propagation vector [fig. 3.2(c)], the resulting magnetic order is a cycloid in the perpendicular plane. Therefore, the resulting polarization changes its direction by 90^o. This is the so-called polarization flop process.

- If the magnetic field is applied perpendicular to the plane of the cycloid [fig. 3.2(d)], the cycloid does not change, thus polarization direction is the same.

The flop process of polarization with these features has been observed in $REMnO_3$ where the RE is non-magnetic $Sm_{0.5}Y_{0.5}MnO_3$ [118], and $Eu_{0.55}Y_{0.45}MnO_3$ [119]. However, this flop process does not occur in the alluded expected way in manganites with a magnetic rare-earth, such as $TbMnO_3$ or $DyMnO_3$ [120]. In these examples flopping occurs while applying the magnetic field

along the propagation vector of the cycloid, therefore it might be reasonable to think that magnetic nature of the RE takes a role in flop process. Mochizuki and Furukawa [121] developed a microscopic theory that explains this non-expected result suggesting that the application of a magnetic field along the antiferromagnetic short axis reduces the Dzyaloshinsky-Moriya energy, through the modulation of the interplane spin angles, which results in the flop of the cycloid to a more stable rotating plane, with the subsequent polarization reorientation.

Summarizing, the different magnetic orders in the $REMnO_3$ have their characteristic signatures in their ferroelectric properties. Whereas those compounds that show A-type magnetic order can not display ferroelectricity, those showing E-type display ferroelectric polarization along the a-axis. In the middle of these are those materials that show cycloidal magnetic order, where polarization is perpendicular to the propagation vector of the cycloid and contained in its rotation plane, and it can be rotated by 90^o by the application of a suitable magnetic field.

Before the beginning of the present thesis not conclusive data were reported on the magnetic structure of o-$YMnO_3$. Whereas very early reports on neutron diffraction of ceramic samples pointed to spiral order [122], more recent results point to E-type ordering [123]. Ferroelectric measurements on bulk ceramics were not conclusive discriminating between a cycloidal or E-type magnetic ordering [105, 106]. At present, it is established that bulk o-$YMnO_3$ is an E-type magnet [61]. This is because ferroelectric measurements in o-$YMnO_3$ single crystals are in agreement with E-type magnetic ordering (Polarization perpendicular to c-axis and no signature of flop process). However, according to Y ionic radii, o-$YMnO_3$ lies at the very verge line between E-type and cycloidal alignment [116], and in thin film form it has been reported that cycloidal and E-type magnetic order can coexist [124]. These results evidence

that subtle changes in the structure of o-$YMnO_3$ can result in a modification of the magnetic order.

Chemical substitution of RE [116, 118, 125, 126] of $REMnO_3$ has been used to obtain controllable changes in the ground magnetic order. Several works report on magnetic properties characterization of thin films of different $REMnO_3$ compounds (i.e. $HoMnO_3$ in refs. [127–129], $TbMnO_3$ in refs. [130–132], and $YbMnO_3$ in ref. [133]). However, careful analysis of strain effects on the magnetic properties have only been done in o-$YMnO_3$ thin films. It has been demonstrated by our group that epitaxial strain effects have most evident hallmarks in their magnetic properties [62, 63]. It has been found that when increasing the epitaxial induced strain, a net magnetic moment emerges; and this has been taken as an evidence of a canted state in the magnetic ordering.

Studies on the cycloidal structure of $BiFeO_3$ suggest that cycloidal order can not be preserved in thin films, because of the presence of epitaxial strain, whose elastic contribution to the magnetic anisotropy annihilates the cycloid [134]. In fact there were not reports on literature pointing to this cycloidal order in $REMnO_3$ thin films.

In the present chapter, we focus on the following studies on o-$YMnO_3$ films: i) the ferroelectric characterization will allow to disclose their magnetic structure (section 3.2), ii) the measurement of the polarization dependence on the magnetoelectric history of the film will give hints on the dynamics of the antiferromagnetic domains (section 3.3), and iii) from the ferroelectric and magnetoelectric characterization of a set of films we will infer the consequences of the epitaxial strain on o-$YMnO_3$ magnetic structure (section 3.4). The samples used to perform these analyses are presented as follows (section 3.1).

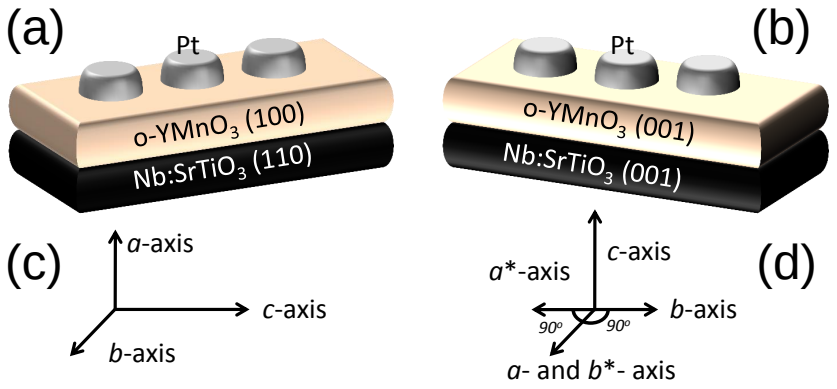

Figure 3.3: *Sketches (a,b) and axis (c,d) of the two families of samples used in the present chapter indicating the o-$YMnO_3$ orientation (in and out of plane) depending on the substrate orientation*

3.1 Samples

Epitaxial films of o-$YMnO_3$ were grown by PLD on (001) or (110) Nb:$SrTiO_3$ substrates (sketched in figure 3.3(a,b)). Information on sample preparation and structural characterization methods for these films can be found elsewhere [62, 135, 136]. o-$YMnO_3$ grows respectively (001) (c-axis) and (100) (a-axis) oriented (Pbnm setting) on these substrates. Structural characterization indicates that *c*-oriented films contain two in-plane 90º-rotated families of crystallites [fig. 3.3(c)], whereas the *a*-oriented are single domain [fig. 3.3(d)].

Because electric measurements are always performed out of plane, dielectric and ferroelectric characterization will be done along the *a*-axis in *a*-oriented films, and along the *c*-axis in *c*-oriented films. For the *a*-oriented samples, the electric measurements have been performed under magnetic field applied along all the crystallographic directions; however, this has not been the case in *c*-oriented samples due to the presence of two in-plane domains; that is the reason why the magnetic field is indicated to be applied along the *c*-axis direction (out-of-plane) or *ab*-plane direction (in-plane).

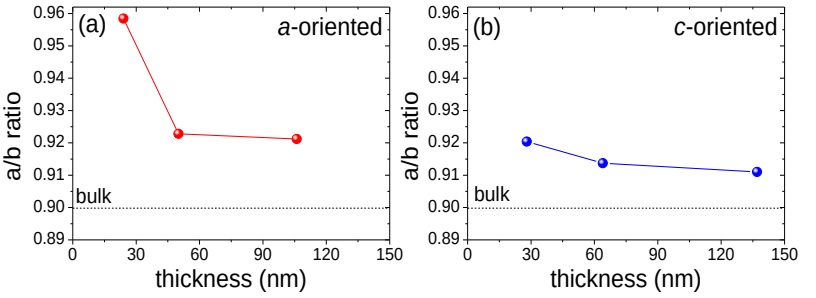

Figure 3.4: *a/b ratio versus thickness for the a-oriented (a) and c-oriented (b) films.*

Table 3.1: *Lattice parameters, and remanent magnetization of o-$YMnO_3$ thin films of different thicknesses. In bulk, (a, b, c)=(5.24560, 5.82980, 7.3295)Å [61].*

Orientation	t (nm)	a (Å)	b (Å)	c (Å)	a/b	M (emu/cm^3)
	106	5.262	5.712	7.453	0.921	2.8
a-oriented	50	5.260	5.700	7.430	0.923	7.9
	24	5.257	5.485	7.837	0.958	15.9
	137	5.260	5.774	7.392	0.911	1.1
c-oriented	64	5.260	5.757	7.393	0.914	1.7
	28	5.260	5.715	7.398	0.920	4.5

Three films with different thicknesses have been studied, for each texture. As the thickness is decreased, epitaxial strain induced by the substrate gradually increases. The lattice parameters and the thickness of these films are summarized in table 3.1. In figures 3.4, it can be seen that all the films have a/b ratio larger than that displayed in bulk, and that as the thickness is increased, the a/b ratio reduces.

Weak-ferromagnetism present in the films has also been previously characterized. As it can be seen in figure 3.5 the ferromagnetism gradually increases for decreasing thickness. This result is in agreement with the previous work

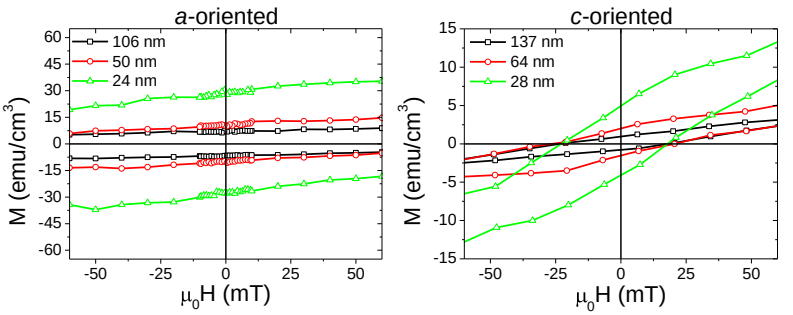

Figure 3.5: *Magnetization versus magnetic field loops recorded at 5K for a- (a) and c-oriented (b) samples. Magnetic fields are applied always out-of-plane, H//a- and H//c- for the a- and c-oriented samples, respectively.*

realized in similar thin films of o-$YMnO_3$ [63].

3.2 Magnetic control of ferroelectric Polarization: cycloidal order in o-$YMnO_3$ thin films

Ferroelectric and magnetoelectric characterization of most relaxed o-$YMnO_3$ thin films of each orientation is now analysed. These correspond to the thickest film for each texture, 105 and 137 nm thick, indicated in table 3.1.

In figures 3.6 ferroelectric measurements have been performed in the *a*-oriented sample under different magnetic fields applied along the *c*-axis. Figure 3.6(a) shows a small hysteresis that can indicate the presence of remanent polarization in I_{PUND}-E characteristics at 0 T. The derived P_{PUND}-E loops (right-axis) indicates that this polarization is around 30 nC/cm^2. This small hysteresis is also present in the loops recorded under applied magnetic field along the *c*-axis of 4 T and 6 T [figs.3.6(b,c), respectively]. However, more remarkable is the ferroelectric current peak that becomes well-visible at 4 T, and progressively increases with the applied magnetic field. The integrated P_a values, consequently, also increase up to 80 nC/cm^2.[2]

[2]For fields above 6 T, polarization start decreasing again; this effect is consequence

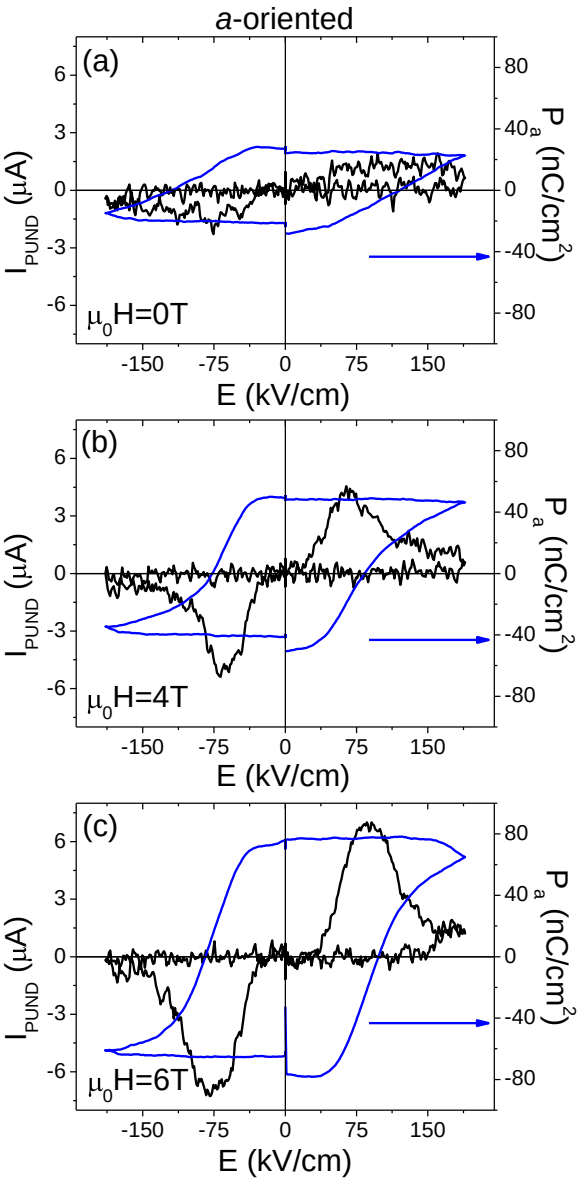

Figure 3.6: *I-E (left-axis) and integrated P-E characteristics (E//a, and H//c) for the a-oriented thin films under applied magnetic field of 0, 4 and 6 T for (a), (b), and (c), respectively. I_{PUND} is the current after PUND subtraction. Measured at 10 kHz and 5 K.*

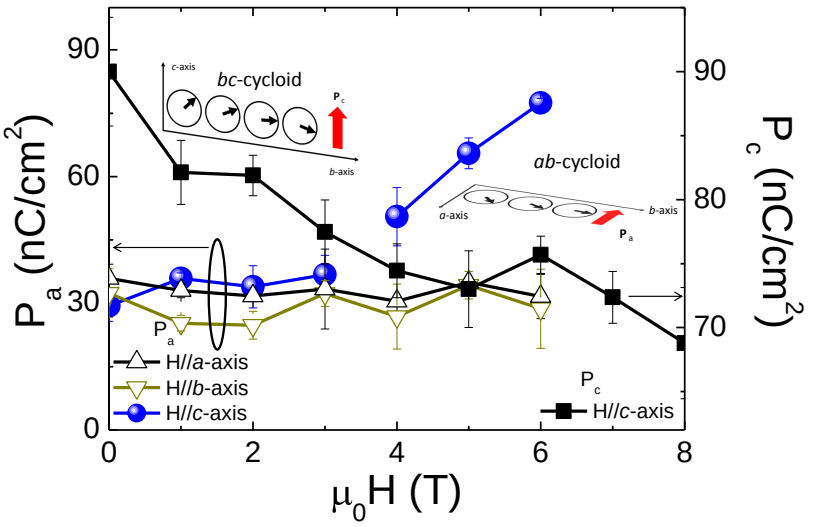

Figure 3.7: *Magnetic field dependence of P_a for $H||c$ (solid circles), $H||a$ (up-triangles), and $H||b$ (down-triangles) and P_c for $H||c$-plane (squares)*

The dependence of polarization on magnetic field along the a- and b-axis is displayed by lines with triangles in figure 3.7. From the figure, it can be inferred that polarization abruptly appears only when applying the magnetic field along c-axis (line with circles).

Ferroelectric measurements have been performed in a c-oriented sample without applying magnetic field. In figure 3.8(a) a clear ferroelectric current peak in the I_{PUND}-E measurement can be observed. Moreover, the obtained polarization ($\approx$90 nC/cm^2) is very similar to the one obtained in the a-oriented sample. This measured polarization does discard the possibility that o-$YMnO_3$ films are E-type because in this ferroelectric polarization would always lie along the a-axis [34, 61].

The data obtained for both samples point to the fact that polarization flops from c-axis to a-axis when a magnetic field is applied along the c-axis.

of the E_c increasing [which can be inferred comparing figs.3.6(b,c)], and, subsequently, with the same applied maximum electric field the polarization loop is not saturated and remanent polarization is underestimated.

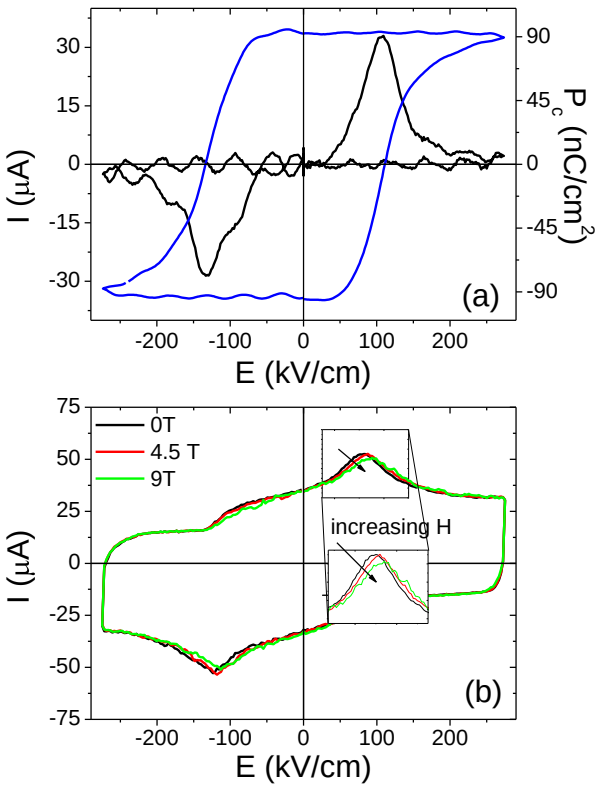

Figure 3.8: *I-E (left-axis) and integrated P-E characteristics (right-axis) for the a-oriented thin films after PUND subtraction. (b) I-E characteristics (DHM) under distinct applied magnetic fields along c-axis. Measured at 10 kHz and 5 K.*

This is in agreement with the previous works in single crystals of $REMnO_3$ [118, 119] where RE is non-magnetic.

However, if the cycloid is contained in the *bc*-plane, P_c should disappear at a similar magnetic field as in the *a*-oriented sample. From the figure 3.8(b), only a slight decrease of the ferroelectric current peak (without applying PUND subtraction) can be observed, even though a total suppression of it was expected. This can be ascribed to the fact that in-plane bi-domain structure of the *c*-oriented film can also suppress the flop effect due to the short coherence length.

Note also the residual polarization ($\approx$ 30 nC/cm^2) observed in the I_{PUND}-E loops of the a-textured film without the application of magnetic field (Fig. 3.6(a)). This could indicate the existence of a minor ferroelectric contribution arising from eventual traces of E-type antiferromagnetic ordering. Because the measured P_a values are much smaller than predicted for E-type antiferromagnets ($\approx$ 2-12 μC/cm^2) [137, 138], this observed hysteresis suggests a minoritary character of such magnetic phase, if present, in the film. This would be consistent with the recent observations of mixed E-type and cycloidal phase in more relaxed o-$YMnO_3$ films [124]. Naturally, this argument would not hold if the maximum polarization of E-type phase were comparable to that reported for polycrystalline samples P_a ($\approx$ 0.5 μC/cm^2) [61, 105, 106]. Alternatively, this residual P_a polarization could be originated from misaligned bc-cycloidal crystallites. Although the presence of these misaligned crystallites with *bc*-cycloidal order can not be excluded [136], their concentration, in principle, could not contribute significantly to the measured hysteresis observed in the I_{PUND}-E loops at fields below 4 T, making less possible this alternative explanation.

In figures 3.9 the dependence of dielectric permittivity on magnetic fields applied along the different crystallographic orientations is displayed for both samples. For both samples the magnetodielectric effect is noticeable. In figure 3.9(a), the *a*-oriented sample shows two remarkable features: i) the

anisotropic response of the dielectric permittivity while applying the magnetic field along the different crystallographic directions, and ii) a dielectric peak at around 4.5 T while applying the magnetic field along the c-axis. In figure 3.9(b), c-oriented sample displays certain anisotropy; however, it is not as remarkable as in the a-oriented sample. Moreover, the well visible dielectric peak present in the a-oriented sample is not present in c-oriented film irrespective of magnetic field orientation. These results are coherent with the magnetic origin of the electric order observed in the studied films. Moreover, the presence of the dielectric peak for the a-oriented film is again a signature of the 90º polarization flop [2, 120]. The hysteresis in the ϵ-H loop is a signature of first order transition, indicating the coexistence of bc- and ab- cycloidal domains near the flopping field.

In fig. 3.9(a), we have observed that the flop of P from c- to a-axis produces a distinctive peak in the dependence of dielectric permittivity on magnetic field. This dielectric peak has been ascribed to the flop magnetic field (H_f). From ϵ-H measurements at various temperatures, the H_f dependence on temperature has been extracted, allowing to build the phase diagram H_f–T shown in figure 3.10. This diagram will help us in next section to explain the magnetoelectric history of the sample in the performed experiments.

The temperature dependence of dielectric permittivity for both samples is shown in figure 3.11(a,b). In these figures one can identify a dielectric peak near the ferroelectric transition. Remarkably, the dielectric peak measured in a-oriented sample under applied magnetic field along the c-axis [3.11(a)] is notably more abrupt that the same peak when the magnetic field is applied along the other directions. While applying magnetic field along the other directions the dielectric peak modifies slightly its height. In the c-oriented sample the dependence on magnetic field direction is very small [fig. 3.11(b)]. This dependence on magnetic field direction is coherent with that observed in the ϵ-H loops.

A final cross-check is the measurement of pyrocurrent for both samples

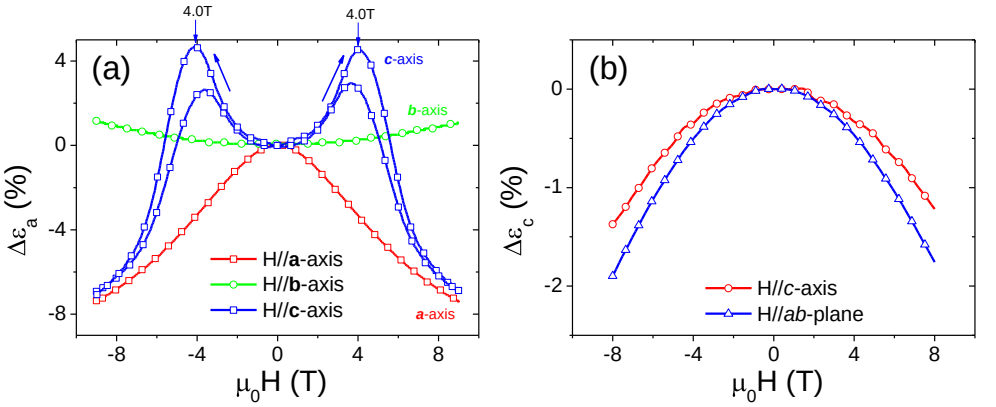

Figure 3.9: *(a) Magnetic field dependence of dielectric permittivity (ϵ_a) at 10 K under the application of a magnetic field along distinct crystallographic directions for a-oriented sample. (b) Idem for c-oriented sample (ϵ_c). $\Delta\epsilon$ corresponds to $\Delta\epsilon = \frac{\epsilon(\mu_0 H)-\epsilon(0T)}{\epsilon(0T)}$. At 100 kHz and 300mV of excitation voltage and at 5K.*

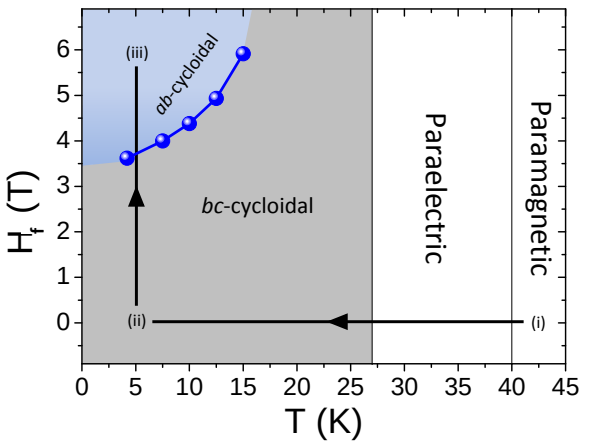

Figure 3.10: *Temperature dependence of the magnetic field required to flop cycloids from bc- to ab- planes (H_f).*

as it is plotted in figure 3.11(c,d). In figure 3.11(c), it can be seen that net polarization emerges at low-temperature for a-oriented sample, while applying a magnetic field of 6 T along c-axis. In figure 3.11(d) net polarization emerges at low-temperature for c-oriented sample.

We have found that o-$YMnO_3$ thin films show typical features of cycloidal magnetic order. This magnetic order permits the control of the polarization vector direction by the application of an external magnetic field, observed for the first time in thin film form. According to our data the cycloid should lie in the bc-plane, and flops to the ab-plane under applied magnetic field along the c-axis.

3.3 Polarization flop and memory effect: Chiral domains configuration

From data displayed in previous section it follows that in the case of $YMnO_3$ thin films studied in the present thesis the polarization changes from c- to a-axis, as a consequence of the flop of the cycloids from bc- to ab- plane. In this section, we would like to go beyond the observation of cycloidal magnetic order, exploring the structure of cycloidal domains, and their dynamics.

In cycloidal magnets multiferroic domains of polarizations, P$\pm c$ (P$\pm a$), are separated by domain walls, DW$\pm c$ (DW$\pm a$) [figure 3.12]. The presence of these chiral domains gives rise to the measurement of hysteresis in the flopping process [139, 140]. As it has been observed in the previous chapter, the H-induced flop transition of cycloids is of first order and thus a competing coexistence of ab and bc cycloids implies the existence of the corresponding domain walls DW$\pm c/\pm a$ in the connecting regions. The dynamics of these multiferroic DW has recently driven much attention due to its relevance on the measured H-dependent gigantic permittivity occurring at the onset of the ferroelectric order [22, 141, 142]. Understanding the formation of the distinct

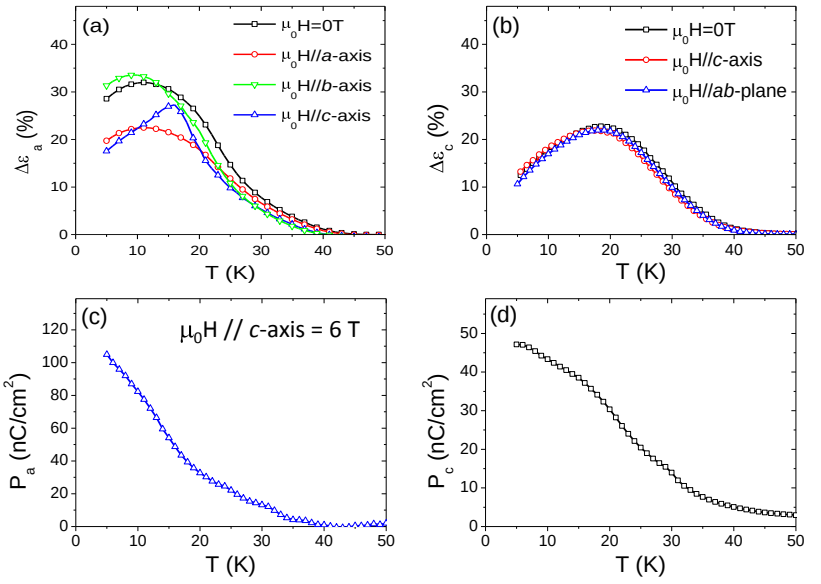

Figure 3.11: *(a,b) Temperature dependence of dielectric permittivity (ϵ_a and ϵ_c, for a-oriented and c-oriented samples, respectively) under the application of a magnetic field along distinct crystallographic directions for a-oriented and c-oriented samples, respectively. $\Delta\epsilon$ corresponds to $\Delta\epsilon = \frac{\epsilon(T)-\epsilon(60K)}{\epsilon(60K)}$. (c,d) Polarization integrated from pyrocurrent measurements for a-oriented and c-oriented samples, respectively. Note that for a-oriented sample (c) the measurement is performed under 6 T of magnetic field. Note also that the polarization value at low temperature obtained for c-oriented sample (panel (d)) is lower than the one obtained by P-E measurement (fig. 3.8), this is because for this sample the retention time for polarization is lower than the duration of the measurement. Dielectric measurements have been performed with 100 kHz and 300mV of excitation voltage. Pyrocurrent measurements have been performed with a heating rate of 20 K/min.*

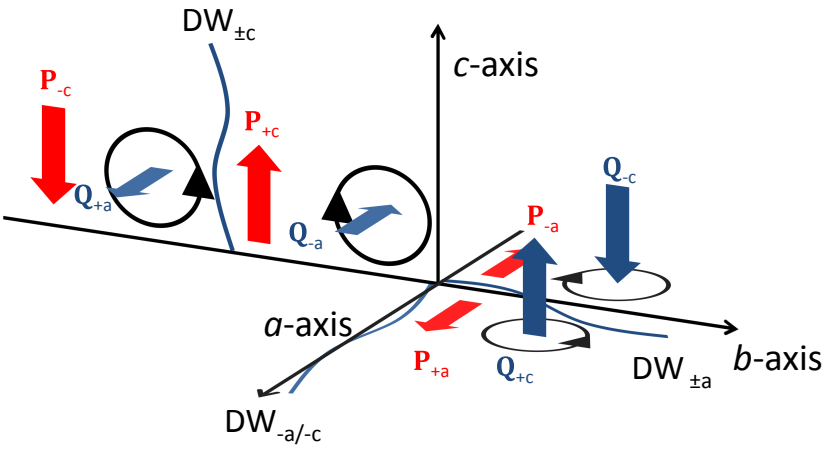

Figure 3.12: *Sketches of the bc- and ac-cycloids (left and right panels); the polar (**P**) and chiral (**Q**) vectors with different sign are indicated.*

chiral domains and the study of chiral domain walls dynamics remains still challenging in cycloidal magnets in thin film form, which is essential for its potential use [143].

The 105 nm *a*-oriented o-$YMnO_3$ thin film grown on Nb:$SrTiO_3$ already used in the previous section and display signature of flopping has been chosen to explore chiral memory effects in thin film.

In order to determine the polar state of the sample we will use a modified PUND measurement. In a standard PUND measurement the complete switchable charge (P) of the material is determined, but the polarization sign can not be extracted, since a pre-polarization pulse is used. Instead, the use of ND [fig. 3.13(a)] and PU [fig. 3.13(c)] train pulses separately without pre-polarizing allows to determine the previous P_+ and P_- polar states. The current is measured during ND [fig. 3.13(b)] or PU [fig. 3.13(d)], consequently the area between these two curves is proportional to the switched charge that was previously pointing to the positive or negative direction, respectively.

In a first set of experiments the sample was cooled down through its Néel temperature (> 40 K) to the measuring temperature (5 K) under electric

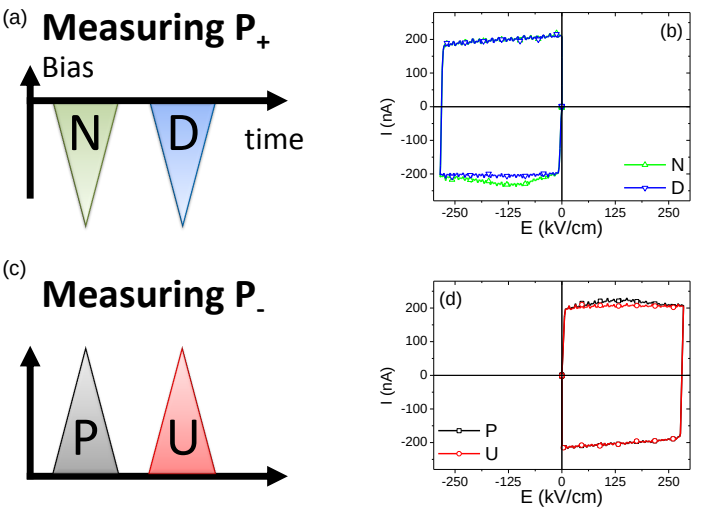

Figure 3.13: *(a, c) Voltage train pulses used during the measurement of negative (PU) and positive (ND) charge, respectively. (b, d) Current recorded during the PU and ND pulses.*

and magnetic zero-field-cooling (E-ZFC and H-ZFC, respectively) conditions [i to ii in fig. 3.10]. Under these cooling conditions positive and negative polar domains are expected to be formed equally, resulting in a zero total measurable polarization. Subsequent application of a magnetic field H>H_f [ii to iii in fig. 3.10] induces flopping of the polarization towards the a-axis [sketched in figure 3.14(a)]. Our aim here is to elucidate whether the formation of these distinct ferroelectric P_{+a} and P_{-a} domains occurs with the same probability. To that purpose we have first measured the I(E) loops using the PUND technique to determine the total amount of switching current (I_{SW}) [Figs.3.14(c,e), squares] and the corresponding charge density P_a = 39(2) nC/cm^2 [proportional to the area under the corresponding I_{SW} loop -dashed regions in figures 3.14(c,e)].

In a subsequent experiment the sample was cycled along the same (i-ii-iii) trajectory (marked in fig. 3.10) and the I-E loops were measured using only a Negative-Down (ND) pulse train to determine the fraction of P_{+a} domains. The results, shown in figure 3.14(b), clearly indicate that the switching current associated to the P_{+a} domains is much smaller than the total switchable current. In fact, the integrated current gives a polarization P_{+a} = 19.1(7) nC/cm^2. This value is close to $\approx 1/2 P_a$ indicating that roughly half the domains have a P||+a as sketched in fig. 3.14(b). This observation suggests that the remaining cycloidal domains should have a similar P_{-a} contribution. This has been verified by cycling again the sample along (i-ii-iii) trajectory and measuring the I-E curves of a Positive-UP (PU) pulse train; the measured current [fig. 3.14(e)] is (in modulus) very similar to that obtained from the ND loops and the corresponding integrated charge is P_{-a} = 20.7(8) nC/cm^2 which is $\approx 1/2 P_a$ [fig. 3.14(d)] thus confirming that P||-a domains coexist in the film in similar number than P||+a domains. This implies, as expected, that both chiralities with opposite sign are degenerated, and one of them can not be selected if no electric field is applied.

Next, we explore the effect of selecting a defined ferroic polarization and

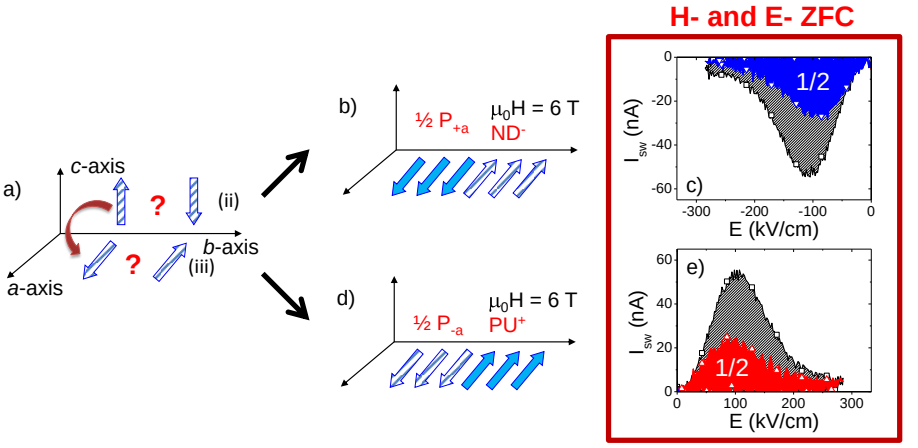

Figure 3.14: *(a) Scheme of the polar state after electric and magnetic zero field cool process and subsequent application of H(6T)||b (flop). "?"'s denote that during this process our experiment does not allow to infer the actual domain configuration of the sample. (b, d) Solid and striped arrows represent the relative fraction of ferroelectric domains measured using the ND and PU signals. (c,e) Switching current versus electric field measured using PUND (squares), ND (down-triangles) and PU (up-triangles). Striped area represents the total amount of switchable charge (PUND) and the solid areas the switched charge during PU or ND measurements.*

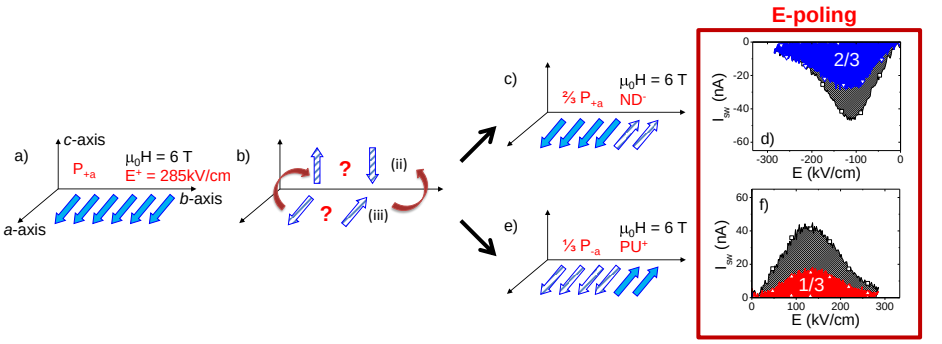

Figure 3.15: *(a) Scheme of the polar state after E-ZFC and H-ZFC process, and E-poling (E//a). "?"'s denote that during this process our experiment does not allow to infer the actual domain configuration of the sample. (b) subsequent application of H(6T)||c-axis (flop). (c, e) Solid and striped arrows represent the relative fraction of ferroelectric domains measured using the ND and PU signals. (d,f) Switching current versus electric field measured using PUND (squares), ND (down-triangles) and PU (up-triangles). Striped area represents the total amount of switchable charge (PUND) and the solid areas the switched charge during PU or ND measurements.*

thus determining the chiral state by E-field poling. For that purpose, the film is cooled down (H-ZFC and E-ZFC) to the measuring temperature (5 K) along i to ii trajectory [fig. 3.10], where a random distribution of polar domains with P$||c$ is likely to be formed. Subsequent application of 6 T magnetic field (H>H_f) (ii-iii) promotes the formation of polar domains with P$||a$ with a random distribution, as it was shown in the previous experiment. E-poling is now done by application of a large enough electric field E$||a$ (E_{+a} = 285 kV/cm) to set a single domain ferroelectric state of a given polarity [sketched in fig. 3.15(a)]. A complete PUND pulse train is used to determine the total amount of switchable charge [fig. 3.15(d,f), squares]; the corresponding charge density P_a = 38(2) nC/cm^2 [dashed regions in figures 3.15(b,c)] is very close, as expected, to that measured in the similar experiment described above (P_a ≈ 39(2) nC/cm^2).

Next, the magnetic field is reduced to zero (polarization should flop back to c-axis) and increased again to the same value (6 T) [fig. 3.15(b)], and the ND train is used to determine the fraction of P_{+a} domains [fig. 3.15(c)]. The results, shown in fig. 3.15(d), clearly indicate that the switching current associated to the P_{+a} domains is smaller than the total switching current. It is remarkable that the integrated current (proportional to the area under the I_{SW}(E) curve) gives a polarization P_{+a} = 25(1) nC/cm^2 which is about ≈2/3P_a. This result indicates that about 2/3 of the film was constituted by domains with polarization P_{+a} [sketched in fig. 3.15(c)]. A complementary experiment using the PU pulse train [see fig. 3.15(f)] was performed to confirm that the remaining switchable charge corresponds to a polarization P_{-a} = 13.9(6) nC/cm^2, which is about ≈1/3P_a [fig. 3.15(e)].

The effect of the magnetic field intensity and sign on the chiral memory has been explored by cycling the films along the (i-ii-iii) trajectory (marked in fig. 3.10) and measuring the switching current after PUND, ND and PU train pulses, as above. This has been done in order to infer if the magnetic field intensity or sign can modify the partial memory observed in the previous

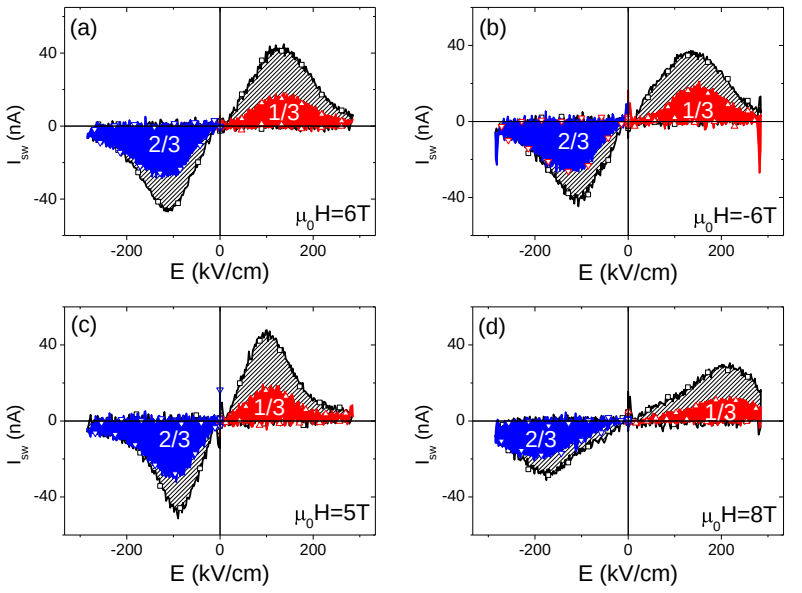

Figure 3.16: *(a) The same data that are plotted in fig. 3.15(b,c). (b, c, d) Switching current obtained by PUND (squares, striped areas), PU (up-triangles) and ND (down-triangles) (solid areas) measurements, after E//a poling process under various magnetic fields, at 5 K.*

experiments (2/3:/1/3). In fig. 3.16 we show $I_{SW}(E)$ curves obtained using -6 T (P_a = 39(2) nC/cm^2, P_{+a} = 24(1) nC/cm^2, and P_{-a} = 15(2) nC/cm^2) [fig. 3.16(b)], 5 T (P_a = 38(1) nC/cm^2, P_{+a} = 25(1) nC/cm^2, P_{-a} = 13(1) nC/cm^2) [fig. 3.16(c)], and 8 T (P_a = 28(1) nC/cm^2, P_{+a} = 18(1) nC/cm^2, P_{-a} = 10(1) nC/cm^2) [fig. 3.16(d)]. As it can be inferred from the obtained values, the relative fractions P_{+a}/P_a and P_{-a}/P_a are roughly constant: $\approx$ 2/3 and $\approx$ 1/3 respectively, and independent of the magnetic field, thus confirming that magnetic field intensity or sign do not favor any particular polarization sign.

A cross-check for the experiment showed in figures 3.14 is the one that we show in figures 3.17, where pyrocurrent is measured. In fig. 3.17(a) it can be seen that, when heating the sample under 6 T after E-poling (positive

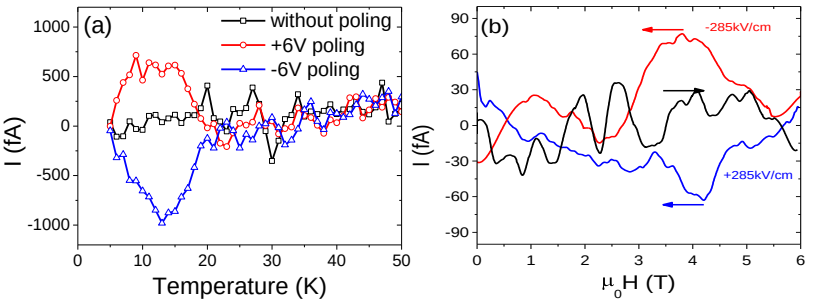

Figure 3.17: *(a) Pyroelectric current measured under 6 T applied along c-axis, after positive, negative and no E-poling applied. Heating and cooling rate 20 K/min. (b) Magnetocurrent at 5 K after ZFC cycling. Field rate 18 mT/s.*

or negative) a current peak occurs; this does not happen if we do not pre-polarize the sample, because domains have both signs of polarization equally populated. Equivalent to this experiment is the following performed with magnetocurrent measurements [fig. 3.17(b)]: after cooling the sample under ZFC conditions the magnetocurrent is measured while increasing the field (labeled with a right-hand arrow), and no current peak is observed indicating that both polar states are equally populated. In the same figure 3.17(b), the current is measured while decreasing the magnetic field (left-hand arrow) after a positive or negative E-poling. Here it is displayed a clear current peak (red and blue curves), this is signature of the selected polar states. Unfortunately, due to the low applicable magnetic field ramp (as maximum as 18 mT/s), the current peak is very small (notice that the current scale is 10 times smaller than in pyrocurrent measurement), comparable to the noise level of our experimental set-up.

Summarizing this first part of the section, data indicate that E-ZFC and H-ZFC processes lead to the formation of domains of $Q_{\pm c}$ with identical probability -and thus total zero polarization in the sample. As shown in the

sketch of fig. 3.18(a) to (b), during the cooling process random nucleation of cycloidal domains with different chiralities occurs. This gives a final state with the same fraction of up and down chiral domains [fig. 3.18(b)] with the subsequent formation of domain-walls (blue dashed lines and red lines).

This is not the case (Figs. 3.15) when a single chirality has been settled and selected by applying an electric field. Data indicate that in this last circumstance, although *ab*-cycloids must have a well-defined chirality (Q_{+c}), when the cycloidal domains are allowed to go back to the *bc*-plane when zeroing the magnetic field, and later on pushed again towards the *ab*-plane by $\mu_0 H = 6$ T, the final chiral configuration clearly keeps memory of the initial E-poled state: the Q_{+c} domains are more abundant than the Q_{-c} ones: $\approx 2/3 Q_{+c}$ and $\approx 1/3 Q_{+c}$ respectively when the sample is poled by $E||a$. By E-poling a single polarization and chiral domain state is formed, a situation which bears much in common with the saturation state of a ferroic system. Results show that, after subsequent magnetic-field induced flop, cycloidal domains of opposite chirality are not randomly formed. Instead of this a fraction of them flop a preferentially to a particular direction, thus suggesting that E-poling, at the same time that induces one single chiral domain, locks the previously different chiral domains [fig. 3.18(c)]. In other words, after E-poling a collective motion of chiral (Q_{+c}) domains is clearly favored during the flopping. This also suggests that during the flopping the formation of $DW_{\pm a}$ is avoided or limited, thus the formation of $DW_{\pm a}$ has some energy cost. This ideal 1:1 memory process is sketched in figure 3.18(c) to (d).

Finally, a plausible scenario to describe the observed partial memory effect can be as follows. First, E-poling induces a single ferroelectric domain state and, consequently, all antiferromagnetic cycloidal domains should have the same chirality, and they are locked. From the previous paragraphs description of the results, coherent flopping of all cycloidal regions from *bc*- to *ab*-planes (or vice versa) would occur without formation of any $DW_{\pm a}$. The eventual incoherent flopping will imply the formation of $DW_{\pm a}$ (or $DW_{\pm c}$, when the

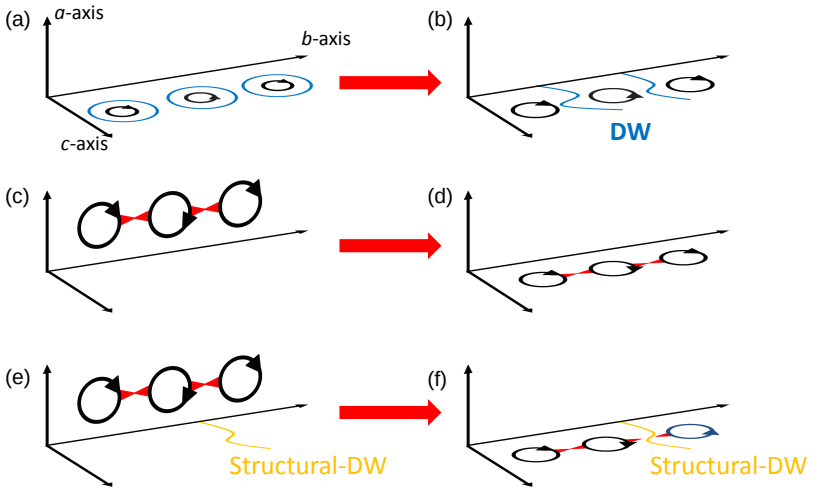

Figure 3.18: *Sketches of (a,b) Nucleation process of different chiral domains in H- and E- ZFC experiment. (c,d) Flopping process of chiral domain after they have been locked by the E-poling field, in an ideal E-poling experiment. (e,f) Flopping process of chiral domain after they have been locked by the E-poling field in the presence of structural defects, which can break the collective motion of the chiral domain. The result would be similar to that found in our E-poling experiment.*

magnetic field is increased again) at the expense of some magnetic and electrostatic energy. Naturally, this argument is not valid if the formation of DW at particular regions of the sample is less energy costly. This is likely to be the case at the unavoidable grain boundaries existing in the sample, which should allow the formation of some $DW_{\pm a}$ [figs.3.18(e) to (f)]. The abundance and microstructure of these boundaries will thus determine the ability of the sample to keep full record of its chiral state during flopping process; in our films, this result is that about 2/3 of the sample flops coherently.

However, it remains still unexplained why chiral domains choose the same chiral direction than the one determined by the previous E-poling sign when they flop back to *bc*-plane. As reported in ref. [139] for $TbMnO_3$ the direction of the polarization can be determined by the tilting of the magnetic

field that induces the flop. Note that in $TbMnO_3$ the flop is produced while magnetic field is applied along b-axis. Thus, the tilting of the applied magnetic field during the flop favors the presence of DW_{+a+c} or DW_{+a-c} (or their complementary DW_{-a-c} or DW_{-a+c}, respectively). This is because the domain walls contain some magnetic moment in the ac-plane, so suitable tilting of the magnetic field in the ac-plane can select the formation of one of them. Now we shift to the measurements in our o-$YMnO_3$ films, which is a different case. As far as we apply the magnetic field along the c-axis, the tilting is always $\approx$0 respect to the c-axis, because $H_c >> H_a$. This results in equal energy cost of the formation of DW_{+a+c} or DW_{+a-c}. This has been in fact demonstrated with repeated experiments after mounting/demounting the sample with accuracy not better than $\pm 5^o$ on positioning, that produce almost identical polarization fractions. Therefore, we conclude that the tilting angle can not play an important role in our experiment, making intrinsic of the system the favoring of DW_{+a+c} or DW_{-a-c} during the flop process.

As a last step in the present analysis of switching chiral domains, data in fig. 3.19(a) reveal that the coercive field (E_c), defined as the maximum of the switching current, increases with the magnetic field. The increase of E_c with H indicates that once the ab-cycloids are formed, switching of their chirality from Q_{+c} to Q_{-c} (or vice versa) by either P (positive) or N (negative) electric pulses becomes gradually more difficult. Note that here chirality is rotating by 180^o, and not by 90^o as we are able to do with the application of a magnetic field. At first sight the increase of E_c with magnetic field appears to be in contradiction with the suggestion of Abe et al. [144] of higher mobility of multiferroic DW under higher magnetic field. However, a simple model can explain this effect: ab-cycloids are formed by $H||c$ with chiralities Q_{+c} to Q_{-c} which are degenerated in energy. Switching from Q_{+c} to Q_{-c} implies a rotation of the chiral vector by $\theta_Q = 180^o$, where θ_Q is the angle defined in the plane perpendicular to the cycloid propagation vector [inset of fig. 3.19(b)], and this implies crossing $\theta_Q = \pm 90^o$ which correspond to $Q_{\pm a}$ (bc-cycloids)

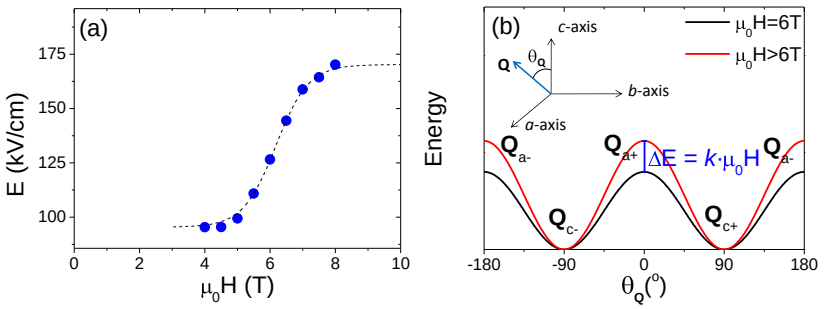

Figure 3.19: *(a) Coercive field extracted from current switching peak of PUND measurements under different magnetic fields. Dashed line is a guide for the eye. (b) Representation of energy dependence on θ_Q depending on the intensity of magnetic field.*

[fig. 3.19(b)] [145]. As shown by experiments [119, 146] and current theories [34, 117], *bc*-cycloids are not stable under H$||c$ thus implying the existence of an energy barrier for Q_{+c} to Q_{-c} switching that increases with the magnetic field. Therefore, the measured increase of E_c with H is not related to lower mobility of cycloidal domains, since it is due to the higher energy cost of rotating chiral domains at higher fields, being in agreement with previous results obtained by Abe et al. [144].

To sum up and in order to simplify the explanation of the performed experiments and the results obtained in the present and the previous section, we can conclude that we have achieved the control of ferroelectric polarization by magnetic field in thin film form. We have seen that after cooling the sample under zero electric and magnetic field, the flop process induced by the application of a magnetic field produces the occurrence of the formation of up and down ferroelectric domains (= chiral domains) with the same population, depicted by a blue line in figure 3.20. We have also seen that, after saturating the ferroelectric state of the sample by application of an electric field, this is partially preserved (= remanence) after successive flopping. The "saturation polarization" curve is depicted in figure 3.20 by the red line, whereas the

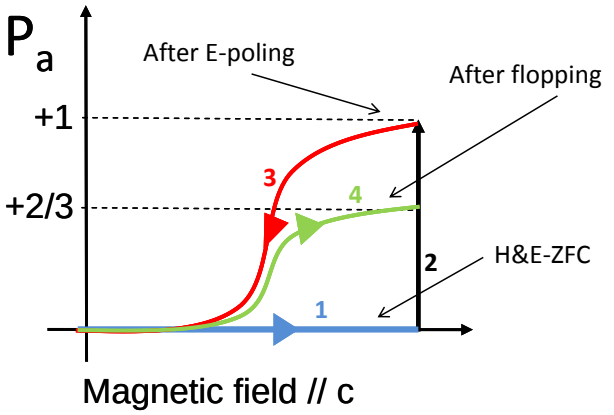

Figure 3.20: *Summary of the performed experiment. Sketch of the polarization dependence on magnetic field, displaying that polarization can be switched in a reversible way. Blue line shows that polarization is zero after electric and magnetic zero field cool process. Red and green line show that previously determined polarization is partially retained after flopping process.*

"remanence polarization" curve is depicted by the green line.

3.4 Strain effects on magnetoelectric coupling and ferroelectricity: magnetoelectric $REMnO_3$ phase diagram

As shown in section 3.2, cycloidal magnetic occurs in the characterized o-$YMnO_3$ thin films. This non-collinear magnetic order differs from the collinear one (E-type antiferromagnet) displayed by its bulk counterpart [61, 123, 147]. This suggests that this unexpected non-collinear magnetic order is determined by the residual strain induced by the substrate.

The aim of the present section is to discern the effects of epitaxial strain on ferroelectricity and magnetoelectric coupling. The results will be analyzed in terms of structural parameters and in the framework of the $REMnO_3$ magnetoelectric phase diagram, demonstrating that, similar to what happens

in bulk material, in our thin films the structure (specifically the a/b ratio) determines the magnetic state.

To that purpose the two sets of films of table 3.1 have been used. We recall here the two main features of these films: i) a/b ratio increases with thickness, and ii) magnetization decreases with thickness.

The ferroelectric character of the thicker films has been already demonstrated (fig. 3.6-3.8). The raw data of PUND measurements for these two thick samples are displayed in figures 3.21(a) and (d). The ferroelectric current peak signature of ferroelectricity during P and N pulses can be clearly observed. The PUND measurements for the thinner samples are shown in figures 3.21(b,c) and (c,f), for a- and c-oriented films, respectively. Although the ferroelectric current peak is not well-visible, clear differences between P(N) and U(D) pulses exist. These differences denote the presence of switchable charge that we ascribe to ferroelectric-switching. Possible reasons for the absence of a clear ferroelectric current peak are: i) the presence of leakage at high electric fields that can hide the peak, and/or ii) the fact that the samples are not saturated, because of the impossibility of applying higher electric fields due to the low breakdown field of these thinner films. In any case, no reliable value for P_r can be extracted. This implies that we can not correlate polarization with strain.

The ferroelectric character of the samples can also be analyzed by measuring ϵ-E loops. As it can be seen in fig. 3.22, all the loops are hysteretic, in spite of not being saturated. Note also the remarkably quite low dielectric losses at low electric fields that the characterized films display. The displayed butterfly-shaped loops confirm the ferroelectric character of all the films, including the thinner ones. However, the fact that for those the loops are not saturated does not allow again to compare polarization values for the different films

Now we will focus on the evolution of the magnetoelectric coupling for the different samples. In figures 3.23, it can be observed that irrespective

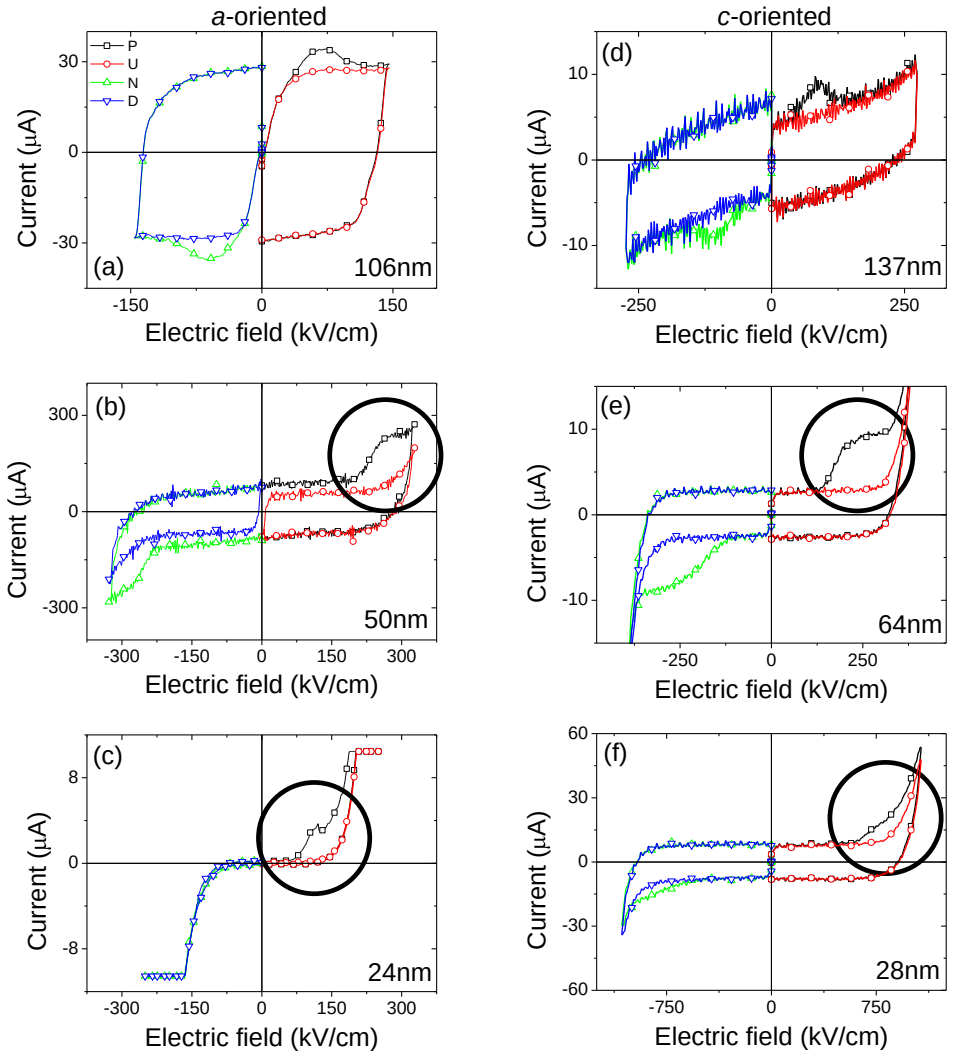

Figure 3.21: *Current vs. voltage loops measured at 5K for a-oriented samples at 10 kHz under a magnetic field (6 T//b), (a, b, c), and for c-oriented samples at 1 kHz (d, e, f) (H=0). Circles signals the difference between the current measured during the P and U pulses, signature of ferroelectricity.*

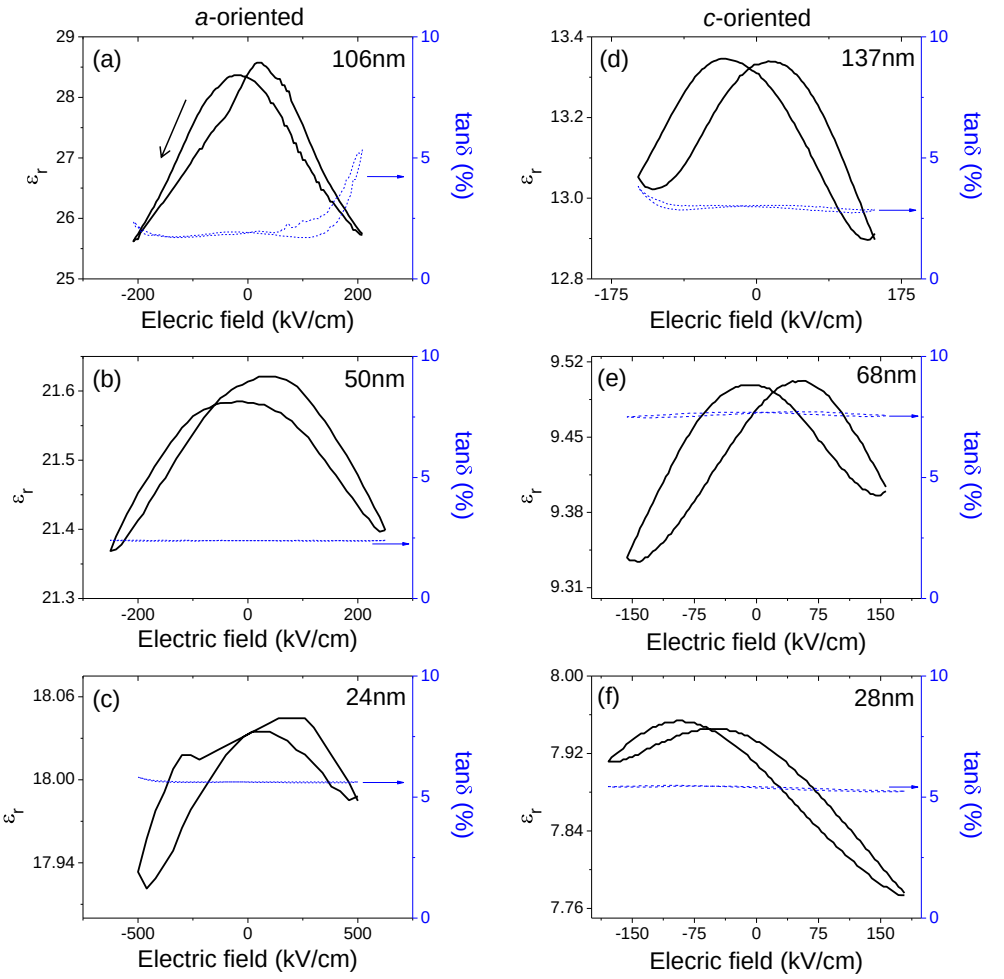

Figure 3.22: *ϵ-E loops at 100 kHz with 300 mV of excitation voltage for a- and c-oriented samples at 5 K. Notice the different left-axis scales.*

of the thickness all samples display the same features as those observed in the thicker ones (already described in section 3.2, fig. 3.11). These were: i) the anisotropy of the ϵ-H loop while applying the magnetic field along the different crystallographic directions, and ii) the occurrence of the dielectric peak that corresponds to the flopping in the a-oriented samples (except for the thinner film in which a kink in the curve can be ascribed to the flop). What is dissimilar between the different samples is the progressive decreasing of the magnetodielectric effect with the thickness (notice the change in the y-scale of figures 3.23 as decreasing the thickness) suggesting that magnetoelectric coupling increases with thickness.

In fig. 3.24 the dependence of dielectric permittivity on temperature is shown. It is seen that the height of the dielectric peak decreases with thickness. As we mentioned above, this dielectric peak is related to the ferroelectricity that emerges at low temperature. As ferroelectricity is consequence of the magnetic order, we can conclude from this figure that as the thickness increases magnetoelectric coupling also increases.

In order to compare the different samples we have compared the amplitude of the dielectric peak, named ME, with a/b ratio and the remanent magnetization (M) at 25K (from table 3.1). This result is plotted in fig. 3.25, where we can see that as the a/b ratio increases, the ME decreases and the M increases. Summarizing, a decrease of magnetoelectric coupling accompanied by an increase of ferromagnetism is observed as a/b ratio increases, while ferroelectricity is preserved.

From the previous results two messages are clear:

- Figure 3.25 shows that there exists a certain a/b ratio window where both ferromagnetic and electric order are present, with coupling between them. In other words, taking non-ferroelectric and antiferromagnetic o-$YMnO_3$ in bulk form as an starting-point, we can induce and modify ferroelectricity and ferromagnetism with coupling between them by

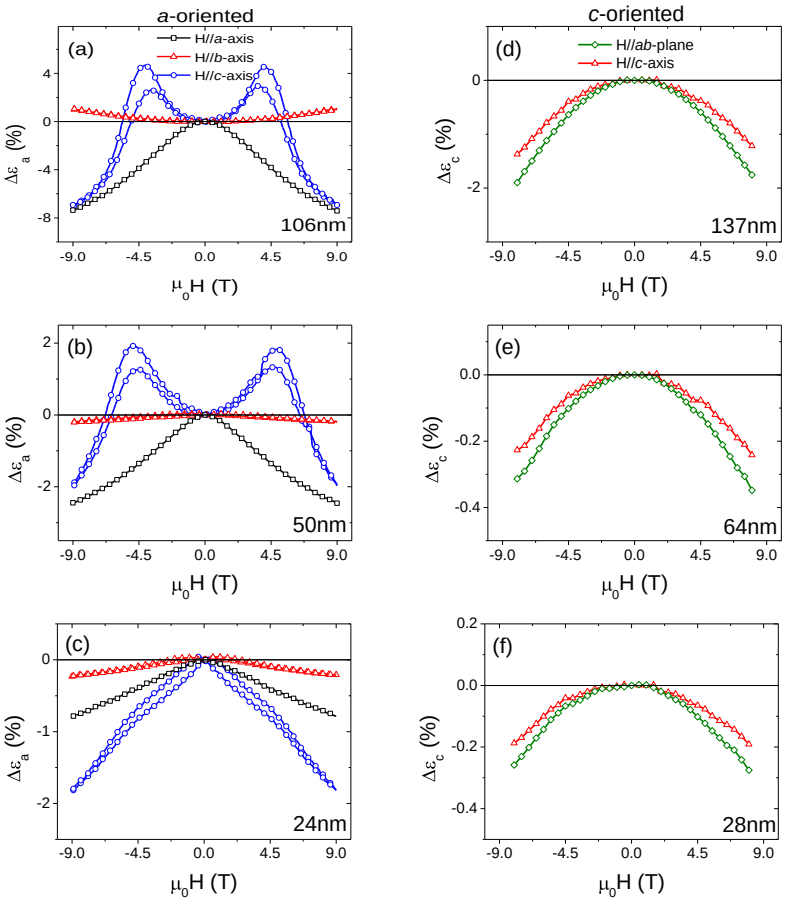

Figure 3.23: *ϵ versus magnetic field loops for a- and c-oriented samples. At 100 kHz with 300 mV of excitation voltage and at 5 K. Notice the different left-axis scales.*

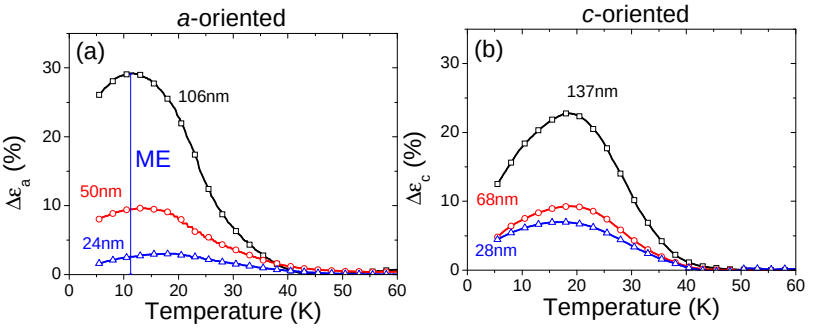

Figure 3.24: *ϵ versus temperature for a- (a) and c-oriented (b) samples. At 100 kHz with 300 mV of excitation voltage.*

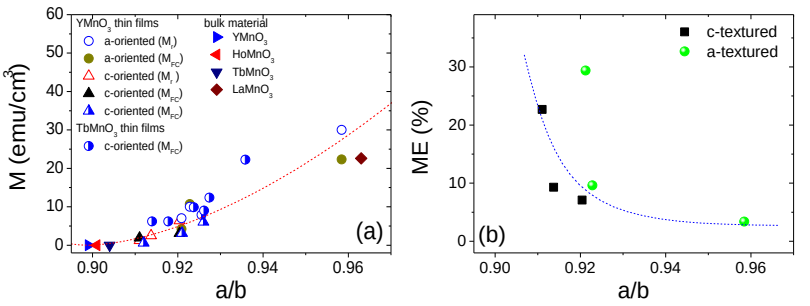

Figure 3.25: *(a)Remanent magnetization measured at 5 K (M_r) (open symbols, extracted from figure 3.5) and magnetization (M_{FC}) after field cool process (solid symbol, extracted from field cool process under 50 mT at 25 K [136]). Samples not used in the present work are also shown, c-textured o-$YMnO_3$ [63], and $TbMnO_3$ [148] films, for completeness. For bulk materials a/b ratio has been extracted from [104], M for all of them has been fixed 0 because they are E-type or cycloidal antiferromagnets with zero net magnetic moment, except for $LaMnO_3$, which is a canted A-type antiferromagnet [149]. (b) Increment of dielectric permittivity respect its value at 60 K ($\Delta\epsilon$) for a- and c-oriented samples.*

strain engineering.

- Second, ferroelectric and magnetodielectric data show the typical signs of cycloidal magnetic order for all the films, thus polarization along c-axis when H=0 and along the a-axis when high enough magnetic field is applied along c-axis. However, the decrease of magnetoelectric coupling as the thickness of the film is reduced and strain increased suggests that the contribution of the cycloidal magnetic order is smaller for thinner films.

These results can be well described in terms of the magnetoelectric phase diagram of $REMnO_3$ (fig. 3.26). Results of section 3.2 have shown that our thicker and most relaxed films display the cycloidal magnetic order. In the present section a decrease of magnetoelectric coupling has been correlated with the increase of a/b ratio, while ferromagnetism increases. On one hand, the decrease of magnetoelectric coupling can be taken as a signature of that cycloidal order is gradually suppressed with a/b ratio. On the other hand, the increase of ferromagnetism with a/b ratio can be signature of that canted magnetic order is being favored, as suggested in [62]. In the magnetoelectric phase diagram of $REMnO_3$ (fig. 3.26), this can mean that increasing a/b favors E-type or A-type magnetic phases. However, by symmetry reasons, canting is not allowed in E-type antiferromagnetic structures [150], thus only canted A-type antiferromagnetic order can be favored. Therefore, the epitaxial induced strain, which induces an increase of a/b ratio, mimics the effect of changing the RE by another with bigger ionic radii. This result is coherent since a/b ratio is proportional to the RE ionic radii, in bulk compounds [104, 151].

This conclusion is also consistent with the results reported on the literature of o-$YMnO_3$ single-crystals. o-$YMnO_3$ single crystals show an a/b ratio of about 0.8997 and E-type magnetic ordering. Our most relaxed films shows smaller a/b ratio and cycloidal magnetic ordering. Thus indicating that

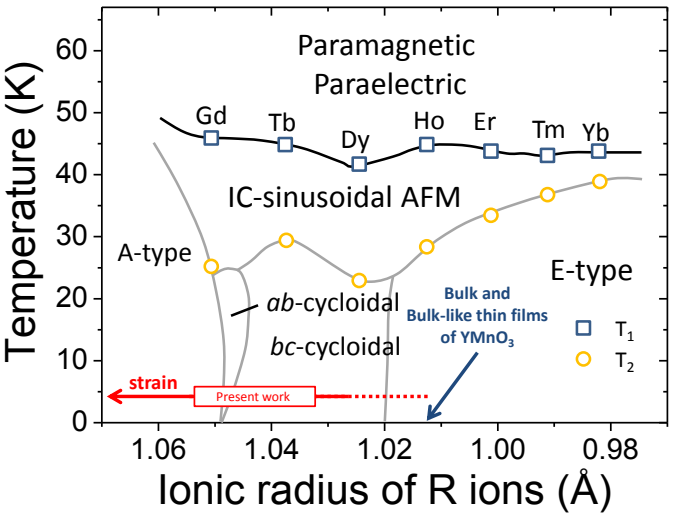

Figure 3.26: *Phase diagrams of orthorhombic $REMnO_3$ with magnetic RE=Gd, Tb, Dy, Ho, Er, Tm, and Yb adapted from refs. [116, 120]. Results for o-$YMnO_3$ in bulk [61] and in bulk-like thin films [147] are also displayed. Our films would be placed, according to our results, across the red solid line.*

E-type phase correspond to a lower a/b ratio (single-crystal) than the one displayed by our films, which correspond to cycloidal order. In the phase diagram displayed in figure 3.26, $YMnO_3$ single-crystals corresponds to ionic radius around 1.01 Å(signaled with Bulk o-$YMnO_3$ label), on the right-side of our films (signaled with a red arrow).

The analyzed results are also consistent with the films grown on a different substrate [(010)-$YAlO_3$] reported by Nakamura et al. in ref. [147] showing features of E-type magnetic order. In fact these films show a b-axis value more similar to bulk than to the b-axis value of our films, pointing that actually they are more relaxed. Due to the lack of structural data in ref. [147], we can not state that this is also valid for the a/b ratio.

It has been reported in ref. [116] that o-$YMnO_3$ lies on the very verge line

between E-type and cycloidal magnetic order, giving sense at the fact that a low distortion of the lattice structure can give rise to the stabilization of cycloidal order (found in our films). These results are illustrated in fig. 3.26.

Angles and distances between Mn and O (all located in the *ab*-plane) are known to be crucial in order to determine the magnetic structure. Our structural characterization does not allow to determine the Mn-O bond angle, but our results point to that a/b ratio can be taken as the key parameter that determines the magnetic order in the studied o-$YMnO_3$ films.

Finally, if we make the lens bigger and we include the results in hexagonal $YMnO_3$ thin films [135], which is the most stable phase in bulk; the here reported data suggest that the whole magnetoelectric phase diagram of $REMnO_3$ can be reproduced by strain engineering using only o-$YMnO_3$. This can be done from hexagonal to orthorhombic phase and inside the orthorhombic phase, magnetic order can be tailored from E-type [147], to canted A-type (thinner films here reported), crossing the cycloidal region (thicker films here reported).

3.5 Conclusions

We have shown that epitaxial o-$YMnO_3$ thin films are ferroelectric and display magnetoelectric coupling. Magnetoelectric coupling allows to control the direction of polarization vector ($\approx$80 nC/cm^2) in *a*-oriented films by applying a magnetic field along *c*-axis: then polarization vector flops from *c*- to *a*-axis, and this is a signature of cycloidal order with the cycloid contained in the *bc*-plane. This magnetic ordering in o-$YMnO_3$ thin films is consistent with the measurement of net polarization along the *c*-axis ($\approx$90 nC/cm^2) in the *c*-oriented film, without the application of any magnetic field. A detailed analysis of the behavior of the polarization under magnetic field has shown that polarization partially retains its direction after flopping, indicating that there is preferential coherent flopping of the different domains. This partial

memory effect has been ascribed to the formation of new domain walls at structural defects.

Moreover, we have also shown that epitaxial strain can be used to modify ferroelectric and magnetoelectric properties, inducing the formation of cycloidal or canted A-type magnetic order. Therefore, by using epitaxial strain we have partially reproduced the magnetoelectric phase diagram of $REMnO_3$ without chemical substitution.

Chapter 4

$CoFe_2O_4$ and $BaTiO_3$ horizontal heterostructures

Horizontal multiferroic composites are those resulting from the combination of alternating ferroelectric and ferromagnetic layers (multiferroic multilayer). These materials in thin film form have attracted much attention [36–43], because they show ferroelectric and ferromagnetic properties similar to those found in single films. In bilayered heterostructures relevant results in the control of the magnetization by electric field have been reported [45, 47, 49, 51, 53, 152–158] using ferromagnetic materials such as Fe, NiFe, $La_{1-x}Sr_xMnO_3$, and others, and ferroelectric materials such as $Pb(Zr_{1-x}Ti_x)O_3$ or $BaTiO_3$. However, fewer works can be found on the measurements of the inverse effect, that is the control of electric order by magnetic field [64, 159–165].

In the present chapter, we use bilayer systems, where both functional layers (ferromagnetic and ferroelectric) are thin films and the substrate is only used as a support for the whole structure, disregarding systems where the substrate plays a role as a functional part of the heterostructure. These systems, when compared with those where the substrate is a functional part of the device, present the advantage of being cheaper, because ferroelectric ($Pb(Zr_{1-x}Ti_x)O_3$) or magnetic ($La_{1-x}Sr_xMnO_3$) single-crystal substrates are

more expensive and technologically unappealing compared with other common substrates, such as $SrTiO_3$, or even silicon (Si). Moreover, these multiferroic structures permit the study of magnetoelectric properties depending on the characteristics of the different layers, thickness, stacking order, crystal quality, and others.

Even more, we focus on multilayers where the ferromagnet is insulating. This allows us to ensure that the coupling present on the characterized systems is strain mediated and to disregard charge effects as a coupling mechanism. This is because in a ferromagnetic insulator, in principle, there is not charge screening at the interface and there can not be a change in the charge carrier density as it is the case of ref. [47]. We have chosen the $BaTiO_3$ perovskite and the $CoFe_2O_4$ spinel as ferroelectric and ferromagnetic materials, respectively.

The main characteristics of multilayered multiferroics are: i) good ferroelectric and ferromagnetic properties are limited by the dissimilar crystal structures of commonly used ferromagnetic and the ferroelectric materials, ii) magnetoelectric coupling is limited by the contact area, thus by the number of alternating layers, by the interface quality, and by the clamping effect induced by the substrate. Now we will briefly summarize the state of the art of the study of these mentioned characteristics.

The growth difficulties due to the structural dissimilarities between both materials have their most clear signature in the dependence of the functional properties on the stacking order. For instance, He et al. [52, 65] showed that ferroelectric properties are poorer when the ferroelectric $Pb(Zr_{0.53}Ti_{0.48})O_3$ is grown on top of the ferromagnet $Co_{0.9}Zn_{0.1}Fe_2O_4$, and also that ferromagnetic properties are poorer when the ferromagnet is grown on top. This reveals the intrinsic problems of growing a ferroelectric (ferromagnet) on top of a ferromagnet (ferroelectric).

In spite of these difficulties, multilayer films with different composition [52, 65, 166–170] have been reported to display multiferroic properties not so far from those found in a single-layer. However, in the literature there is

a lack of information on the functional characterization of $BaTiO_3$-$CoFe_2O_4$ bilayered systems. Magnetic [169] and ferroelectric [170] properties have been studied in $BaTiO_3$-$CoFe_2O_4$ structures. In ref. [170], good ferroelectric properties have been measured, but ferroelectricity is significantly suppressed for thicknesses below 60 nm. An interesting study can be found in ref. [168]; however, in this case, multilayered systems were grown as nanocolumns (0-0 multilayered nanodot arrays), a very different system compared to the one focused in the present chapter. At present, the reported data do not clearly conclude about the technological applicability of this composition, and there is a lack of information about the strain effects on ferroelectric properties of the bilayered system.

Magnetoelectric coupling in multiferroic multilayers also depends on the interface quality [154]. It has been shown that in films grown by pulsed laser deposition, where ferromagnetic and ferrroelectric are perovskite compounds, the interfaces are commonly sharp with low composition intermixing [167, 171], which, in principle, may favor larger magnetoelectric coupling. However, to date, bilayers with either spinel on perovskite or perovskite on spinel are repeatedly observed to grow three-dimensionally with rough morphology (see for instance ref. [170, 172–175], which should not come out in favor of the good interface quality.

The coupling between ferroelectricity and ferromagnetism can also be limited by the clamping effect of the substrate. Indeed comparing bilayered systems of $Pb(Zr_{0.52}Ti_{0.48})O_3$ and $La_{0.7}Sr_{0.3}MnO_3$, grown as thin films by pulsed laser deposition a smaller value of magnetoelectric coefficient [3.0 mV $cm^{-1}Oe^{-1}$, ref. [165]] is measured compared to that found for thick-film bilayers prepared by tape-casting techniques [30 mV $cm^{-1}Oe^{-1}$, ref. [164]]. This decrease in the magnetoelectric coupling is associated to substrate clamping, which locks piezoelectric/magnetostrictive effects of the ferroelectric/ferromagnetic material reducing significantly the coupling. Petrov et al. [176] predicted that to significantly reduce this effect the substrate

thickness should be at most twice the ferroelectric thickness (in the case of $Ni_{1-x}Zn_xFe_2O_4 - Pb_{1-x}Zr_xTiO_3$ composite), which is experimentally very difficult. Recent works suggested that the growth of nanostructured multilayered systems (with high aspect ratio) would reduce the clamping effect because of the much larger aspect ratio over conventional multilayer thin films [168]. However, it is worth mentioning that clamping effects have not yet been experimentally analyzed in detail in films.

Summarizing, there are some open questions on the fundamental knowledge of the multiferroic and magnetoelectric properties of the multiferroic multilayered films. In this chapter, we address the study to the ferroelectric properties and magnetoelectric coupling dependence on stacking order in $BaTiO_3$-$CoFe_2O_4$ systems (section 4.2). From this study, we get insights into the substrate clamping effect, and the possibility to obtain bilayered structures with bulk-like ferroelectric properties. A more detailed study of ferroelectric properties dependence on stacking order and ferroelectric thickness is also presented (section 4.3). With the aim of performing the mentioned studies a set of samples grown by pulsed laser deposition have been used and they are described below.

4.1 Samples

Bilayers with different stacking order and $BaTiO_3$ and $CoFe_2O_4$ respective thicknesses were grown on different bottom electrodes, as summarized in table 4.1. Metallic epitaxial $La_{2/3}Sr_{1/3}MnO_3$ or $SrRuO_3$ (ferromagnetic and paramagnetic at room temperature, respectively) have been used as bottom electrodes. The entire heterostructure was grown by pulsed laser deposition in one process. Growth conditions are those optimized for the growth of the two materials separately with flat surfaces and single textured: $CoFe_2O_4$ has been grown at 500^{o}C with 0.1 mbar of oxygen pressure, and a pulse laser frequency of 5 Hz, and $BaTiO_3$ at 700^{o}C, 0.02 mbar, and 5 Hz. Extensive

Table 4.1: *List of studied samples. The used bottom electrode is indicated (LSMO corresponds to $La_{2/3}Sr_{1/3}MnO_3$, and SRO to $SrRuO_3$) and their respective thicknesses are constant for all the samples, $t_{LSMO} \approx 20$ nm and $t_{SRO} \approx 60$ nm. $BaTiO_3$ (BTO) c/a parameter is also indicated. c/a* parameter corresponds to the c/a ratio of a second $BaTiO_3$ phase (more strained) found in some bottom $BaTiO_3$ samples.*

Stacking sequence	Label	Electrode	t_{BTO} (nm)	t_{CFO} (nm)	c/a	c/a*
Bottom $BaTiO_3$	**SB25C100**	SRO	25	100	1.06	1.10
	SB80C15	SRO	80	15	1.05	
	LB25C100	LSMO	25	100		1.10
	LB50C50	LSMO	50	50		1.10
	LB72C6	LSMO	72	6	1.04	1.09
Top $BaTiO_3$	**SC100B25**	SRO	25	100	0.98	
	SC15B80	SRO	80	15	1.00	
	LC100B25	LSMO	25	100	0.99	
	LC50B50	LSMO	50	50	1.00	
	LC6B85	LSMO	85	6	1.00	

details on growth and structural properties can be found in the Ph.D. thesis of N. Dix [70].

From the structural point of view, we divide the samples in two groups: those with $BaTiO_3$ on the bottom (named bottom-BTO samples, fig. 4.1(a)) and those with $BaTiO_3$ on the top (named top-BTO samples, fig. 4.1(b)).

In bottom-BTO samples, $BaTiO_3$ is *c*-textured, as inferred from the X-ray analysis. Q-plots and $\theta - 2\theta$ data [177] reveal that, in some layers, two families of $BaTiO_3$ crystallites exist. These two phases have different lattice parameters that correspond to two different strain states of $BaTiO_3$ [178]. As a general trend for all the samples, one of the phases corresponds to a more strained $BaTiO_3$, with large c/a ratio (consequence of the biaxial compressive strain induced by the substrate) yielding to a more tetragonal $BaTiO_3$ (c/a*

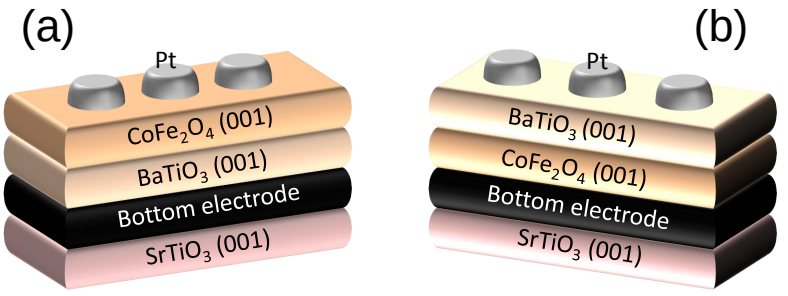

Figure 4.1: *Sketches of $BaTiO_3$-$CoFe_2O_4$ bilayers with two different stacking sequence: (a) Bottom-BTO and (b) Top-BTO.*

$\approx$ 1.10); the other phase corresponds to a less strained $BaTiO_3$ (c/a $\approx$ 1.05). Note that the less strained $BaTiO_3$ still displays a c/a ratio larger than bulk [$(c/a)_{bulk}$ = 1.01]. The thinner films grown on $La_{2/3}Sr_{1/3}MnO_3$ only show the most strained c/a* phase, and as the thickness is increased the second c/a phase starts to appear (see table 4.1). The presence of these two phases suggests that there is an step-like strain gradient in the samples, i.e. $BaTiO_3$ partially relaxes at a certain distance from the substrate. The fact that the two $BaTiO_3$ phases with different strain are present for the very thin sample grown on $SrRuO_3$ suggests that the strain relaxation occurs at lower thickness when using this electrode. Indeed, in SB80C15 sample, only the less strained phase is present.

In bottom-BTO samples, $CoFe_2O_4$ grows relaxed with cubic lattice parameter identical to that found in bulk (a=8.40 Å, a_{bulk}=8.40 Å).

$\theta - 2\theta$ data for top-BTO samples show that the out-of-plane parameter is larger than *c*-axis of bulk $BaTiO_3$. Q-plots show that c/a ratio is between 0.98 and 1 (table 4.1); in spite of the error in the extraction of in-plane parameters due to the poor angular resolution of Q/plots, this suggests that we have nearly relaxed $BaTiO_3$ in these samples.

In top-BTO samples, the $CoFe_2O_4$ grown on bottom shows near bulk

lattice parameters (a=8.40 Å and c=8.39 Å).

We would like to remark that bottom-BTO films present an unit cell volume (V_{uc}) V_{uc} = 65.4 ± 0.2 Å^3, and top-BTO films have 66.4 ± 0.2 Å^3 (V_{uc} are an average for top and bottom-BTO samples), both larger than bulk values (V_{bulk} = 64.32 Å^3). This has been ascribed to be most probably due to compositional changes and/or oxygen vacancies, which are known to be responsible for $BaTiO_3$ unit cell enlargement.

All samples display similarly flat surfaces with rms ≈ 0.25 nm with terraces for top-BTO samples (absent for the samples with 100 nm of $CoFe_2O_4$ at the bottom) and with homogeneously distributed coalescencing grains with 1-2nm depth holes for bottom-BTO samples. The presence of these flat surfaces for bilayers with both stacking order suggests the two-dimensional growth and, consequently, the presence of good quality $BaTiO_3$-$CoFe_2O_4$ interfaces, but we do not have direct information about this relevant parameter.

Magnetic properties of $CoFe_2O_4$ are similar to those found in $CoFe_2O_4$ films of similar thickness [179], for all the samples. More detailed analysis of magnetic data is found in ref. [70].

4.2 Ferroelectricity and magnetoelectric coupling dependence on stacking order: clamping effects

In this section the dependence of the ferroelectric properties and the magnetoelectric coupling on the stacking sequence are explored. We have used two samples: The first sample (SB25C100, in bold in table 4.1) is a thin layer of $BaTiO_3$ (25 nm) grown on the substrate ($SrRuO_3$/$SrTiO_3$), capped with a thick layer of $CoFe_2O_4$ (100 nm). The second sample (SC100B25, in bold in table 4.1) consists of a thick $CoFe_2O_4$ layer (100 nm) grown on the substrate and a thin $BaTiO_3$ layer (25 nm) grown on top.

The bottom electrode chosen for the present experiments has been $SrRuO_3$,

because it is paramagnetic above $\approx$ 150 K, and thus at studied temperatures it will not mask the magnetic signal of $CoFe_2O_4$.

The ferroelectric behavior of the bilayers is demonstrated by P-E loops at room temperature displayed in figure 4.2. The loops show hysteresis, which is signature of ferroelectricity. This signature is also present in the I-E characteristics [fig. 4.2(b)], where the two ferroelectric current peaks that correspond to the ferroelectric switching are well-visible at fields near 500 kV/cm. Some leakage current (similar for both samples) is present at high electric fields; however, this does not hide the ferroelectric current peaks.

In figure 4.2(a) it can be also observed that P_r and P_s have larger values for bottom-BTO sample than in bulk ($P_{s,bulk}$ = 26 $\mu C/cm^2$, dashed lines in the figure). This is not the case for top-BTO sample, which displays polarization values similar to bulk $BaTiO_3$.

In figure 4.2(c), we show the temperature dependence of permittivity of the bottom-BTO sample. A rapid increase of ϵ with temperature can be observed. However, this is only because of the presence of two electroactive contributions to the dielectric permittivity measurement ($CoFe_2O_4$ and $BaTiO_3$ contributions, as described later in detail), which results in a rapid increase of permittivity and a peak on dielectric losses (as partially observed in fig. 4.2(d) because of the upper experimentally available temperature limit) as described in detail in ref. [76]. However, a detailed inspection of this dependence also reveals the occurrence of two subtle but well-visible kinks at temperatures $T_1 \approx 360$ K and $T_2 \approx 250$ K.

In figure 4.2(e), the temperature dependence of permittivity of the top-BTO sample is shown. Similar to the previous sample the most visible feature is the rapid increase of ϵ with temperature (here the rapid increase of permittivity and the peak of dielectric losses are well-visible in figure 4.2(f)). In this top-BTO sample a clear dielectric peak is visible at $T_2 \approx 280$ K, and a less visible kink at $T_1 \approx 360$ K.

The ferroelectric measurements on bottom-BTO sample suggest that the

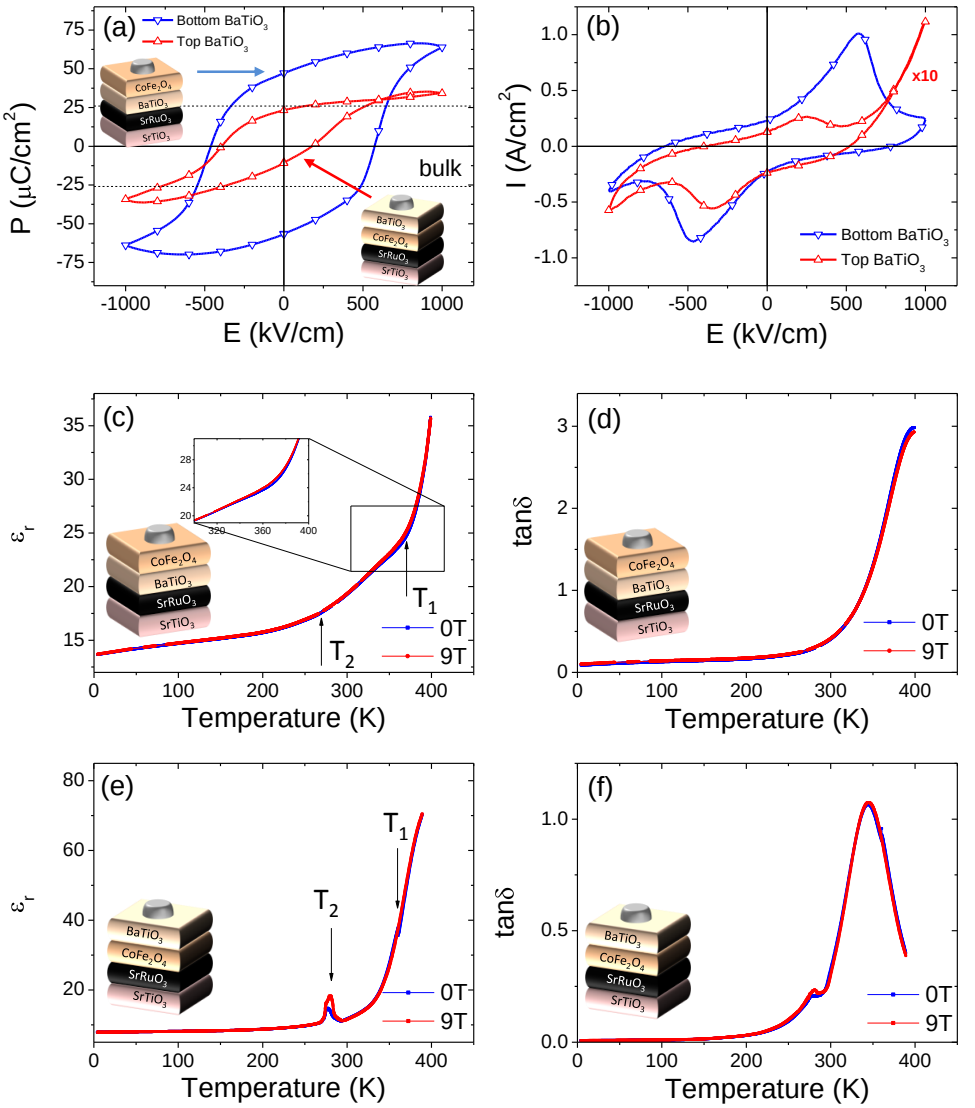

Figure 4.2: *P-E loops (a) integrated from I-E characteristics (b) for SB25C100 and SC100B25 samples, both at room temperature. (c) ϵ and (d) tanδ at 100 kHz versus temperature (while heating the sample) with and without magnetic applied field along the plane of the film for SB25C100. (e,f) Idem for SC100B25. Arrows indicate cubic-tetragonal (T_1 = high temperature) and tetragonal-orthorhombic (T_2 = low temperature) transitions. Leakage in P-E loops has been compensated by DLCC after careful analysis in terms of the procedures described in chapter 2.3.*

enhanced $BaTiO_3$ tetragonality induced by the substrate reflects is reflected in the large measured polarization. In top-BTO sample, the extracted ferroelectric polarization is similar to bulk value, which is coherent with the fact that $BaTiO_3$ on top-BTO sample is more relaxed. The dielectric anomalies found on both samples at T_1 and T_2 most probably correspond to the cubic-tetragonal (T_1) and to the tetragonal-orthorhombic (T_2) transitions (in bulk 393 and 278 K, respectively), which are partially hindered by the mentioned rapid increase of ϵ with temperature in both samples.

Figures 4.2(c-f) display the ϵ and tanδ measured under 9 T magnetic field applied in-plane. Only a very small variation (see inset of fig. 4.2(c)), comparing with the measurement at zero magnetic field, of ϵ at T_1 can be observed for bottom-BTO. In contrast, a well-visible variation of ϵ is observed at T_2 for top-BTO sample [fig. 4.2(e)].

The dependence of the variation of permittivity under the application of an external magnetic field applied in-plane on temperature becomes clearer if $\Delta\epsilon$ ($\Delta\epsilon = \frac{\epsilon(\mu_0 H=9T)-\epsilon(\mu_0 H=0T)}{\epsilon(\mu_0 H=0T)}$) is plotted, fig.4.3(a,b).

In bottom-BTO sample [fig. 4.3(a)], $\Delta\epsilon$ shows a well visible variation ($\approx$ 2%) at T_1' $\approx$ 361 K, and two small but well-defined peaks at lower temperatures, T_2' $\approx$ 244 K and T_3' $\approx$ 161 K. Most probably, these three peaks correspond to the three structural phase transitions of $BaTiO_3$ (in bulk $BaTiO_3$: T_1 = 393 K, where cubic $BaTiO_3$ becomes tetragonal, T_2 = 278 K, from tetragonal to orthorhombic, and T_3 = 183 K, from orthorhombic to romboedric), as depicted in figure 4.3(a).

Similarly, top-BTO sample [fig. 4.3(b)] shows three magnetodielectric anomalies at T_1' $\approx$ 360 K, T_2' $\approx$ 281 K, and T_3' $\approx$ 178 K. Note that the variation of the dielectric permittivity at T_2' is larger than at T_1'; however, we ascribe this to the fact that here the relative variation of dielectric permittivity is smaller because at this temperature ϵ is very large compared with its value at T_2'.

Comparing both samples we observe that the magnetodielectric response

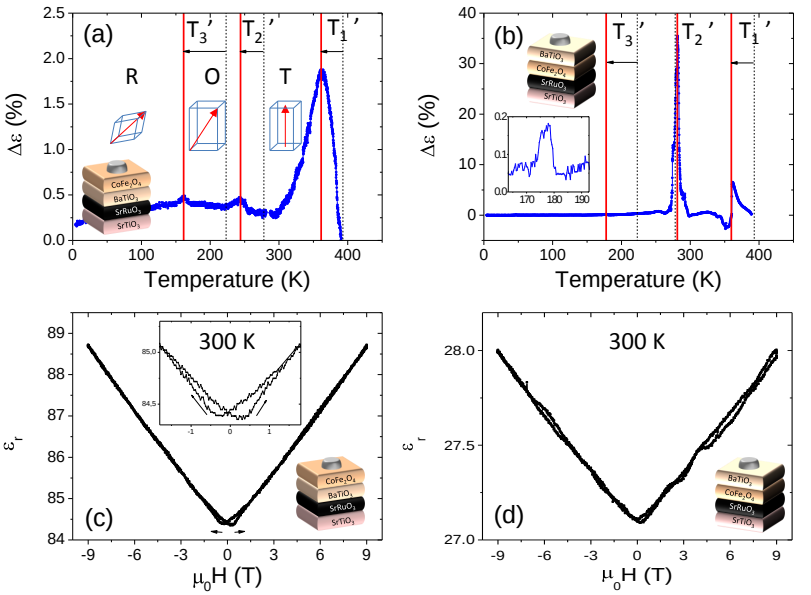

Figure 4.3: *Magnetodielectric response ($\Delta\epsilon$) under 9 T magnetic field applied along c-axis for SB25C100 (a) and SC100B25 (b) samples. Dashed lines indicate the cubic-tetragonal (T_1'), tetragonal-orthorhombic (T_2') and orthorhombic-romboedric (T_3') phase transitions for bulk-$BaTiO_3$, and solid lines the corresponding transitions measured in the film. Plotted results have been extracted from the data displayed in figures 4.2(c,e). ϵ-$\mu_0 H$ loops at 10 kHz and room temperature for $\mu_0 H$ applied along the in-plane for SB25C100 (c) and SC100B25 (d) samples. Note the different measurement frequency compared with the measurements displayed in figure 4.2.*

under 9 T at the transition temperatures (T_1, T_2, and T_3) is much larger for top-BTO sample (compare the change in the y-scale of figures 4.3(a,b)). Note that for top-BTO sample the maximum change is around 36 %, and for bottom-BTO only 2 %.

The observed magnetodielectric anomalies near the $BaTiO_3$ structural transition temperatures can be ascribed to be because of the strain mediated magnetoelectric coupling between $BaTiO_3$ and $CoFe_2O_4$. The measured variations of dielectric permittivity are large (for top-BTO sample up to $\chi_E = 4$ %/T, as defined in chapter 2) compared with the magnetodielectric measurements performed in other similar systems, χ_E = -0.3 %/T in $Pb(Zr_{0.4}Ti_{0.6})O_3$-$Ni_{0.8}Zn_{0.2}Fe_2O_4$ multilayer [159] and χ_E = -0.3 %/T in $BiFeO_3/CoFe_2O_4$ bilayers [162]. Note that in the referred works the measurement is performed at room temperature.

Now we turn to the magnitude of the measured magnetodielectric effect depending on the stacking order. As we have observed, bottom-BTO sample shows less variation of dielectric permittivity under the application of external magnetic field at transition temperatures compared with top-BTO sample. This observation indicates that for bottom-BTO sample, $BaTiO_3$ is highly clamped to the substrate. Consequently, it can not react to magnetostrictive response of $CoFe_2O_4$ under magnetic field. In contrast in top-BTO sample, $BaTiO_3$ is now clamped to the $CoFe_2O_4$ layer, and thus the magnetodielectric effect is large. Moreover, in top-BTO sample the larger thickness of $CoFe_2O_4$ can somehow release the clamping effect of the substrate on $CoFe_2O_4$.

The sign of the measured magnetodielectric effect (permittivity increases near transition temperatures under the application of magnetic field) seems to be in agreement with the fact that $CoFe_2O_4$'s magnetostrictive coefficient is negative [69]. Therefore, when applying the magnetic field in plane, $CoFe_2O_4$ should be compressed along the magnetic field direction and, subsequently, it induces an extra compressive strain to $BaTiO_3$. This should result in an increase of polarization and the observed increase of dielectric permittivity

near the $BaTiO_3$ transition temperatures.

As inferred from figures 4.3(a,b), we can observe that T_1, T_2, and T_3 transition temperatures take place at lower temperatures that for bulk-$BaTiO_3$ structural transitions (indicated by dashed lines in figs. 4.3(a,b)). The theoretical approach performed by Pertsev et al. [180] suggests that when $BaTiO_3$ suffers a compressive epitaxial strain on the order of 2 % (as it is the case of bottom-BTO sample), tetragonal phase should be more stable, and thus Curie temperature should increase, and only one other transition at low temperature is expected. This prediction does not agree with the results shown in figure 4.3(a), where ferroelectric Curie temperature is observed at temperatures below bulk, and the other two structural transitions appear. However, Ti and oxygen vacancies can be at the origin of the observed decrease of transition temperatures. It has been seen that doped films [181], or oxygen deficient $BaTiO_3$ [182] have lower transition temperatures than pure and stoichiometric $BaTiO_3$. The fact that in our films V_{uc} of $BaTiO_3$ is larger than in bulk suggests that oxygen vacancies can be the prime reason for the observed effect. This explanation for the transition temperatures decrease would also apply for bottom-BTO sample.

We rule out that the magnetodielectric peak at $\approx$ 161 K is related to the $SrRuO_3$ paramagnetic-ferromagnetic transition, because magnetic data (not shown here) indicate that both transitions (the T_3' and the $SrRuO_3$ magnetic transition) are well-separated.

In figure 4.3(c), the dielectric permittivity dependence on applied magnetic field measured at room temperature for bottom-BTO sample is shown. We can see that the magnetodielectric coefficient is around 0.5 %/T and the hysteresis induced by the ferromagnetic nature of $CoFe_2O_4$ is well visible. The shape of the permittivity dependence on magnetic field and the magnetitude of the magnetoedielectric effect is similar to that observed in $BaTiO_3$-$CoFe_2O_4$ vertical nanocomposites (see chapter 5). For top-BTO sample [figure 4.3(d)] the effect is even smaller (less than 0.5 %/T) at room temperature, even

though it is present. Notice also that the measurement frequency is 10 kHz, which is different from that used in figures 4.2(c,e). This difference on absolute values is due to the presence of the mentioned two electroactive contributions. The origin of this magnetodielectric response far from transition temperatures is discussed in the following.

It is important to distinguish whether the measured magnetodielectric effect at 300 K results from an intrinsic magnetoelectric coupling, or it is caused by the magnetoresistive response of $CoFe_2O_4$ [81]. In order to address this issue we have performed impedance spectra analysis of the sample that displays the largest variation of dielectric permittivity at room temperature: SB25C100. The Nqvist diagram displayed in figure 4.4(a) evidences that two contributions exist, as reflected by the two overlapped semicircles present in the diagram. These two contributions have been fitted to an equivalent circuit of two RCPE elements (a resistance in parallel with a constant phase element), plus the resistance in series with an inductance as expected for the wires and contact contributions (section 2.2.2). This equivalent circuit is sketched in figure 4.4(e); we assume that the highly resistive contribution ($RCPE_1$) can be ascribed to $BaTiO_3$ and the low resistive to $CoFe_2O_4$ ($RCPE_2$) [183, 184]. For each RCPE element, the resistive contribution that corresponds to the parallel resistance, and the real and imaginary part of dielectric permittivity at 100 kHz, which correspond to the parallel constant phase element, have been extracted (as described in section 2.4). The results are plotted in figure 4.4(b-d, f-h). As it can be observed, all the variations of the dielectric permittivity and resistivity (calculated according to the equations displayed in chapter 2) are within the error bar (determined by the error fit) for $BaTiO_3$. This result suggests that magnetostriction of $CoFe_2O_4$ does not induce a change in $BaTiO_3$ dielectric permittivity. In addition, figures 4.4(f-h) show that the variations of the dielectric permittivity are also below the error bar for $CoFe_2O_4$. This is not the case of the resistivity ascribed to $CoFe_2O_4$, which significantly changes under the application of a magnetic field. These

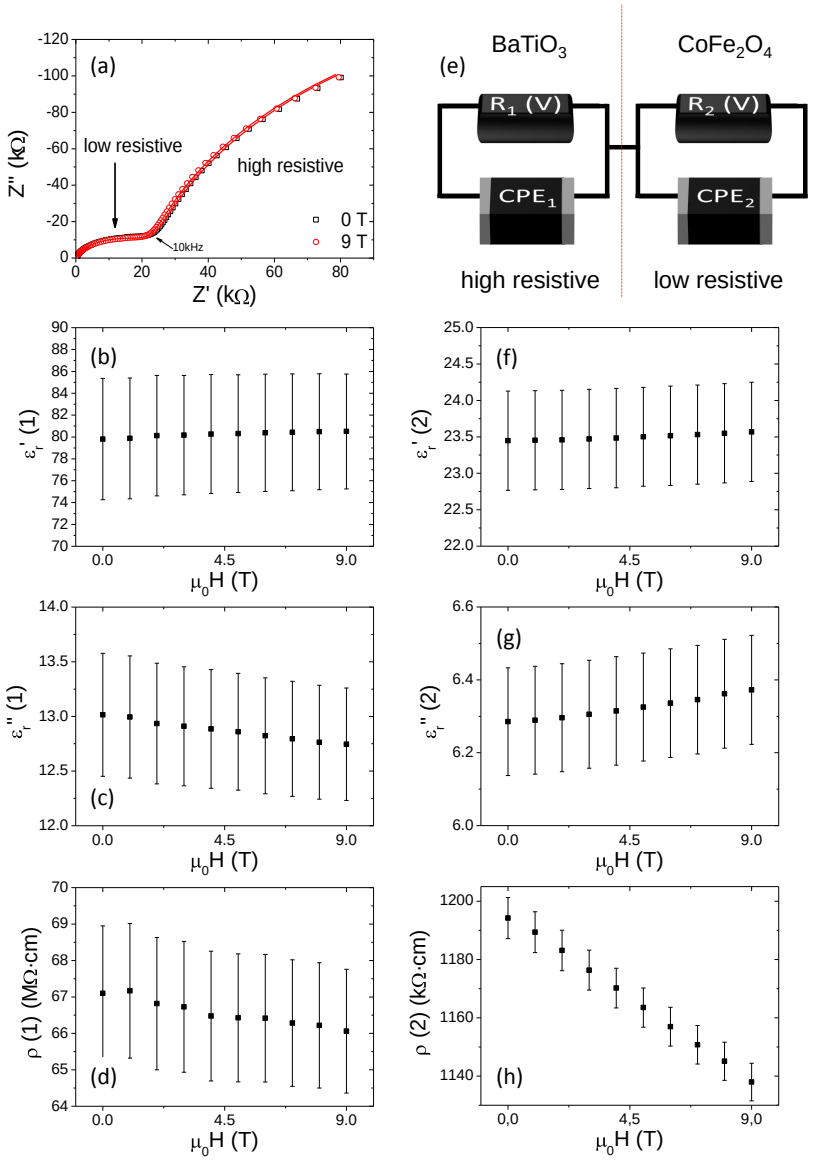

Figure 4.4: *Impedance spectroscopy data for SB25C100 sample. (a) Nqvist diagram. Solid line corresponds to the fitting performed with the equivalent circuit of figure (e). Results for the resistivity (b), real (c) and imaginary (d) part of dielectric permittivity for the high resistive RCPE element ascribed to $BaTiO_3$. Idem for $CoFe_2O_4$ in (f-h). Error bars are determined by the fitting program.*

results suggest that the measured magnetodielectric effect can be dominated by $CoFe_2O_4$ magnetoresistance at the measurement temperature.

In contrast, this effect can not originate the $\Delta\epsilon(T)$ anomalies, because it would imply that $CoFe_2O_4$ displays distinctive magnetoresistance anomalies at T_1', T_2', and T_3', and there is no reason for this.

4.3 Strain effects on ferroelectric properties

In the previous section magnetoelectric coupling has been analyzed as a function of stacking sequence in a particular bilayered structure. Here, the ferroelectric properties dependence on $BaTiO_3$-$CoFe_2O_4$ stacking order, $BaTiO_3$ thickness, and bottom electrode are analyzed in detail in terms of $BaTiO_3$ structural properties.

We recall here the main structural properties of the studied samples of table 4.1:

- In bottom-BTO samples two $BaTiO_3$ phases can be found. The first phase corresponds to a most strained $BaTiO_3$ with an enhanced tetragonality ($c/a^* \approx 1.1$). The second would correspond to a less strained $BaTiO_3$, with a lower tetragonality ($c/a \approx 1.05$), although it is still larger than for bulk $BaTiO_3$ ($c/a_{bulk} = 1.01$). This indicates the presence of two $BaTiO_3$ phases with ddifferent strain.

- In top-BTO samples a c/a ratio near 1 is measured, which indicates that $BaTiO_3$ layer is near bulk-like $BaTiO_3$.

Figures 4.5 show the ferroelectric loops (I-E characteristics and integrated P-E loops) for all the samples. First, we observe that all the samples are ferroelectric. This can be inferred from the I-E characteristics in figure 4.5(b,d), where the current peaks that correspond to the ferroelectric switching are visible.

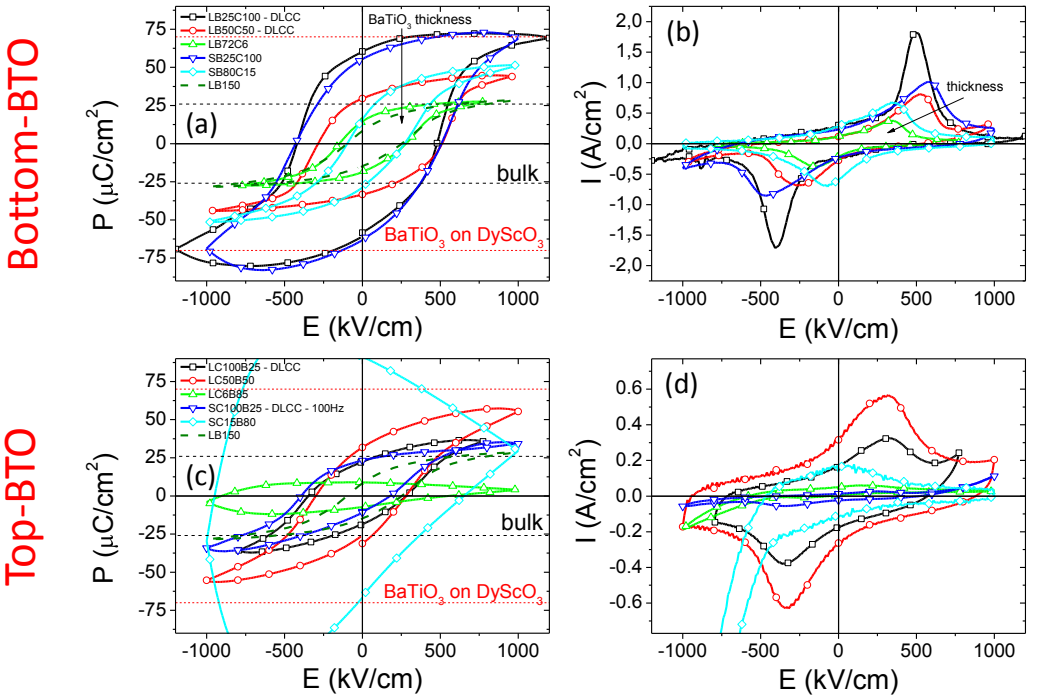

Figure 4.5: *P-E loop (a) integrated from I-E characteristics (b) at 1 kHz for $BaTiO_3$-$CoFe_2O_4$ bilayers with $BaTiO_3$ on bottom. (c,d) Idem for samples with $BaTiO_3$ on top. Loops labeled with DLCC have been obtained after the application of DLCC compensation. Note that the loops obtained for SC100B25 have been measured at 100Hz. Dashed lines indicate saturation polarization values for bulk $BaTiO_3$ [71] (black) and for strained $BaTiO_3$ grown on $DyScO_3$ [185] (red). Labels of the samples are summarized in table 4.1.*

Bottom-BTO samples [fig. 4.5(b)] show well-visible ferroelectric current peaks, consequence of high polarization values. On the contrary, top-BTO samples [fig. 4.5(d)] show less visible current peaks.

Figure 4.5(a) shows the integrated P-E loops for bottom-BTO samples; it can be observed that the polarization decreases while decreasing the sample thickness, from values near to those obtained in highly compressively strained $BaTiO_3$ ($BaTiO_3$ grown on $DyScO_3$ [185]) to bulk values [71] (dashed lines). Electric coercive field shows a similar tendency, as it can be seen in figure 4.5(b) by the shift of ferroelectric current peak towards lower field values.

In figure 4.5(c), it is displayed the integrated P-E loops for top-BTO samples. The measured polarization values are of the order of bulk for the films with thinner $BaTiO_3$ (i.e. SC100B25, LC100B25), and even larger than bulk for the intermediate $BaTiO_3$ thickness (LC50B50). Regarding the thick $BaTiO_3$ top-BTO samples (SC15B80, LC6B85), leakage does not allow to extract reliable polarization values.

The polarization values obtained in thin $BaTiO_3$ (of top-BTO set of samples) are noticeable because, in spite of the tensile strain induced by $CoFe_2O_4$ on top $BaTiO_3$ layer ($\approx +5\%$), these are near bulk. We have ascribed this finding to the fact that these films are relaxed with bulk-like tetragonality, so they should display bulk like polarization. This result improves the previous results obtained on $BaTiO_3$-$CoFe_2O_4$ heterostructures, where ferroelectric switching can only be clearly observed for thicknesses beyond 60 nm [170], and differs from the obtained in similar heterostructures with $Pb(Zr_{1-x}Ti_x)O_3$, which always display polarization values lower than that reported in bulk [52, 55, 65, 159].

It is remarkable that, irrespective of the bottom electrode, P-E loops are very similar in all the samples. This is expected owing to the fact that bottom electrodes grow epitaxial and coherently on top of the substrate, which results in no change of in-plane lattice parameters comparing samples grown on $La_{2/3}Sr_{1/3}MnO_3$ and $SrRuO_3$.

Finally, it is also interesting to note that the loops show visible horizontal shift, consequence of the imprint. The samples with bottom-BTO have a negative imprint, while in the top-BTO samples the imprint is positive, moreover as the thickness increases, imprint increases.

In the following sections, we will discuss the polarization dependence on tetragonality and strain gradient for bottom-BTO samples, and show the imprint dependence on bilayer stacking sequence and $BaTiO_3$ thickness.

4.3.1 Polarization dependence on tetragonality

We have observed that polarization depends on $BaTiO_3$ thickness for bottom-BTO samples [fig. 4.5(a)]. Moreover, we have also observed that bottom-BTO samples show an step-like strain gradient(section 4.1). These features invite us to think that strain and polarization are correlated. Therefore, we have plotted polarization versus c/a parameter in figure 4.6(a). From the figure it is difficult to disclose a direct correlation between P and c/a, because some films present both (more and less strained) $BaTiO_3$ phases [indicated with two points with different c/a values and grouped with a rectangle in figure 4.6(a)]. However, if we take into account that in the thinner films the more strained $BaTiO_3$ phase should be more abundant [less abundant phase is indicated with an arrow and with points of smaller size in fig. 4.6(a)] and subsequently, it should weight more in the measured polarization value than in the thicker films, a correlation is found. This result shows that polarization and tetragonality in $BaTiO_3$ are correlated as it has been already reported in ferroelectric single-layers [see f.i. [186, 187]].

The dependence of polarization on strain can be more accurately analyzed, if we take into account the strain profile in the $BaTiO_3$ layer. The most simple explanation for the two different strained $BaTiO_3$ phases is an abrupt relaxation of the $BaTiO_3$ at a given distance (z) from the film-electrode interface. This suggests that strain performs the step-like profile that follows:

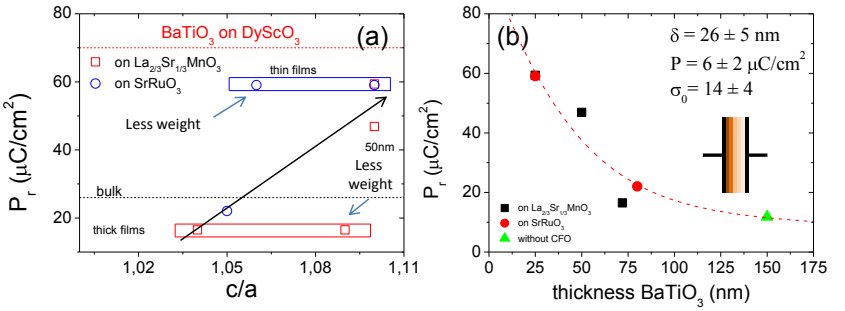

Figure 4.6: *(a) Remanent polarization versus c/a ratio for the series of samples with bottom $BaTiO_3$. Rectangles group the c/a values that correspond to different strain phases $BaTiO_3$ in the same sample. Polarization values for bulk $BaTiO_3$ [71] and highly strained $BaTiO_3$ films growth on $DyScO_3$ [185] are indicated by dashed lines. (b) Remanent polarization dependence on thickness for bottom-BTO samples. Dashed line fits the data points according to equation 4.5.*

$$\sigma(x) = \begin{cases} \sigma_1 & x < \delta \\ \sigma_2 & x > \delta \end{cases} \tag{4.1}$$

where σ is the tetragonal strain defined as $\sigma = \frac{(c/a)-(c/a)_{bulk}}{(c/a)_{bulk}}$, σ_1 and σ_2 are the characteristic strains of the two phases, and δ is the thickness of the phase corresponding to σ_1. This model has been used to analyze the data; however, due to the few available experimental points, the obtained results do not converge in a reliable manner. That is the reason why we have used a simpler exponential model, where strain gradually decreases. This model, in spite of being less accurate to our data, is more general, and has one free parameter less, allowing the more accurate extraction of characteristic parameters, as it is described below. The equation that describes the exponential decrease of the strain across the film is [188]:

$$\sigma(z) = \sigma_0 e^{-z/\delta} \tag{4.2}$$

where σ_0 is the strain at the interface.

As it is suggested by the figure 4.6(a), we assume that polarization is proportional to the tetragonality ($P \propto c/a$); under this assumption the film can be modeled as a series of capacitors with a decrease in the permittivity as z increases (sketched in the inset of fig. 4.6(b)); therefore, the polarization across the film will be given by

$$P(Z) \propto \epsilon(z) = \alpha \cdot (c/a)(z) = \epsilon_\infty(\sigma(z) + 1) \tag{4.3}$$

and the permittivity for this system will be given by

$$\frac{t}{\epsilon} = \sum_i \frac{t_i}{\epsilon_i} = \int_0^t \frac{dz}{\epsilon(z)} \tag{4.4}$$

where t is the thickness of the sample, and ϵ_∞ is the permittivity for the equivalent sample at infinite distance from the substrate. Consequently, the polarization for a sample of a certain t thickness will be given by

$$P(t) = \frac{t \cdot P_\infty}{t + \delta \cdot ln\frac{1+\sigma_0 e^{-t/\delta}}{1+\sigma_0}} \tag{4.5}$$

The resulting equation has been fitted to the obtained data [fig. 4.6b] providing a value of 26 ± 5 nm for δ. This value is lower than the experimentally obtained in a similar ferroelectric as $Ba_{0.5}Sr_{0.5}TiO_3$, which is around 100 nm [189], most probably because in the referred case the lattice mismatch is smaller (around 1 % in front of our 2 %) and the relaxation is more gradual. The values for P_∞[1] and σ_0 are 6 ± 2 $\mu C/cm^2$ and 14 ± 4, respectively.

The performed analysis indicates that polarization can be controlled by epitaxial strain, being $BaTiO_3$ c/a ratio the key factor that determines the polarization magnitude.

[1]Note that P_∞ is the polarization of $BaTiO_3$ layer at infinite distance from the film-electrode interface and it should not be the bulk value.

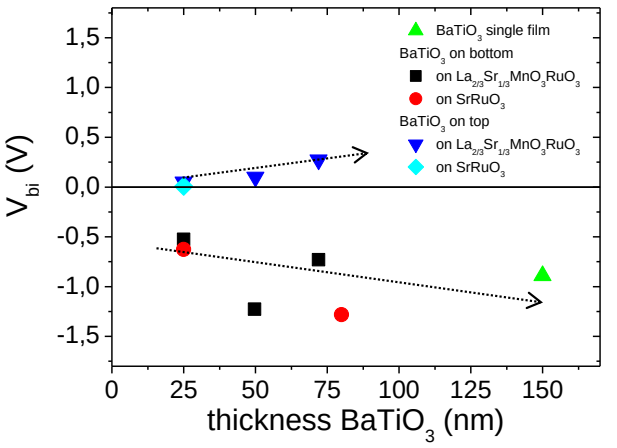

Figure 4.7: *V_{bi} versus $BaTiO_3$ thickness for all the samples.*

4.3.2 Imprint dependence $BaTiO_3$ thickness and stacking order

Imprint is a consequence of a built-in voltage common in ferroelectrics that causes the preference of a certain polarization state over the other. This asymmetry results in a shift of the hysteresis loop along the electric field axis, as the vertical position of the loop is arbitrarily set. This shift in the ferroelectric hysteresis loop corresponds to this built-in voltage ($V_{bi} = (V_c^+ + V_c^-)/2$), where $V_c^{\pm}$ are the positive and negative coercive voltages). The imprint may have several different origins; however, it is usually associated with degraded ferroelectric film, because it is usually ascribed to charge defects [190].

Figure 4.7 shows the V_{bi} dependence on thickness for the different samples with different stacking order. The most remarkable feature is the dependence of the V_{bi} sign on the stacking order. Second, in spite of the dispersion of the data, an increase of the imprint with thickness can be observed, even for the reference sample without $CoFe_2O_4$.

Due to the different work functions (Φ^0) of the electrodes [$La_{2/3}Sr_{1/3}MnO_3$

or $SrRuO_3$ and Pt, [191, 192]] and to the fact that in a metal-ferroelectric interface having a Schottky contact is most probable [88, 193, 194], the formation of a built-in voltage is expected [88, 89]. In fact the reference sample without $CoFe_2O_4$ displays negative V_{bi}. If we suppose that the electric properties of $BaTiO_3$ are the same in both metal-ferroelectric interfaces and taking into account the Pt and $La_{2/3}Sr_{1/3}MnO_3$ work functions, a negative built-in voltage ($V_{bi} \propto -\Phi^0_{Pt} + \Phi^0_{SRO,LSMO}$ [88]) is expected. A similar argument can be applicable for all bottom-BTO samples. However, the origin of V_{bi} increase with thickness is more difficult to understand with the available data. We suggest that it can be due to the strain gradient present in $BaTiO_3$ layer, and/or to the differences in the metal-ferroelectric interface as the $BaTiO_3$ thickness increases. On the other hand, the change of sign of V_{bi} in top-BTO samples indicates that metal-$CoFe_2O_4$ interface contributes in a relevant manner.

4.4 Conclusions

We have shown that ferroelectric and magnetoelectric properties are modified depending on the stacking order of the $BaTiO_3$-$CoFe_2O_4$ bilayer. Moreover, we have also seen that irrespective of $BaTiO_3$ thickness and $BaTiO_3$-$CoFe_2O_4$ stacking order the studied bilayers are always ferroelectric. These results are remarkable in terms of the future integration of this system in a multilayered structure.

We have observed that when $BaTiO_3$ is grown at the bottom, it suffers compressive strain induced by the substrate; this enhances $BaTiO_3$ tetragonality, and, subsequently, the ferroelectric properties. For $BaTiO_3$ on top bilayers, it grows nearly relaxed and ferroelectric polarization is near the bulk values.

A large variation of the dielectric permittivity under the application of magnetic field (up to 36 %) is found for top-BTO bilayer, near $BaTiO_3$ ferro-

electric transition temperatures. For bottom-BTO sample discontinuities in magnetodielectric effect near ferroelectric transition temperatures of $BaTiO_3$, also appear but with lower intensity. We ascribe this last result to the fact that there is a larger clamping between the ferroelectric and the substrate in bottom-BTO sample, which partially anihilates the possible magnetoelectric coupling between the two functional layers. Contrary to this, when $BaTiO_3$ is grown on top of thick $CoFe_2O_4$ the clamping to the substrate is released at the same time that the coupling between $CoFe_2O_4$ and $BaTiO_3$ is enhanced, resulting in a larger magnetoelectric response.

Moreover, we have also shown that via modifying $BaTiO_3$ thickness and consequently the induced substrate strain in $CoFe_2O_4/BaTiO_3$ bilayers, $BaTiO_3$ tetragonality can be tailored leading to the control of the polarization values. Our results also revealed the presence of a V_{bi} that depends on $BaTiO_3$ thickness and stacking order.

Chapter 5

$CoFe_2O_4$ and $BaTiO_3$ vertical nanocomposites

Vertical nanostructured self-assembled composite thin films are made of nanocolumns of a magnetostrictive-ferromagnetic spinel embedded in a matrix of a piezoelectric-ferroelectric perovskite (in this work $BaTiO_3$ and $CoFe_2O_4$ respectively), or vice versa. A milestone in the study of this architecture in thin film form was the growth of $BaTiO_3$-$CoFe_2O_4$ nanocomposites reported by Zheng et al. [15], who were able to grow nanocolumns of $CoFe_2O_4$ embedded in a matrix of $BaTiO_3$ with both ferroic orders (electric and magnetic) at room temperature and coupling between them. Since this relevant finding, much interest has been focused on composites combining different magnetic and ferroelectric materials [15, 56, 66, 67, 195–213].

In these materials nanocolumns are self-assembled when mixing ferromagnetic spinel with ferroelectric perovskite. Epitaxial films have vertical architecture when deposited (001)-textured on (001) perovskite substrates ($SrTiO_3$): spinel grows as nano-pillars embedded in the perovskite matrix [15, 195, 196], because the perovskite wets better on (001) perovskite substrates than the spinel [200]. Otherwise, perovskite columns grow within a spinel matrix when growing the heterostructures on (111) perovskite

substrates($SrTiO_3$). Therefore, the different crystal structure of the ferroelectric and the ferromagnet helps to its self-assembled groth with good crystallinity [195–197, 199, 200, 202, 207, 208, 213].

In vertical composites, the limiting factor for good ferroelectric properties is the leakage. As mentioned in the previous chapter, the leakage is determined by the ferromagnet, which is usually a poorer insulator than the ferroelectric phase. Several groups have reported on evidences of multiferroicity [15, 56, 66, 67, 196, 200, 201, 206, 207], which have demonstrated the technological interest of the architecture.

The area of the interface between both phases is maximized in this geometry, which should result in an enhancement of magnetoelectric coupling. Another advantage is that substrate clamping effect is reduced because here the strain coupling occurs along vertical interfaces. However, magnetoelectric coupling measurements can also be affected by leakage; that is the reason why in only a few works the magnetoelectric coupling using electric measurements is evaluated [56, 212], and most of the performed characterization has been done using non-direct techniques or performing experiments at the nanoscale [15, 66, 67, 209].

In this thesis, we have focused on $BaTiO_3$-$CoFe_2O_4$ composites grown on (001) $SrTiO_3$ substrates, therefore $CoFe_2O_4$ nanocolumns are formed in a $BaTiO_3$ matrix. Whereas there are several reports on the magnetic properties of these structures [201, 206], the dependence of dielectric and ferroelectric properties on deposition conditions and correlations with structural properties have not been reported yet.

The present chapter is devoted to: analyze the ferroelectric (section 5.2) and magnetoelectric (section 5.3) properties of nanocomposite films grown by rf sputtering. The dependence of the ferroelectric and dielectric properties on growth conditions will be analyzed in section 5.4. The studied samples are described in next section.

Table 5.1: *$BaTiO_3$ unit-cell volume (V) and plateau size (PS) of $BaTiO_3$-$CoFe_2O_4$ nanocomposite thin films with different growth conditions: temperature (T) and growth rate (GR), and different thickness (t).*

Label	T (^oC)	t (nm)	GR (nm/min)	V (Å^3)	PS (nm)
T5GR3t165	850	165	2.8	65.28	138
T4GR3t165	**825**	**165**	**2.8**	**65.57**	**114**
T3GR3t165	800	165	2.8	65.93	86
T2GR3t165	775	165	2.8	66.18	39
T1GR3t165	750	165	2.8	67.22	58
T4GR3t90	**825**	**90**	**2.8**	**65.63**	**81**
T4GR3t255	825	255	2.8	65.58	131
T4GR3t345	825	345	2.8	65.40	162
T4GR2t150	825	150	1.4	65.20	113
T4GR1t90	825	90	0.5	64.52	137

5.1 Samples

Epitaxial nanocomposite films of $BaTiO_3$-$CoFe_2O_4$ (2/3 and 1/3 of molar ratio, respectively) with different thicknesses, and grown at different conditions by rf sputtering on (001) Nb:$SrTiO_3$ substrates were prepared. Extensive details on sample preparation and structural and microstructural characterization are described in the Ph.D. work of N.Dix [70] and have been reported elsewhere [214]. Here we only summarize the more relevant results. In short, $CoFe_2O_4$ nanocolumns are embedded in a $BaTiO_3$ matrix (sketched in figure 5.1). Due to the respective spinel and perovskite structure of $CoFe_2O_4$ and $BaTiO_3$, the $CoFe_2O_4$ nanocolumns emerge on the surface like pyramids, whereas $BaTiO_3$ matrix is composed by square-like grains. Both $BaTiO_3$ and $CoFe_2O_4$ are (001) textured in almost all the samples.

The here studied samples are summarized in table 5.1. The growth conditions have been varied by changing the growth rate (by changing the power

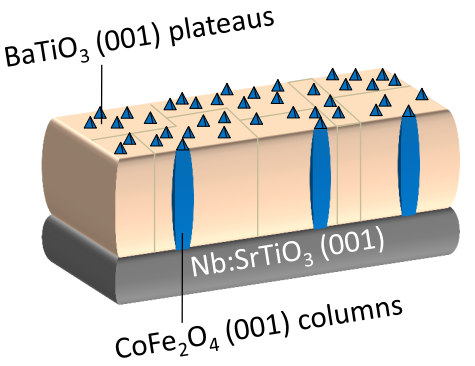

Figure 5.1: *Sketch of studied $BaTiO_3$-$CoFe_2O_4$ nanocomposite.*

of the rf sputtering) and the substrate temperature during the deposition; moreover, films with different thicknesses have also been grown. Therefore, the samples are classified in three sets according to the changed parameter: the deposition temperature, the growth rate, and the thickness. The growth conditions are summarized in table 5.1.

From the structural point of view, as mentioned, almost all the samples are $(00l)$ single textured and the $BaTiO_3$ and $CoFe_2O_4$ reflections are clearly separated, except for two cases: i) for the samples deposited at $T_S < 775^oC$ the out-of-plane diffraction peaks of $CoFe_2O_4$ and $BaTiO_3$ merge and become indistinguishable (T1GR3t165, and T2GR3t165), ii) the samples grown at very low growth rate (0.5 nm/min, T4GR1t90) and the thicker samples (255 and 345 nm, labeled as T4GR3t255 and T4GR3t345) have traces of polycrystalline reflections.

From reciprocal space maps, in-plane and out-of-plane parameters have been extracted, and from them the $BaTiO_3$ unit cell volume has been calculated (summarized in table 5.1). It turns out that $BaTiO_3$ unit cell volume for all our samples is larger than in bulk ($V_{bulk} = 64.32$ Å^3)[1]. This expansion

[1]In ref. [214] it is shown that the expansion of the volume cell is due to an expansion of all axes, separately.

of the unit cell volume is more important for samples grown at lower temperature and for increasing growth rates. When increasing thickness the unit cell volume reduces a bit, although it remains larger than bulk. It is worth noting that films displaying a polycrystalline character (additional reflections like (lll) or $(ll0)$) tend to have more bulk-like parameters and, consequently, the unit cell volume is reduced, approaching bulk value.

Morphologically, the studied nanocomposite films show clearly the typical surface topology of a matrix-column composite film. As mentioned, the $BaTiO_3$ matrix is not continuous. It is observed to grow with a columnar morphology that generates squared plateaus in the surface (fig. 5.1). The average size of these $BaTiO_3$ plateaus (measured as the average laterel size of the plateau) for the different samples is summarized in table 5.1. We have observed that the $BaTiO_3$ plateaus increase their size with temperature, growth rate and thickness (table 5.1). The matrix ($BaTiO_3$) plus columns ($CoFe_2O_4$) morphology is observed for all the samples except for those displaying overlapping of the $CoFe_2O_4$ and $BaTiO_3$ reflections (T1GR3t165, and T2GR3t165 samples), which show purely granular (round shape) surface (the size of the grains has been ascribed to plateau size in table 5.1), and polycrystalline reflections (T4GR1t90, T4GR3t255 and T4GR3t345) that show not square-like grains (in this latter case these not squared grains have not been taken into account in the calculation of the average plateau size).

Summarizing, we can conclude that T4GR3t165, T3GR3t165, T4GR3t90, T4GR2t150 are optimal samples from structural (do not display policristaline reflections or $CoFe_2O_4$ /$BaTiO_3$ phase overlapping) and morphological (show $CoFe_2O_4$ columns embedded in a matrix formed by squared $BaTiO_3$ plateaus) point of views.

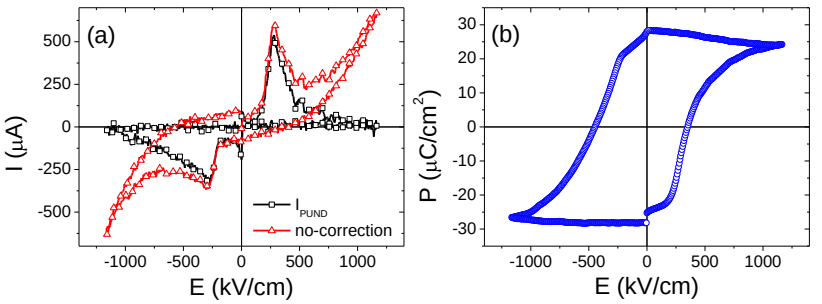

Figure 5.2: *(a) Current versus electric field characteristics as measured and after PUND correction at 250 Hz. (b) Polarization versus electric field integration of figure (a).*

5.2 Ferroelectric properties

We study in this section the ferroelectric behavior of $BaTiO_3$-$CoFe_2O_4$ nanocomposite thin film. To that purpose an optimal 90 nm nanocomposite (from structural and morphological point of view) film is used in the present section (T4GR3t90 sample highlighted in table 5.1).

In figure 5.2(a), the PUND measurement for the referred sample is displayed. The line labeled with up-triangles corresponds to the as measured I-E curve at 250 Hz. It can be seen that leakage current at high fields is comparable to the ferroelectric switching current peak. In spite of the leakage, after subtracting it using PUND protocol, as described in chapter 1 (line with squares), the two ferroelectric peaks can be clearly isolated. This demonstrates that the sample is ferroelectric. Polarization can be obtained by integrating the corrected I-E characteristics, as displayed in figure 5.2(b).

The obtained polarization is $P_r = 27(1)\ \mu C/cm^2$. Taking into account the fact that $CoFe_2O_4$ is not ferroelectric and that the surface occupied by $BaTiO_3$ is $\approx 2/3$, a polarization of $\approx 40 \mu C/cm^2$ would correspond to the $BaTiO_3$ fraction of the film. This value is larger than bulk ($\approx 26\ \mu C/cm^2$ [71]); thus suggesting that the experimental value is probably overestimated

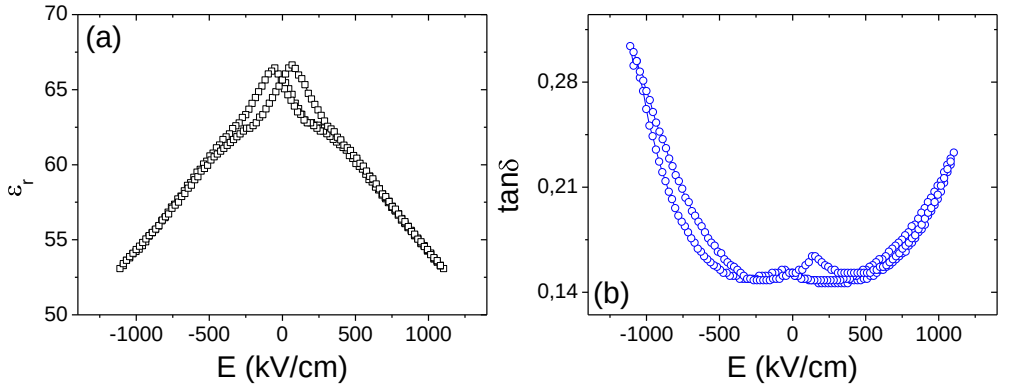

Figure 5.3: *(a) Dielectric permittivity and (b) losses dependence on electric field.*

because of the presence of leakage as mentioned in section 2.3, and/or because the $BaTiO_3$ surface area is not exactly 2/3.

In figure 5.3(a) we show the hysteretic behavior in ϵ-E loop, which is signature of the ferroelectric nature of the material. Note that this loop has a smaller coercive field (≈50 kV/cm) than the one obtained by the I-E characteristics (≈250 kV/cm). This is due to the different frequencies used in both measurements. While in the I-E loop the measurement is at 250 Hz, the ϵ-E loop is recorded quasi statically. Since coercive field in ferroelectrics usually depends exponentially on frequency, this discrepancy is expected, as mentioned in section 2.3.2.

The hysteresis is also well-visible in the tanδ-E data shown in figure 5.3(b). The effect of leakage can also be observed in the rapid increase of tanδ at high electric fields.

The important leakage, observed in either P-E or ϵ-E measurements is most probably due to the presence of boundaries between $BaTiO_3$ plateaus (equivalent to grain boundaries) and/or the presence of the $CoFe_2O_4$ columns. $CoFe_2O_4$ columns and grain boundaries can act as conductive channels through the insulating matrix. In fact, even though $CoFe_2O_4$ is insulating, it has

a very low band gap and resistivity (less than 0.5 eV [183, 215], while for $BaTiO_3$ it is around 3eV [184, 216]). Consequently, defects can induce a high leakage current.

The data show that nanocomposite thin films grown by rf sputtering preserve the ferroelectric nature of $BaTiO_3$. This, together with the already reported magnetic data [100], demonstrates the possibility to obtain multiferroic $BaTiO_3$-$CoFe_2O_4$ composite thin films with vertical architecture by the sputtering technique. The observed ferroelectric polarization, in spite of the presence of leakage, is comparable to that obtained for similar nanocomposites grown by PLD [15].

5.3 Magnetoelectric coupling

Now we explore the possible existence of magnetoelectric coupling by means of magnetodielectric measurements. To that propose, an optimal 165 nm sample has been used (T4GR3t165 sample highlighted in table 5.1). The chosen sample is very suitable for magnetodielectric measurements, because the dielectric permittivity and losses [later displayed in fig. 5.7(a,b)] show low dependence on frequency. As described in section 2.2, a reduced dependence of the impedance on frequency should help to reduce the extrinsic contributions to the measured magnetodielectric effect. Indeed, minor ferroelectric loops applying DLCC have been measured as show in figure 5.8 for this sample.

The temperature dependence of the change of dielectric permittivity under an applied magnetic field of 8 T with respect to its value at 0 T ($\Delta\epsilon = \frac{\epsilon(\mu_0 H) - \epsilon(\mu_0 H=0)}{\epsilon(\mu_0 H=0)}$) is shown in figure 5.4. It can be seen that $\Delta\epsilon$ increases with temperature and reaches a maximum of more than 2% near 390 K. This value is not far away from the Curie temperature of bulk $BaTiO_3$ (393 K [71]), and thus it is plausible that the peak on $\Delta\epsilon$ could be related to the $BaTiO_3$ ferroelectric transition. Figure 5.4(b) shows that magnetolosses show a peak at a different temperature than $\Delta\epsilon$. Moreover, the losses dependence on

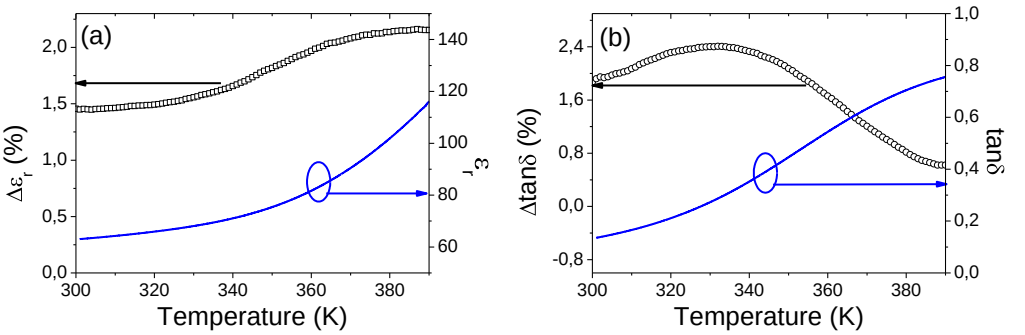

Figure 5.4: *$\Delta\epsilon$ (a) and $\Delta tan\delta$ (b) dependence on temperature at 100 kHz, on the left axes. epsilon (a) and tanδ (b) dependence on temperature at 100 kHz, on the right axes.*

temperature (right axis in fig. 5.4(b)) reveals that losses increase significantly with temperature. Both facts cast some doubts about the reliability of the measured magnetodielectric response.

Isothermal-room temperature magnetodielectric measurements at 10 kHz are displayed in figure 5.5. The figure shows that magnetodielectric coefficient is around 0.06%/T. Moreover, from the figure, it can also be inferred that the ϵ-H loop shows hysteretic behaviour, which is attributed to the $CoFe_2O_4$ ferromagnetism. This is confirmed by the magnetic susceptibility loop plotted in the same figure (right-axis), that shows the coincidence of the maximum and minimun value of magnetic susceptibility (the derivative of the M-H measured loop) and dielectric permittivity, respectively.

In figure 5.6, we show the dependence of the dielectric permittivity on magnetic field at various frequencies, which clearly reveals that ϵ and tanδ variations strongly depend on frequency. This result suggests that the measured magnetodielectric effect is not due to an intrinsic coupling between the two referred ferroic orders.

As discussed in section 2.2.2, in the presence of Maxwell-Wagner behavior, a finite magnetodielectric response can be measured if there is a magnetore-

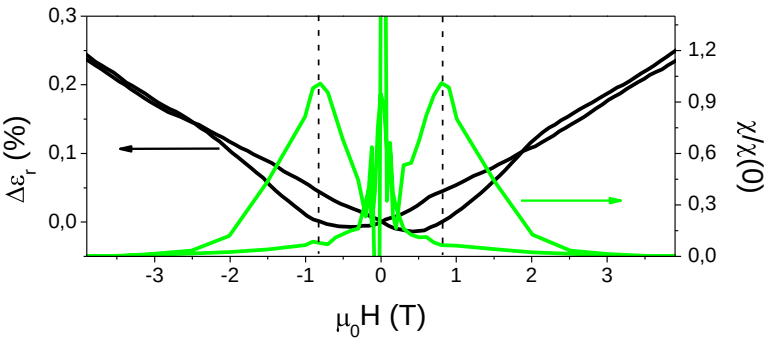

Figure 5.5: *(left-axis) Variation of dielectric permittivity at 10 kHz under the application of magnetic field out of plane. (right-axis) Magnetic susceptibility versus magnetic field characteristics extracted from the magnetic m(H) loop from ref. [100].*

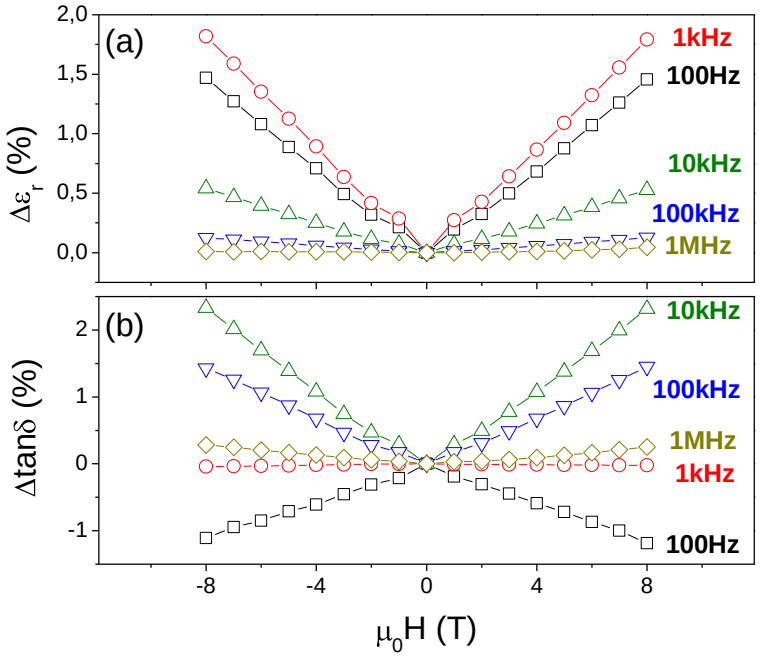

Figure 5.6: *Variation of dielectric permittivity (a) and losses (b) at various frequencies under the application of magnetic field.*

sistance contribution of the material. Impedance spectra at 300 K [5.7(a,b)] are not conclusive about the presence of this behavior because the resistance of the film is high; however, at 380 K [5.7(c,d)] it can be easily identified by the presence of a peak in the dielectric losses, which is a signature of this phenomenon (section 2.2.2)[2].

Figures 5.7(e,f) clearly show that the dependencies on frequency of $\Delta\epsilon$ and $\Delta\tan\delta$ at 380 K are very similar, qualitatively, to the simulated in section 2.2.2 for a magnetoresistive but non-magnetodielectric material, with a peak in magnetocapacitance (lines with squares) and a change from negative to positive in magnetolosses (lines with circles) as frequency increases. As $CoFe_2O_4$ is magnetoresistive the obtained data can be a consequence of the variation of the resistance of $CoFe_2O_4$ under the application of a magnetic field. Finally, the data were analyzed by means of equivalent circuit in order to isolate the magnetoresistive contributions from the magnetodielectric ones (not shown). Unfortunately, the small variations found for dielectric permittivity and conductivity of both contributions are always below the fitting error; thus, both contributions can not be separated.

Summarizing, the observed magnetodielectric effect, about 2 %, is comparable with the reported data in the characterized horizontal heterostructures of the previous chapter (to our knowledge there are not reported data on magnetodielectric measurements in $BaTiO_3$-$CoFe_2O_4$ vertical heterostructures). However, we can not discern if the measured effect is purely magnetoelectric, i.e. due to the strain coupling between $CoFe_2O_4$ and $BaTiO_3$, or only due to the magnetoresistance of $CoFe_2O_4$.

[2]The reason why Maxwell-Wagner behavior is observed at high temperature is because the resistance of the intrinsic contribution decreases and this provokes a displacement of the peak of dielectric losses to higher frequencies. Most probably, at low temperature it is not visible because it is present at a lower frequency than the measured range.

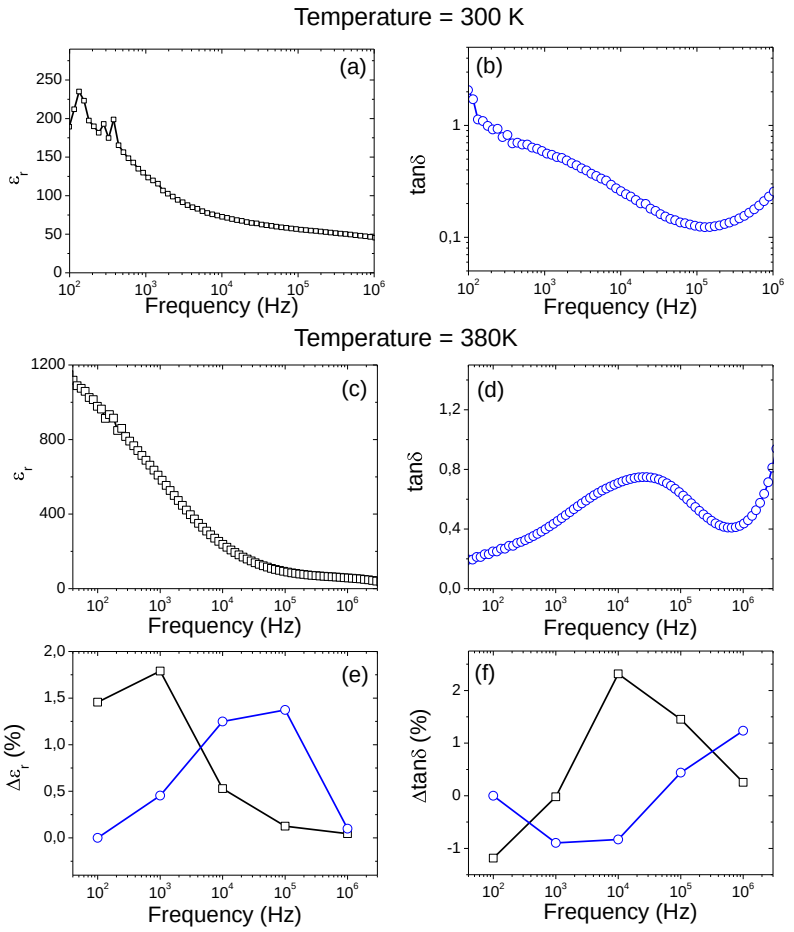

Figure 5.7: *ϵ (a) and tanδ (b) dependence on frequency at 300 K. ϵ (c) and tanδ (e) dependence on frequency at 380 K. $\Delta\epsilon$ (a) and Δtanδ (b) dependence on frequency at 300 K (lines with squares) and at 380 K (lines with circles).*

5.4 Effects of morphology and strain on dielectric properties

In previous sections the ferroelectric character of representative nanocomposite has been demonstrated and magnetodielectric response has been discussed. Now we will focus on the evolution of the ferroelectric and dielectric response of multiferroic $BaTiO_3$-$CoFe_2O_4$ columnar nanocomposite thin films obtained at different deposition temperatures, growth rate and with different thicknesses (samples in table 5.1). We will correlate the microstructure with dielectric response, while demonstrating that samples preserve their ferroelectric character for all the studied growth conditions. More specifically, we show that the dielectric permittivity depends on the grain size and unit cell volume of the $BaTiO_3$ matrix, while the dielectric losses remain nearly constant for the studied films. The implications of these results in view of tailoring these materials will be discussed.

First, we will focus on the ferroelectric behavior. Ferroelectric loops are shown in figure 5.8. Unfortunately, saturated ferroelectric loops have been obtained only for the set grown at the same temperature (825 ^{o}) and varying the growth rate[3]. In figure 5.8(b), the loops of this set after leakage subtraction are presented. For the other two sets of samples: varying the deposition temperature [fig. 5.8(a)] and thickness [fig. 5.8(c)], only minor loops without a clear ferroelectric switching peak have been measured (after DLCC), and therefore, it has not been possible to stablish any correlation between polarization and growth conditions. For this reason the values of remanent polarization collected in figures fig. 5.8 can not be compared. Consequently, we have focused our efforts on the correlation of the dielectric permittivity and the structure and morphology of the composites.

[3]For samples in which proper PUND measurement has been measured, it is shown in the figure 5.8, instead of DLCC measurements.

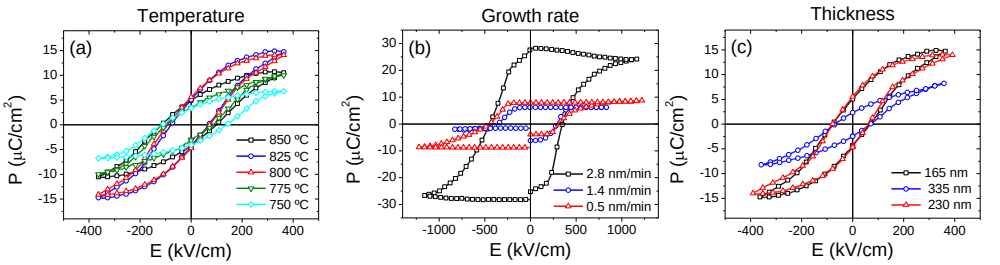

Figure 5.8: *P-E characteristics for samples grown at different temperature (a), and with different growth rate (b), and with different thickness. DLCC has been applied in the measurements plotted in figures (a) and (c), and PUND correction in figure (b).*

One example of the dependence of the dielectric permittivity ϵ and loss tangent $\tan\delta$ on frequency was already shown in figures 5.7(a,b) for one representative sample (T4GR3t165). The strong frequency dependence of both quantities observed at low frequencies corresponds to the electronic transport (discussed in section 2.2). As the frequency increases, the dependences become much smoother and, as expected, a plateau is reached near 100 kHz. Thus we chose this frequency to compare the dielectric permittivity for all the samples.

Figures 5.9 show the dependences of ϵ and $\tan\delta$ on the deposition conditions and thickness. While a nearly constant $\tan\delta \approx 0.15$ is observed for all the films, the dielectric permittivity varies between 20 and 80 and displays different tendencies with the different parameters.

- As a function of deposition temperature [fig. 5.9(a)], ϵ displays two regimes which correspond to samples grown at deposition temperatures either above or below 800ºC. Note that this deposition temperature is the same at which a clear evidence for the formation of the matrix-column nanocomposite appears (plateau-like $BaTiO_3$ surface + pyramidal CFO columns), together with a clear observation of phase separation (clear splitting between $BaTiO_3$ and $CoFe_2O_4$ diffraction peaks). For deposi-

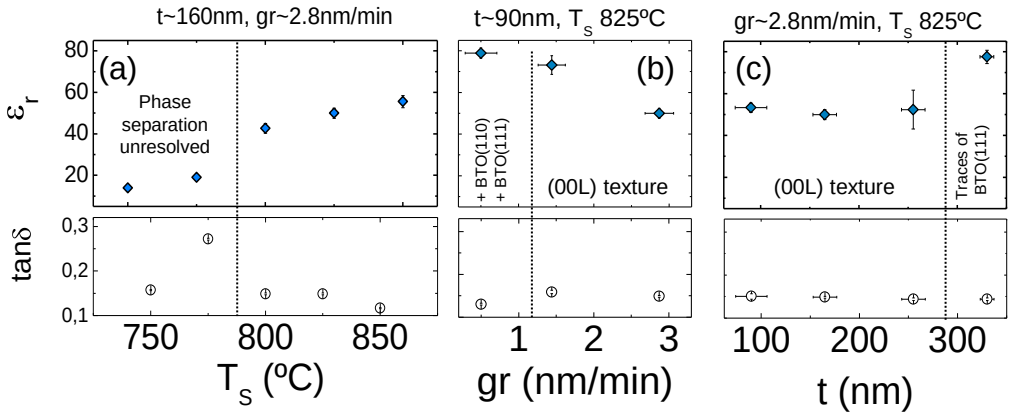

Figure 5.9: *Values for dielectric permittivity (upper-panels) and losses (bottom-panels) at 100 kHz for the samples grown at different temperature (a), growth rate (b), and with different thicknesses (c).*

tion temperatures below 800^{o}C, where more granular films are observed, ϵ displays lower values. Therefore, the appearance of the plateaus and columns is accompanied by a clear increase of ϵ [4]. Further increase of deposition temperature still rises ϵ, but more gradually.

- Decreasing the growth rate has a similar effect to increasing deposition temperature [fig. 5.9(b)]. This is somehow expected because with lower growth rate the adatom diffusion time increases, equivalent to the adatom rate increase expected in the samples grown at higher temperature.

- Finally, ϵ appears not to depend on thickness [fig. 5.9(b)], except for the thickest sample, where the permittivity is larger, with values close to those obtained for the lowest growth rate (notice that the $BaTiO_3$ phase is not fully (00l) textured, as discussed in section 5.1). The low sensitivity of ϵ to the thickness corresponds to the invariance

[4]SEM images that reveal the appearance of plateaus and columns for deposition temperatures below 800^{o}C are reported in ref. [214] for the very same samples.

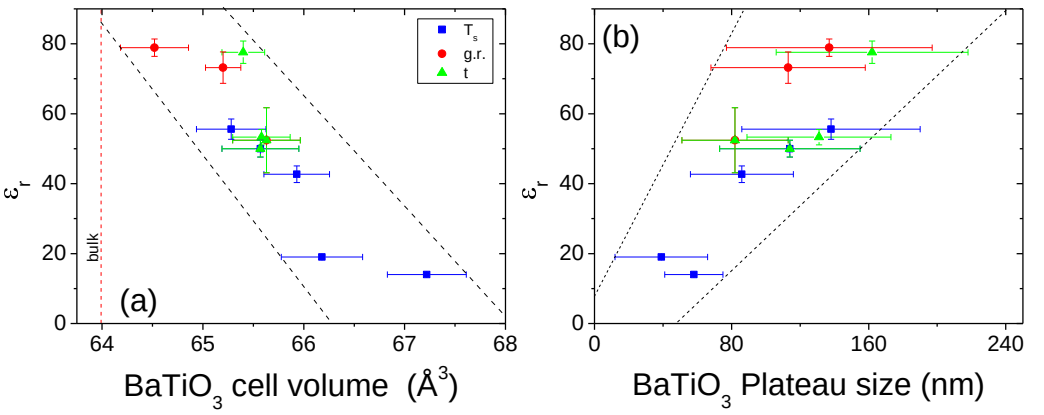

Figure 5.10: *Values of the dielectric permittivity obtained at 100 kHz plotted vs BTO cell volume (a) and grain size (b). Circles, squares, and triangles correspond to the sets of samples grown at different deposition temperature, growth rate, and with different thickness, respectively. Lines are guides to the eye. The dashed vertical line indicates the unit cell volume of bulk $BaTiO_3$.*

of morphology with film thickness; it can also be considered as an indication that the measured ϵ is not significantly affected by dead layers or other interfacial effects of the nanocomposite film with the electrodes.

We have observed that the deposition conditions determine the dielectric response, preserving the ferroelectric character of the films and giving some common tendencies with structural and morphological characteristics of the samples. Now, we try to make a step further understanding the correlation between the dielectric constant and the nanocomposite film structure and morphology. Figure 5.10 displays the evolution of the dielectric permittivity ϵ with the $BaTiO_3$ cell volume (V_{uc}) and plateau size; in spite of the substantial error bars, clear trends are appreciated, in the sense that ϵ decreases when increasing cell volume and when decreasing $BaTiO_3$ plateau size.

Let us focus on the measured values of the dielectric permittivity, $\epsilon \approx$ 20-80. Assuming that $\epsilon_{BTO} >> \epsilon_{CFO}$, the measured overall dielectric permittivity

should correspond to the dielectric permittivity of $BaTiO_3$ normalized by the composition ratio: $\epsilon = 1/3{\cdot}\epsilon_{CFO} \times 2/3{\cdot}\epsilon_{BTO} \approx 2/3{\cdot}\epsilon_{BTO}$. According to the extracted values for the dielectric permittivity of our composite films ϵ_{BTO} should range between 30 and 120. These values are substantially below the typical values found for $BaTiO_3$ (between 300 and 1000 [217–219]. The much lower values of dielectric permittivity of our samples can be ascribed to a variety of effects, including interfacial capacitances, granular character or deviations from nominal composition. These undesired effects can also be the reason for the observed permittivity ($\epsilon \approx 200$) reported in similar nanocomposites grown by PLD [15], which is certainly more similar to ϵ value obtained in our films.

Finally, we turn to the reduction of the dielectric constant when decreasing plateau-size in our films, and when increasing the $BaTiO_3$ unit cell volume. From literature, it is well known and understood that in ferroelectric thin films [219] and ceramics [220] dielectric constant increases with grain size. On the other hand, oxygen vacancies (or other compositional changes) could also result in an increase of $BaTiO_3$ unit cell volume and a subsequent decrease of ϵ [217, 221]. In our samples both parameters (grain size and unit cell volume) are also correlated; this implies that within the present data it is difficult to discern the effects of these two parameters, and no conclusion can be given.

5.5 Conclusions

The ferroelectric character of the vertical self-assembled nanocomposites grown by sputtering has been demonstrated, in spite of the presence of important leakage in all the films. Moreover, we have observed a small magnetodielectric effect (up to 2 %), which can not be concluded to be caused by the $CoFe_2O_4$ magnetostrictive or magnetoresistive response. Finally, we have shown that the dielectric permittivity is determined by the growth conditions (between 20 and 80), while dielectric losses remain constant (15%), and the ferroelectric

nature of $BaTiO_3$ is preserved. The variation of the dielectric permittivity on grown conditions has been ascribed to be induced by the variations of morphological, as well as structural, characteristics of the studied samples.

Part IV

Conclusions

Conclusions

Since the discovery of multiferroicity and magnetoelectric coupling in single-phase $TbMnO_3$ [2], and in $BaTiO_3$-$CoFe_2O_4$ composite [15], almost 10 years ago, intensive work has been done by scientific community in the field of multiferroics. In the present thesis we have performed detailed analyses of dielectric and ferroelectric properties, and magnetoelectric coupling in single-phase and composite (with vertical and horizontal architectures) multiferroic thin films.

To perform the required characterization a new experimental set-up has been designed and built. This allows to perform ferroelectric and dielectric characterization, which involves the measurement of dielectric permittivity, polarization, and pyrocurrent, controlling the temperature and the applied magnetic field. This characterization is challenging in multiferroic thin films since they are often poor insulators, and/or show relatively small polarization values (compared with common ferroelectrics); therefore, extensive efforts have been dedicated to the development of methodologies to obtain accurate dielectric and ferroelectric parameters.

We have measured ferroelectricity in epitaxial thin films of orthorhombic $YMnO_3$; and we have seen that the polarization can be controlled by an appropriate magnetic field. These results show that *bc*-cycloidal magnetic order exists in films of $YMnO_3$, in opposition to the E-type displayed in bulk, and it can be switched to *ac*-cycloid by a magnetic field applied along the *c*-axis.

We have observed that the dependence of measured polarization of o-$YMnO_3$ on magnetic field is hysteretic. We have explained this result presenting a plausible scenario where cycloidal domains of different chiralities compete between them in a similar way to magnetic domains in ferromagnets. In this context, we have shown that, in the absence of previous electrical poling, chiral domains are randomly formed. However, once poling has been used to create a single domain chiral state, after subsequent magnetic field induced flopping, chiral order is (partially 2/3) preserved, thus keeping memory of its initial poling direction.

Ferroelectricity and the dielectric permittivity dependency on magnetic field of orthorhombic *a*- and *c*-oriented thin films has been explored as a function of thickness, a/b lattice parameters ratio and ferromagnetic character of the films. It has been observed that increasing in-plane compressive strain the ferroelectric polarization gradually disappears and a net magnetic moment emerges. It is argued that these observations are signatures of the progressive destabilization of the cycloid antiferromagnetic structure in benefit of a canted A-type magnetic structure.

Ferroelectric nature of horizontal and vertical $BaTiO_3$-$CoFe_2O_4$ composite materials has been also observed. In horizontal structures, it is noticeable that $BaTiO_3$ preserves its ferroelectric character even when growing on $CoFe_2O_4$, thus overcoming the difficulties due to the dissimilar structure of both phases. In vertical structures, it is interesting to note that ferroelectric behavior, already reported in similar composites grown by PLD, is preserved when using rf magnetron sputtering growing technique.

Magnetodielectric response in both composite architectures has also been measured. In $BaTiO_3$-$CoFe_2O_4$ vertical nanocomposites low magnetodielectric effect (up to 2 % under 9 T at room temperature) has been found. Here, data do not permit to firmly conclude that the observed magnetodielectric response is genuine and consequence of the magnetoelectric coupling between $BaTiO_3$ and $CoFe_2O_4$ but may result from the magnetoresitance contribution

Summary of obtained experimental results in the present thesis.

System	P control by H	Magneto-dielectric coefficient (%/T)	Working temperature
Single-phase o-$YMnO_3$	✓	-0.9	5 K
Horizontal $BaTiO_3$-$CoFe_2O_4$	Further work	4	Fridge Temperature
Vertical $BaTiO_3$-$CoFe_2O_4$	X	0.2	RT

of $CoFe_2O_4$. In opposition, in horizontal heterostructures, magnetoelectric coupling has been revealed to be present, large and intrinsic (magnetodielectric response up to 36 % under 9 T near room temperature). The large magnetoelectric effect has been demonstrated to be favoured when the substrate clamping effect is released.

It has been shown that epitaxial strain determines the dielectric/ferroelectric properties in both architectures. Whereas in vertical structures strain, modified by growth conditions, can control the dielectric permittivity ($\epsilon \approx$ 20-80), in horizontal structures suitable election of thicknesses and ratios of $BaTiO_3$ and $CoFe_2O_4$ can determine the final ferroelectric properties (with polarization values even larger than in bulk, up to 50 $\mu C/cm^2$).

To sum up, we have achieved the control of ferroelectric polarization by magnetic field in single-phase multiferroic o-$YMnO_3$ at low temperature, while, in horizontal composites multiferroicity and large magnetodielectric effect near room temperature have been measured, pointing to the possibility of controlling polarization by magnetic field near room temperature. Leakage in vertical composites appears to be a handicap for exploiting magnetoelectric

coupling.

The results obtained in the present thesis (summarized in the summary table) show that both classes of materials can lead to the control of sizable amount of charge by magnetic field near room temperature.

Bibliography

[1] T. Lottermoser, T. Lonkai, U. Amann, D. Hohlwein, J. Ihringer, and M. Fiebig, *Magnetic phase control by an electric field*, Nature **430**, 541 (2004).

[2] T. Kimura, T. Goto, H. Shintani, K. Ishizaka, T. Arima, and Y. Tokura, *Magnetic control of ferroelectric polarization*, Nature **426**, 55 (2003).

[3] V. Wood and A. Austin, *Possible applications for magnetoelectric materials*, International Journal of Magnetism **5**, 303 (1974).

[4] R. Thomas, J. F. Scott, D. N. Bose, and R. S. Katiyar, *Multiferroic thin-film integration onto semiconductor devices*, Journal of Physics: Condensed Matter **22**, 423201 (2010).

[5] J. Maxwell, *A Treatise on Electricity And Magnetism*, Posner Memorial Collection, Vol. 1 (Carnegie Mellon University, 1873).

[6] J. Maxwell, *A Treatise on Electricity And Magnetism*, Posner Memorial Collection, Vol. 2 (Carnegie Mellon University, 1873).

[7] P. Curie, *On the symmetry of the physics phenomena, symmetry of and electric and magnetic field*, J. Physique **3**, 393 (1894).

[8] P. Debye, *Bemerkung zu einigen Versuchen über einen magneto-elektrischen Richteffekt*, Z. Phys. **36**, 300 (1926).

[9] I. Dzyaloshinskii, *K voprosu o magnitno-elektricheskom effekte v antiferromagnetikakh (On the magneto-electrical effect in antiferromagnets)*, Sov. Phys. JETP **10**, 628 (1959).

[10] D. Astrov, *The magnetoelectric effect in antiferromagnetics*, Sov. Phys. JETP **11**, 708 (1960).

[11] E. Ascher, H. Rieder, H. Schmid, and H. Stössel, *Some Properties of Ferromagnetoelectric Nickel-Iodine Boracite, $Ni_3B_7O_{13}I$*, Journal of

Applied Physics **37**, 1404 (1966).

[12] H. Schmid, *Multi-ferroic magnetoelectrics*, Ferroelectrics **162**, 317 (1994).

[13] N. A. Hill, *Why Are There so Few Magnetic Ferroelectrics?*, The Journal of Physical Chemistry B **104**, 6694 (2000).

[14] J. Wang, J. B. Neaton, H. Zheng, V. Nagarajan, S. B. Ogale, B. Liu, D. Viehland, V. Vaithyanathan, D. G. Schlom, U. V. Waghmare, N. A. Spaldin, K. M. Rabe, M. Wuttig, and R. Ramesh, *Epitaxial $BiFeO_3$ Multiferroic Thin Film Heterostructures*, Science **299**, 1719 (2003).

[15] H. Zheng, J. Wang, S. E. Lofland, Z. Ma, L. Mohaddes-Ardabili, T. Zhao, L. Salamanca-Riba, S. R. Shinde, S. B. Ogale, F. Bai, D. Viehland, Y. Jia, D. G. Schlom, M. Wuttig, A. Roytburd, and R. Ramesh, *Multiferroic $BaTiO_3$-$CoFe_2O_4$ Nanostructures*, Science **303**, 661 (2004).

[16] M. Fiebig, *Revival of the magnetoelectric effect*, Journal of Physics D: Applied Physics **38**, R123 (2005).

[17] W. Eerenstein, N. D. Mathur, and J. F. Scott, *Multiferroic and magnetoelectric materials*, Nature **442**, 759 (2006).

[18] D. I. Khomskii, *Multiferroics: Different ways to combine magnetism and ferroelectricity*, Journal of Magnetism and Magnetic Materials **306**, 1 (2006).

[19] S.-W. Cheong and M. Mostovoy, *Multiferroics: a magnetic twist for ferroelectricity*, Nature Materials **6**, 13 (2007).

[20] J. P. Velev, S. S. Jaswal, and E. Y. Tsymbal, *Multi-ferroic and magnetoelectric materials and interfaces*, Philosophical Transactions of the Royal Society A: Mathematical,Physical and Engineering Sciences **369**, 3069 (2011).

[21] W. Prellier, M. Singh, and P. Murugavel, *The single-phase multiferroic oxides: from bulk to thin film*, Journal of Physics: Condensed Matter **17**, R803 (2005).

[22] Y. Tokura and N. Kida, *Dynamical magnetoelectric effects in multiferroic oxides*, Philosophical Transactions of the Royal Society A: Mathematical,Physical and Engineering Sciences **369**, 3679 (2011).

[23] G. Lawes and G. Srinivasan, *Introduction to magnetoelectric coupling and multiferroic films*, Journal of Physics D: Applied Physics **44**, 243001

(2011).

[24] D. Khomskii, *Classifying multiferroics: Mechanisms and effects*, Physics **2**, 20 (2009).

[25] M. Sakai, A. Masuno, D. Kan, M. Hashisaka, K. Takata, M. Azuma, M. Takano, and Y. Shimakawa, *Multiferroic thin film of Bi_2NiMnO_6 with ordered double-perovskite structure*, Applied Physics Letters **90**, 072903 (2007).

[26] E. Langenberg, M. Varela, M. García-Cuenca, C. Ferrater, M. Polo, I. Fina, L. Fàbrega, F. Sánchez, and J. Fontcuberta, *Epitaxial thin films of $(Bi_{0.9}La_{0.1})_2NiMnO_6$ obtained by pulsed laser deposition*, Journal of Magnetism and Magnetic Materials **321**, 1748 (2009).

[27] E. Langenberg, J. Rebled, S. Estradé, C. J. M. Daumont, J. Ventura, L. E. Coy, M. C. Polo, M. V. García-Cuenca, C. Ferrater, B. Noheda, F. F. Peiró, M. Varela, and J. Fontcuberta, *Long-range order of Ni^2+ and Mn^{4+} and ferromagnetism in multiferroic $(Bi_{0.9}La_{0.1})_2NiMnO_6$ thin films*, Journal of Applied Physics **108**, 123907 (2010).

[28] E. Langenberg, I. Fina, P. Gemeiner, B. Dkhil, L. Fàbrega, M. Varela, and J. Fontcuberta, *Ferroelectric phase transition in strained multiferroic $(Bi_{0.9}La_{0.1})_2NiMnO_6$ thin films*, Applied Physics Letters **100**, 022902 (2012).

[29] J. Efremov, Dmitry V. and-van den Brink and D. I. Khomskii, *Bond-versus site-centred ordering and possible ferroelectricity in manganites*, Nature Materials **3**, 853 (2004).

[30] N. Hur, S. Park, P. A. Sharma, J. S. Ahn, S. Guha, and S.-W. Cheong, *Electric polarization reversal and memory in a multiferroic material induced by magnetic fields*, Nature **429**, 392 (2004).

[31] B. B. Van Aken, T. Palstra, A. Filippetti, and N. Spaldin, *The origin of ferroelectricity in magnetoelectric $YMnO_3$*, Nature Materials **3**, 164 (2004).

[32] E. Bertaut, F. Forrat, and P. Fang., *Les manganittes de terres rares et d'yttrium: une nouvelle classe de ferroélectriques*, Académie des Sciences Paris **256**, 1958 (1963).

[33] Y. J. Choi, H. T. Yi, S. Lee, Q. Huang, V. Kiryukhin, and S.-W. Cheong, *Ferroelectricity in an Ising Chain Magnet*, Phys. Rev. Lett.

100, 047601 (2008).

[34] I. A. Sergienko, C. Şen, and E. Dagotto, *Ferroelectricity in the Magnetic E-Phase of Orthorhombic Perovskites*, Phys. Rev. Lett. **97**, 227204 (2006).

[35] N. Lee, Y. J. Choi, M. Ramazanoglu, W. Ratcliff, V. Kiryukhin, and S.-W. Cheong, *Mechanism of exchange striction of ferroelectricity in multiferroic orthorhombic $HoMnO_3$ single crystals*, Phys. Rev. B **84**, 020101 (2011).

[36] N. Izyumskaya, Y. Alivov, and H. Morkoç, *Oxides, Oxides, and More Oxides: High-k Oxides, Ferroelectrics, Ferromagnetics, and Multiferroics*, Critical Reviews in Solid State and Materials Sciences **34**, 89 (2009).

[37] J. Ma, J. Hu, Z. Li, and C.-W. Nan, *Recent Progress in Multiferroic Magnetoelectric Composites: from Bulk to Thin Films*, Advanced Materials **23**, 1062 (2011).

[38] L. W. Martin, S. P. Crane, Y.-H. Chu, M. B. Holcomb, M. Gajek, M. Huijben, C.-H. Yang, N. Balke, and R. Ramesh, *Multiferroics and magnetoelectrics: thin films and nanostructures*, Journal of Physics: Condensed Matter **20**, 434220 (2008).

[39] C.-W. Nan, M. I. Bichurin, S. Dong, D. Viehland, and G. Srinivasan, *Multiferroic magnetoelectric composites: Historical perspective, status, and future directions*, Journal of Applied Physics **103**, 031101 (2008).

[40] G. Srinivasan, *Magnetoelectric Composites*, Annual Review of Materials Research **40**, 153 (2010).

[41] J. Zhai, Z. Xing, S. Dong, J. Li, and D. Viehland, *Magnetoelectric Laminate Composites: An Overview*, Journal of the American Ceramic Society **91**, 351 (2008).

[42] L. Martin, Y.-H. Chu, and R. Ramesh, *Advances in the growth and characterization of magnetic, ferroelectric, and multiferroic oxide thin films*, Materials Science and Engineering: R: Reports **68**, 89 (2010).

[43] L. Yan, Y. Yang, Z. Wang, Z. Xing, J. Li, and D. Viehland, *Review of magnetoelectric perovskite-spinel self-assembled nano-composite thin films*, Journal of Materials Science **44**, 5080 (2009).

[44] J. van Suchtelen, *Product properties: a new application of composite*

materials, Philips Research Reports **27**, 28 (1972).

[45] W. Eerenstein, M. Wiora, J. L. Prieto, J. F. Scott, and N. D. Mathur, *Giant sharp and persistent converse magnetoelectric effects in multiferroic epitaxial heterostructures*, Nature Materials **6**, 348 (2007).

[46] S. Dong, J. Zhai, F. Bai, J.-F. Li, and D. Viehland, *Push-pull mode magnetostrictive/piezoelectric laminate composite with an enhanced magnetoelectric voltage coefficient*, Applied Physics Letters **87**, 062502 (2005).

[47] H. J. A. Molegraaf, J. Hoffman, C. A. F. Vaz, S. Gariglio, D. van der Marel, C. H. Ahn, and J.-M. Triscone, *Magnetoelectric Effects in Complex Oxides with Competing Ground States*, Advanced Materials **21**, 3470 (2009).

[48] M. Fiebig, T. Lottermoser, D. Frohlich, A. V. Goltsev, and R. V. Pisarev, *Observation of coupled magnetic and electric domains*, Nature **419**, 818 (2002).

[49] V. Laukhin, V. Skumryev, X. Martí, D. Hrabovsky, F. Sánchez, M. V. García-Cuenca, C. Ferrater, M. Varela, U. Lüders, J. F. Bobo, and J. Fontcuberta, *Electric-Field Control of Exchange Bias in Multiferroic Epitaxial Heterostructures*, Phys. Rev. Lett. **97**, 227201 (2006).

[50] V. Skumryev, V. Laukhin, I. Fina, X. Martí, F. Sánchez, M. Gospodinov, and J. Fontcuberta, *Magnetization Reversal by Electric-Field Decoupling of Magnetic and Ferroelectric Domain Walls in Multiferroic-Based Heterostructures*, Phys. Rev. Lett. **106**, 057206 (2011).

[51] V. Garcia, M. Bibes, L. Bocher, S. Valencia, F. Kronast, A. Crassous, X. Moya, S. Enouz-Vedrenne, A. Gloter, D. Imhoff, C. Deranlot, N. D. Mathur, S. Fusil, K. Bouzehouane, and A. Barthélémy, *Ferroelectric Control of Spin Polarization*, Science **327**, 1106 (2010).

[52] H.-C. He, J. Wang, J.-P. Zhou, and C.-W. Nan, *Ferroelectric and Ferromagnetic Behavior of $Pb(Zr_{0.52}Ti_{0.48})O_3$-$Co_{0.9}Zn_{0.1}Fe_2O_4$ Multilayered Thin Films Prepared via Solution Processing*, Advanced Functional Materials **17**, 1333 (2007).

[53] C. Thiele, K. Dörr, S. Fähler, L. Schultz, D. C. Meyer, A. A. Levin, and P. Paufler, *Voltage-controlled epitaxial strain in $La_{0.7}Sr_{0.3}MnO_3/Pb(Mg_{1/3}Nb_{2/3})O_3$-$PbTiO_3$ (001) films*, Applied Physics Letters **87**, 262502 (2005).

[54] H. Ryu, P. Murugavel, J. H. Lee, S. C. Chae, T. W. Noh, Y. S. Oh, H. J. Kim, K. H. Kim, J. H. Jang, M. Kim, C. Bae, and J.-G. Park, *Magnetoelectric effects of nanoparticulate $Pb(Zr_{0.52}Ti_{0.48})O_3$-$NiFe_2O_4$ composite films*, Applied Physics Letters **89**, 102907 (2006).

[55] N. Ortega, P. Bhattacharya, R. S. Katiyar, P. Dutta, A. Manivannan, M. S. Seehra, I. Takeuchi, and S. B. Majumder, *Multiferroic properties of $Pb(Zr,Ti)O_3/CoFe_2O_4$ composite thin films*, Journal of Applied Physics **100**, 126105 (2006).

[56] J. G. Wan, X. W. Wang, Y. J. Wu, M. Zeng, Y. Wang, H. Jiang, W. Q. Zhou, G. H. Wang, and J.-M. Liu, *Magnetoelectric $CoFe_2O_4$-$Pb(Zr,Ti)O_3$ composite thin films derived by a sol-gel process*, Applied Physics Letters **86**, 122501 (2005).

[57] J. Ma, Z. Shi, and C.-W. Nan, *Magnetoelectric Properties of Composites of Single $Pb(Zr,Ti)O_3$ Rods and Terfenol-D/Epoxy with a Single-Period of 1-3-Type Structure*, Advanced Materials **19**, 2571 (2007).

[58] Z. Shi, C. W. Nan, J. Zhang, N. Cai, and J.-F. Li, *Magnetoelectric effect of $Pb(Zr,Ti)O_3$ rod arrays in a $(Tb,Dy)Fe_2$/epoxy medium*, Applied Physics Letters **87**, 012503 (2005).

[59] Z. Shi, C.-W. Nan, J. Zhang, J. Ma, and J.-F. Li, *Magnetoelectric properties of multiferroic composites with pseudo-1-3-journal article structure*, Journal of Applied Physics **99**, 124108 (2006).

[60] V. Corral-Flores, D. Bueno-Baques, D. Carrillo-Flores, and J. A. Matutes-Aquino, *Enhanced magnetoelectric effect in core-shell particulate composites*, Journal of Applied Physics **99**, 08J503 (2006).

[61] D. Okuyama, S. Ishiwata, Y. Takahashi, K. Yamauchi, S. Picozzi, K. Sugimoto, H. Sakai, M. Takata, R. Shimano, Y. Taguchi, T. Arima, and Y. Tokura, *Magnetically driven ferroelectric atomic displacements in orthorhombic $YMnO_3$*, Phys. Rev. B **84**, 054440 (2011).

[62] X. Martí, *Growth and characterization of magnetoelectric $YMnO_3$ epitaxial thin films*, Ph.D. thesis, Universitat Autònoma de Barcelona (2009).

[63] X. Martí, V. Skumryev, V. Laukhin, R. Bachelet, C. Ferrater, M. V. García-Cuenca, M. Varela, F. Sánchez, and J. Fontcuberta, *Strain-driven noncollinear magnetic ordering in orthorhombic epitaxial $YMnO_3$ thin films*, Journal of Applied Physics **108**, 123917 (2010).

[64] C. Deng, Y. Zhang, J. Ma, Y. Lin, and C.-W. Nan, *Magnetic-electric properties of epitaxial multiferroic $NiFe_2O_4$-$BaTiO_3$ heterostructure*, Journal of Applied Physics **102**, 074114 (2007).

[65] H.-C. He, J.-P. Zhou, J. Wang, and C.-W. Nan, *Multiferroic $Pb(Zr_{0.53}Ti_{0.48})O_3$-$Co_{0.9}Zn_{0.1}Fe_2O_4$ bilayer thin films via a solution processing*, Applied Physics Letters **89**, 052904 (2006).

[66] F. Zavaliche, T. Zhao, H. Zheng, F. Straub, M. P. Cruz, P.-L. Yang, D. Hao, and R. Ramesh, *Electrically Assisted Magnetic Recording in Multiferroic Nanostructures*, Nano Letters **7**, 1586 (2007).

[67] F. Zavaliche, H. Zheng, L. Mohaddes-Ardabili, S. Y. Yang, Q. Zhan, P. Shafer, E. Reilly, R. Chopdekar, Y. Jia, P. Wright, D. G. Schlom, Y. Suzuki, and R. Ramesh, *Electric Field-Induced Magnetization Switching in Epitaxial Columnar Nanostructures*, Nano Letters **5**, 1793 (2005).

[68] M. Zgonik, P. Bernasconi, M. Duelli, R. Schlesser, P. Günter, M. H. Garrett, D. Rytz, Y. Zhu, and X. Wu, *Dielectric, elastic, piezoelectric, electro-optic, and elasto-optic tensors of* $BaTiO_3$ *crystals*, Phys. Rev. B **50**, 5941 (1994).

[69] R. M. Bozorth, E. F. Tilden, and A. J. Williams, *Anisotropy and Magnetostriction of Some Ferrites*, Phys. Rev. **99**, 1788 (1955).

[70] N. Dix, Ph.D. thesis, Universitat Autònoma de Barcelona (2012).

[71] M. Lines and A. Glass, *Principles and applications of ferroelectrics and related materials* (Oxford Classsic Texts in the Ohysical Science, 2001).

[72] A. V. Hippel, *Dielectric and Waves* (Wiley, 1981).

[73] L. Pintilie, I. Vrejoiu, D. Hesse, and M. Alexe, *The influence of the top-contact metal on the ferroelectric properties of epitaxial ferroelectric $Pb(Zr_{0.2}Ti_{0.8})O_3$ thin films*, Journal of Applied Physics **104**, 114101 (2008).

[74] Agilent, *Agilent Impedance Measurement Handbook*, edited by I. Agilent Technologies (Agilent Technologies, Inc., 2009).

[75] M. Dawber, K. M. Rabe, and J. F. Scott, *Physics of thin-film ferroelectric oxides*, Rev. Mod. Phys. **77**, 1083 (2005).

[76] G. Catalan, D. O'Neill, R. M. Bowman, and J. M. Gregg, *Relaxor features in ferroelectric superlattices: A Maxwell-Wagner approach*, Applied Physics Letters **77**, 3078 (2000).

[77] A. K. Jonscher, *Dielectric Relaxation in Solids* (Chelsea Dielectrics Press Ltd, 1983).

[78] J. R. Macdonald and W. R. Kenan, *Impedance Spectroscopy: Emphasizing Solid Materials and Systems*, edited by J. R. Macdonald (Wiley-Interscience, 1987).

[79] R. Schmidt, W. Eerenstein, T. Winiecki, F. D. Morrison, and P. A. Midgley, *Impedance spectroscopy of epitaxial multiferroic thin films*, Phys. Rev. B **75**, 245111 (2007).

[80] S. Song and F. Placido, *The influence of phase probability distributions on impedance spectroscopy*, Journal of Statistical Mechanics: Theory and Experiment **2004**, P10018 (2004).

[81] G. Catalan, *Magnetocapacitance without magnetoelectric coupling*, Applied Physics Letters **88**, 102902 (2006).

[82] J. T. S. Irvine, D. C. Sinclair, and A. R. West, *Electroceramics: Characterization by Impedance Spectroscopy*, Advanced Materials **2**, 132 (1990).

[83] Scribner, *http://www.scribner.com*.

[84] J. F. Scott, *Ferroelectrics go bananas*, Journal of Physics: Condensed Matter **20**, 021001 (2008).

[85] C. B. Sawyer and C. H. Tower, *Rochelle Salt as a Dielectric*, Phys. Rev. **35**, 269 (1930).

[86] Aixacct, *TF Analyzer 2000 Hysteresis Software Version 2.1.* (2000).

[87] S. L. Miller, R. D. Nasby, J. R. Schwank, M. S. Rodgers, and P. V. Dressendorfer, *Device modeling of ferroelectric capacitors*, Journal of Applied Physics **68**, 6463 (1990).

[88] L. Pintilie and M. Alexe, *Metal-ferroelectric-metal heterostructures with Schottky contacts. I. Influence of the ferroelectric properties*, Journal of Applied Physics **98**, 124103 (2005).

[89] L. Pintilie, I. Boerasu, M. J. M. Gomes, T. Zhao, R. Ramesh, and M. Alexe, *Metal-ferroelectric-metal structures with Schottky contacts. II. Analysis of the experimental current-voltage and capacitance-voltage characteristics of Pb(Zr,Ti)O_3 thin films*, Journal of Applied Physics **98**, 124104 (2005).

[90] P. Zubko, D. J. Jung, and J. F. Scott, *Electrical characterization*

of $PbZr_{0.4}Ti_{0.6}O_3$ capacitors, Journal of Applied Physics **100**, 114113 (2006).

[91] O. Lohse, M. Grossmann, U. Boettger, D. Bolten, and R. Waser, *Relaxation mechanism of ferroelectric switching in $Pb(Zr,Ti)O_3$ thin films*, Journal of Applied Physics **89**, 2332 (2001).

[92] P. A. Tipler and G. Mosca, *Physics for Scientists and Engineers*, Vol. Volume 2 Electricity and Magnetism/Light (W. H. Freeman, 2007).

[93] I. Fina, L. Fàbrega, E. Langenberg, X. Martí, F. Sánchez, M. Varela, and J. Fontcuberta, *Non-ferroelectric contributions to the hysteresis cycles in manganite thin films: A comparative study of measurement techniques*, Journal of Applied Physics **109**, 074105 (2011).

[94] R. Meyer, R. Waser, K. Prume, T. Schmitz, and S. Tiedke, *Dynamic leakage current compensation in ferroelectric thin-film capacitor structures*, Applied Physics Letters **86**, 142907 (2005).

[95] J. F. Scott, L. Kammerdiner, M. Parris, S. Traynor, V. Ottenbacher, A. Shawabkeh, and W. F. Oliver, *Switching kinetics of lead zirconate titanate submicron thin film memories*, Journal of Applied Physics **64**, 787 (1988).

[96] L. Pintilie and M. Alexe, *Ferroelectric-like hysteresis loop in nonferroelectric systems*, Applied Physics Letters **87**, 112903 (2005).

[97] I. Rivera, A. Kumar, N. Ortega, R. Katiyar, and S. Lushnikov, *Divide line between relaxor, diffused ferroelectric, ferroelectric and dielectric*, Solid State Communications **149**, 172 (2009).

[98] O. G. Vendik and S. P. Zubko, *Ferroelectric phase transition and maximum dielectric permittivity of displacement article ferroelectrics ($Ba_xSr_{1-x}TiO_3$)*, Journal of Applied Physics **88**, 5343 (2000).

[99] V. G. Chepurenko, *Pyroelectric effect in ceramic ferroelectrics*, Russian Physics Journal **9**, 29 (1966).

[100] I. Fina, N. Dix, L. Fàbrega, F. Sánchez, and J. Fontcuberta, *Magnetocapacitance in $BaTiO_3$-$CoFe_2O_4$ nanocomposites*, Thin Solid Films **518**, 4634 (2010), proceedings of the EMRS 2009 Spring Meeting Symposium H: Synthesis, Processing and Characterization of Nanoscale Multi Functional Oxide Films II.

[101] J. Hemberger, P. Lunkenheimer, R. Fichtl, H.-A. Krug von Nidda,

V. Tsurkan, and A. Loidl, *Relaxor ferroelectricity and colossal magnetocapacitive coupling in ferromagnetic $CdCr_2S_4$*, Nature **434**, 364 (2005).

[102] G. Catalan and J. F. Scott, *Magnetoelectrics: Is $CdCr_2S_4$ a multiferroic relaxor?*, Nature **448**, E4 (2007).

[103] J. Hemberger, P. Lunkenheimer, R. Fichtl, H.-A. K. von Nidda, V. Tsurkan, and A. Loidl, *Magnetoelectrics: Is $CdCr_2S_4$ a multiferroic relaxor? (reply)*, Nature **448**, E5 (2007).

[104] J. A. Alonso, M. J. Martínez-Lope, M. T. Casais, and M. T. Fernández-Díaz, *Evolution of the Jahn-Teller Distortion of MnO_6 Octahedra in $RMnO_3$ Perovskites (R = Pr, Nd, Dy, Tb, Ho, Er, Y): A Neutron Diffraction Study*, Inorganic Chemistry **39**, 917 (2000).

[105] B. Lorenz, Y. Q. Wang, Y. Y. Sun, and C. W. Chu, *Large magnetodielectric effects in orthorhombic $HoMnO_3$ and $YMn\ O_3$*, Phys. Rev. B **70**, 212412 (2004).

[106] B. Lorenz, Y.-Q. Wang, and C.-W. Chu, *Ferroelectricity in perovskite $HoMnO_3$ and $YMn\ O_3$*, Phys. Rev. B **76**, 104405 (2007).

[107] N. Hur, I. K. Jeong, M. F. Hundley, S. B. Kim, and S.-W. Cheong, *Giant magnetoelectric effect in multiferroic $HoMnO_3$ with a high ferroelectric transition temperature*, Phys. Rev. B **79**, 134120 (2009).

[108] M. Kenzelmann, A. B. Harris, S. Jonas, C. Broholm, J. Schefer, S. B. Kim, C. L. Zhang, S.-W. Cheong, O. P. Vajk, and J. W. Lynn, *Magnetic Inversion Symmetry Breaking and Ferroelectricity in $TbMnO_3$*, Phys. Rev. Lett. **95**, 087206 (2005).

[109] H. Katsura, N. Nagaosa, and A. V. Balatsky, *Spin Current and Magnetoelectric Effect in Noncollinear Magnets*, Phys. Rev. Lett. **95**, 057205 (2005).

[110] T. Kimura, *Spiral Magnets as Magnetoelectrics*, Annual Review of Materials Research **37**, 387 (2007).

[111] Y. Tokura and S. Seki, *Multiferroics with Spiral Spin Orders*, Advanced Materials **22**, 1554 (2010).

[112] I. A. Sergienko and E. Dagotto, *Role of the Dzyaloshinskii-Moriya interaction in multiferroic perovskites*, Phys. Rev. B **73**, 094434 (2006).

[113] I. Dzyaloshinsky, *A thermodynamic theory of "weak" ferromagnetism of*

antiferromagnetics, Journal of Physics and Chemistry of Solids **4**, 241 (1958).

[114] T. Moriya, *Anisotropic Superexchange Interaction and Weak Ferromagnetism*, Phys. Rev. **120**, 91 (1960).

[115] T. Kimura, G. Lawes, T. Goto, Y. Tokura, and A. P. Ramirez, *Magnetoelectric phase diagrams of orthorhombic R MnO_2 (R = Gd , Tb, and Dy)*, Phys. Rev. B **71**, 224425 (2005).

[116] S. Ishiwata, Y. Kaneko, Y. Tokunaga, Y. Taguchi, T.-h. Arima, and Y. Tokura, *Perovskite manganites hosting versatile multiferroic phases with symmetric and antisymmetric exchange strictions*, Phys. Rev. B **81**, 100411 (2010).

[117] M. Mostovoy, *Ferroelectricity in Spiral Magnets*, Phys. Rev. Lett. **96**, 067601 (2006).

[118] D. O'Flynn, C. V. Tomy, M. R. Lees, A. Daoud-Aladine, and G. Balakrishnan, *Multiferroic properties and magnetic structure of* $Sm_{1-x}Y_xMnO_3$, Phys. Rev. B **83**, 174426 (2011).

[119] H. Murakawa, Y. Onose, F. Kagawa, S. Ishiwata, Y. Kaneko, and Y. Tokura, *Rotation of an Electric Polarization Vector by Rotating Magnetic Field in Cycloidal Magnet $Eu_{0.55}Y_{0.45}MnO_3$*, Phys. Rev. Lett. **101**, 197207 (2008).

[120] T. Goto, T. Kimura, G. Lawes, A. P. Ramirez, and Y. Tokura, *Ferroelectricity and Giant Magnetocapacitance in Perovskite Rare-Earth Manganites*, Phys. Rev. Lett. **92**, 257201 (2004).

[121] M. Mochizuki and N. Furukawa, *Theory of Magnetic Switching of Ferroelectricity in Spiral Magnets*, Phys. Rev. Lett. **105**, 187601 (2010).

[122] S. Quezel, J. Rossat-Mignod, and E. F. Bertaut, *Magnetic Structure of rare earth orthomanganites - 1. $YMnO_3$*, Solid State Communications **14**, 941 (1974).

[123] A. Muñoz, J. A. Alonso, M. T. Casais, M. J. Martínez-Lope, J. L. Martínez, and M. T. Fernández-Díaz, *The magnetic structure of $YMnO_3$ perovskite revisited*, Journal of Physics: Condensed Matter **14**, 3285 (2002).

[124] H. Wadati, J. Okamoto, M. Garganourakis, V. Scagnoli, U. Staub, Y. Yamasaki, H. Nakao, Y. Murakami, M. Mochizuki, M. Nakamura,

M. Kawasaki, and Y. Tokura, *Origin of the Large Polarization in Multiferroic* $YMnO_3$ *Thin Films Revealed by Soft- and Hard-X-Ray Diffraction*, Phys. Rev. Lett. **108**, 047203 (2012).

[125] J. Hemberger, F. Schrettle, A. Pimenov, P. Lunkenheimer, V. Y. Ivanov, A. A. Mukhin, A. M. Balbashov, and A. Loidl, *Multiferroic phases of* $Eu_{(1-x)}Y_xMnO_3$, Phys. Rev. B **75**, 035118 (2007).

[126] Y. Yamasaki, H. Sagayama, N. Abe, T. Arima, K. Sasai, M. Matsuura, K. Hirota, D. Okuyama, Y. Noda, and Y. Tokura, *Cycloidal Spin Order in the a-Axis Polarized Ferroelectric Phase of Orthorhombic Perovskite Manganite*, Phys. Rev. Lett. **101**, 097204 (2008).

[127] T. H. Lin, C. C. Hsieh, C. W. Luo, J.-Y. Lin, C. P. Sun, H. D. Yang, C.-H. Hsu, Y. H. Chu, K. H. Wu, T. M. Uen, and J. Y. Juang, *Magnetism-induced ferroelectric polarization in the c-axis-oriented orthorhombic* $HoMnO_3$ *thin films*, Journal of Applied Physics **106**, 103923 (2009).

[128] T. H. Lin, H. C. Shih, C. C. Hsieh, C. W. Luo, J.-Y. Lin, J. L. Her, H. D. Yang, C.-H. Hsu, K. H. Wu, T. M. Uen, and J. Y. Juang, *Strain-induced effects on antiferromagnetic ordering and magnetocapacitance in orthorhombic* $HoMnO_3$ *thin films*, Journal of Physics: Condensed Matter **21**, 026013 (2009).

[129] T. C. Han and J. G. Lin, *Strong coupling of magnetic and dielectric properties in the a-axis-oriented orthorhombic* $HoMnO_3$ *films*, Applied Physics Letters **94**, 082502 (2009).

[130] C. J. M. Daumont, D. Mannix, S. Venkatesan, G. Catalan, D. Rubi, B. J. Kooi, J. T. M. D. Hosson, and B. Noheda, *Epitaxial* $TbMnO_3$ *thin films on* $SrTiO_3$ *substrates: a structural study*, Journal of Physics: Condensed Matter **21**, 182001 (2009).

[131] B. J. Kirby, D. Kan, A. Luykx, M. Murakami, D. Kundaliya, and I. Takeuchi, *Anomalous ferromagnetism in* $TbMnO_3$ *thin films*, Journal of Applied Physics **105**, 07D917 (2009).

[132] D. Rubi, C. de Graaf, C. J. M. Daumont, D. Mannix, R. Broer, and B. Noheda, *Ferromagnetism and increased ionicity in epitaxially grown* $TbMnO_3$ *films*, Phys. Rev. B **79**, 014416 (2009).

[133] D. Rubi, S. Venkatesan, B. J. Kooi, J. T. M. De Hosson, T. T. M. Palstra, and B. Noheda, *Magnetic and dielectric properties of* $YbMnO_3$ *perovskite thin films*, Phys. Rev. B **78**, 020408 (2008).

[134] F. Bai, J. Wang, M. Wuttig, J. Li, N. Wang, A. P. Pyatakov, A. K. Zvezdin, L. E. Cross, and D. Viehland, *Destruction of spin cycloid in $(111)_c$-oriented $BiFeO_3$ thin films by epitiaxial constraint: Enhanced polarization and release of latent magnetization*, Applied Physics Letters **86**, 032511 (2005).

[135] X. Martí, F. Sánchez, V. Skumryev, V. Laukhin, C. Ferrater, M. García-Cuenca, M. Varela, and J. Fontcuberta, *Crystal texture selection in epitaxies of orthorhombic antiferromagnetic $YMnO_3$ films*, Thin Solid Films **516**, 4899 (2008).

[136] J. Fontcuberta, I. Fina, L. Fàbrega, F. Sánchez, X. Martí, and V. Skumryev, *Ferroelectricity and strain effects in orthorhombic $YMnO_3$ thin films*, Phase Transitions **84**, 555 (2011).

[137] S. Picozzi, K. Yamauchi, B. Sanyal, I. A. Sergienko, and E. Dagotto, *Dual Nature of Improper Ferroelectricity in a Magnetoelectric Multiferroic*, Phys. Rev. Lett. **99**, 227201 (2007).

[138] K. Yamauchi, F. Freimuth, S. Blügel, and S. Picozzi, *Magnetically induced ferroelectricity in orthorhombic manganites: Microscopic origin and chemical trends*, Phys. Rev. B **78**, 014403 (2008).

[139] N. Abe, K. Taniguchi, S. Ohtani, H. Umetsu, and T. Arima, *Control of the polarization flop direction by a tilted magnetic field in multiferroic $TbMnO_3$*, Phys. Rev. B **80**, 020402 (2009).

[140] K. Taniguchi, N. Abe, H. Umetsu, H. A. Katori, and T. Arima, *Control of the Magnetoelectric Domain-Wall Stability by a Magnetic Field in a Multiferroic* $MnWO_4$, Phys. Rev. Lett. **101**, 207205 (2008).

[141] F. Kagawa, M. Mochizuki, Y. Onose, H. Murakawa, Y. Kaneko, N. Furukawa, and Y. Tokura, *Dynamics of Multiferroic Domain Wall in Spin-Cycloidal Ferroelectric $DyMnO3$*, Phys. Rev. Lett. **102**, 057604 (2009).

[142] F. Schrettle, P. Lunkenheimer, J. Hemberger, V. Y. Ivanov, A. A. Mukhin, A. M. Balbashov, and A. Loidl, *Relaxations as Key to the Magnetocapacitive Effects in the Perovskite Manganites*, Phys. Rev. Lett. **102**, 207208 (2009).

[143] J. F. Scott, *Data storage: Multiferroic memories*, Nature Materials **6**, 256 (2007).

[144] N. Abe, K. Taniguchi, H. Sagayama, H. Umetsu, and T. Arima, *Correlation between the mobility of domain wall and polarization flop direction in a slanted magnetic field in the helimagnetic ferroelectrics* $Tb_{1-x}Dy_xMnO_3$, Phys. Rev. B **83**, 060403 (2011).

[145] M. Mochizuki and N. Nagaosa, *Theoretically Predicted Picosecond Optical Switching of Spin Chirality in Multiferroics*, Phys. Rev. Lett. **105**, 147202 (2010).

[146] N. Abe, K. Taniguchi, S. Ohtani, T. Takenobu, Y. Iwasa, and T. Arima, *Polarization Reversal in Multiferroic* $TbMnO_3$ *with a Rotating Magnetic Field Direction*, Phys. Rev. Lett. **99**, 227206 (2007).

[147] M. Nakamura, Y. Tokunaga, M. Kawasaki, and Y. Tokura, *Multiferroicity in an orthorhombic* $YMnO_3$ *single-crystal film*, Applied Physics Letters **98**, 082902 (2011).

[148] X. Martí, V. Skumryev, C. Ferrater, M. V. García-Cuenca, M. Varela, F. Sánchez, and J. Fontcuberta, *Emergence of ferromagnetism in antiferromagnetic* $TbMnO_3$ *by epitaxial strain*, Applied Physics Letters **96**, 222505 (2010).

[149] V. Skumryev, F. Ott, J. Coey, A. Anane, J.-P. Renard, L. Pinsard-Gaudart, and A. Revcolevschi, *Weak ferromagnetism in* $LaMnO_3$, The European Physical Journal B - Condensed Matter and Complex Systems **11**, 401 (1999).

[150] J. Perez-Mato, *Private communication* (2011).

[151] R. D. Shannon, *Revised effective ionic radii and systematic studies of interatomic distances in halides and chalcogenides*, Acta Crystallographica Section A **32**, 751 (1976).

[152] J. H. Liao, T. B. Wu, Y. T. Chen, and J. M. Wu, *Ferroelectric-field-induced spin-pinning effect in* $Pb(Zr_{0.5}Ti_{0.5})O_3/La_{0.9}Sr_{0.1}MnO_3$ *bilayers*, Journal of Applied Physics **101**, 09M110 (2007).

[153] Y. Chen, J. Wang, M. Liu, J. Lou, N. X. Sun, C. Vittoria, and V. G. Harris, *Giant magnetoelectric coupling and E-field tunability in a laminated* Ni_2MnGa*/lead-magnesium-niobate-lead titanate multiferroic heterostructure*, Applied Physics Letters **93**, 112502 (2008).

[154] Y.-C. Chen, T.-H. Hong, Z.-X. Jiang, and Q.-R. Lin, *Study on multiferroic properties in* $Ni_{80}Fe_{20}/BaTiO_3$ *bilayer films*, Journal of Applied

Physics **103**, 07E305 (2008).

[155] C. Israel, S. Kar-Narayan, and N. D. Mathur, *Converse magnetoelectric coupling in multilayer capacitors*, Applied Physics Letters **93**, 173501 (2008).

[156] H. F. Tian, T. L. Qu, L. B. Luo, J. J. Yang, S. M. Guo, H. Y. Zhang, Y. G. Zhao, and J. Q. Li, *Strain induced magnetoelectric coupling between magnetite and $BaTiO_3$*, Applied Physics Letters **92**, 063507 (2008).

[157] J. Lou, M. Liu, D. Reed, Y. Ren, and N. X. Sun, *Giant Electric Field Tuning of Magnetism in Novel Multiferroic FeGaB/Lead Zinc Niobate-Lead Titanate (PZN-PT) Heterostructures*, Advanced Materials **21**, 4711 (2009).

[158] Y. Chen, T. Fitchorov, C. Vittoria, and V. G. Harris, *Electrically controlled magnetization switching in a multiferroic heterostructure*, Applied Physics Letters **97**, 052502 (2010).

[159] S. Ryu, J. H. Park, and H. M. Jang, *Magnetoelectric coupling of [00l]-oriented $Pb(Zr_{0.4}Ti_{0.6})O_3$-$Ni_{0.8}Zn_{0.2}Fe_2O_4$ multilayered thin films*, Applied Physics Letters **91**, 142910 (2007).

[160] J.-P. Zhou, H. He, Z. Shi, and C.-W. Nan, *Magnetoelectric $CoFe_2O_4/Pb(Zr_{0.52}Ti_{0.48})O_3$ double-layer thin film prepared by pulsed-laser deposition*, Applied Physics Letters **88**, 013111 (2006).

[161] K. Tahmasebi, A. Barzegar, J. Ding, T. Herng, A. Huang, and S. Shannigrahi, *Magnetoelectric effect in $Pb(Zr_{0.95}Ti_{0.05})O_3$ and $CoFe_2O_4$ heteroepitaxial thin film composite*, Materials & Design **32**, 2370 (2011).

[162] X. Tang, J. Dai, X. Zhu, W. Song, and Y. Sun, *Magnetic annealing effects on multiferroic $BiFeO_3/CoFe_2O_4$ bilayered films*, Journal of Alloys and Compounds **509**, 4748 (2011).

[163] T. Wu, M. A. Zurbuchen, S. Saha, R.-V. Wang, S. K. Streiffer, and J. F. Mitchell, *Observation of magnetoelectric effect in epitaxial ferroelectric film/manganite crystal heterostructures*, Phys. Rev. B **73**, 134416 (2006).

[164] G. Srinivasan, E. T. Rasmussen, B. J. Levin, and R. Hayes, *Magnetoelectric effects in bilayers and multilayers of magnetostrictive and piezoelectric perovskite oxides*, Phys. Rev. B **65**, 134402 (2002).

[165] Y. G. Ma, W. N. Cheng, M. Ning, and C. K. Ong, *Magnetoelectric*

effect in epitaxial $Pb(Zr_{0.52}Ti_{0.48})O_3/La_{0.7}Sr_{0.3}MnO_3$ composite thin film, Applied Physics Letters **90**, 152911 (2007).

[166] R. Y. Zheng, J. Wang, and S. Ramakrishna, *Electrical and magnetic properties of multiferroic $BiFeO_3/CoFe_2O_4$ heterostructure*, Journal of Applied Physics **104**, 034106 (2008).

[167] I. Vrejoiu, M. Ziese, A. Setzer, P. D. Esquinazi, B. I. Birajdar, A. Lotnyk, M. Alexe, and D. Hesse, *Interfacial strain effects in epitaxial multiferroic heterostructures of $PbZr_xTi_{1-x}O_3/La_{0.7}Sr_{0.3}MnO_3$ grown by pulsed-laser deposition*, Applied Physics Letters **92**, 152506 (2008).

[168] X. Lu, Y. Kim, S. Goetze, X. Li, S. Dong, P. Werner, M. Alexe, and D. Hesse, *Magnetoelectric Coupling in Ordered Arrays of Multilayered Heteroepitaxial $BaTiO_3/CoFe_2O_4$ Nanodots*, Nano Letters **11**, 3202 (2011).

[169] K.-S. Chang, M. A. Aronova, C.-L. Lin, M. Murakami, M.-H. Yu, J. Hattrick-Simpers, O. O. Famodu, S. Y. Lee, R. Ramesh, M. Wuttig, I. Takeuchi, C. Gao, and L. A. Bendersky, *Exploration of artificial multiferroic thin-film heterostructures using composition spreads*, Applied Physics Letters **84**, 3091 (2004).

[170] W. Huang, J. Zhu, H. Zeng, X. Wei, Y. Zhang, Y. Li, and J. Hao, *Effect of strain on the ferroelectric properties in epitaxial perovskite titanate thin films grown on ferromagnetic $CoFe_2O_4$ layers*, Scripta Materialia **58**, 1118 (2008).

[171] P. S. S. R. Krishnan, M. Arredondo, M. Saunders, Q. M. Ramasse, N. Valanoor, and P. Munroe, *Microstructural analysis of interfaces in a ferromagnetic-multiferroic epitaxial heterostructure*, Journal of Applied Physics **109**, 034103 (2011).

[172] J. Zhu, L. Zhou, W. Huang, Y. Li, and Y. Li, *Study on the growth and interfacial strain of $CoFe_2O_4/BaTiO_3$ bilayer films*, Journal of Crystal Growth **311**, 3300 (2009).

[173] J. Zhang, J. Dai, W. Lu, and H. Chan, *Room temperature magnetic exchange coupling in multiferroic $BaTiO_3/CoFe_2O_4$; magnetoelectric superlattice*, Journal of Materials Science **44**, 5143 (2009).

[174] D. Mukherjee, T. Dhakal, R. Hyde, P. Mukherjee, H. Srikanth, and S. Witanachchi, *Role of epitaxy in controlling the magnetic and magnetostrictive properties of cobalt ferrite-PZT bilayers*, Journal of Physics

D: Applied Physics **43**, 485001 (2010).

[175] C. Deng, Y. Zhang, J. Ma, Y. Lin, and C.-W. Nan, *Magnetoelectric effect in multiferroic heteroepitaxial $BaTiO_3$-$NiFe_2O_4$ composite thin films*, Acta Materialia **56**, 405 (2008).

[176] V. M. Petrov and G. Srinivasan, *Enhancement of magnetoelectric coupling in functionally graded ferroelectric and ferromagnetic bilayers*, Phys. Rev. B **78**, 184421 (2008).

[177] F. Sánchez and N. Dix, *Structural properties of $BaTiO_3$-$CoFe_2O_4$bilayers on $SrTiO_3$*.

[178] M. Kawai, D. Kan, S. Isojima, H. Kurata, S. Isoda, Y. Shimakawa, S. Kimura, and O. Sakata, *Critical thickness control by deposition rate for epitaxial $BaTiO_3$ thin films grown on $SrTiO_3(001)$*, Journal of Applied Physics **102**, 114311 (2007).

[179] F. Rigato, *Epitaxial spinel ferrite films for spin polarized tunneling transport*, Ph.D. thesis, Universitat Autònoma de Barcelona (2010).

[180] N. A. Pertsev, A. G. Zembilgotov, and A. K. Tagantsev, *Effect of Mechanical Boundary Conditions on Phase Diagrams of Epitaxial Ferroelectric Thin Films*, Phys. Rev. Lett. **80**, 1988 (1998).

[181] L. Ben and D. C. Sinclair, *Anomalous Curie temperature behavior of A-site Gd-doped $BaTiO_3$ ceramics: The influence of strain*, Applied Physics Letters **98**, 092907 (2011).

[182] E. Bursian and E. Starov, *Lowering of phase transition temperature in heavily reduced $BaTiO_3$ crystals*, Soviet Physics Solid State,USSR **11**, 2423 (1970).

[183] I. Gul and A. Maqsood, *Structural, magnetic and electrical properties of cobalt ferrites prepared by the sol-gel route*, Journal of Alloys and Compounds **465**, 227 (2008).

[184] W. Heywang, *Semiconducting barium titanate*, Journal of Materials Science **6**, 1214 (1971).

[185] K. J. Choi, M. Biegalski, Y. L. Li, A. Sharan, J. Schubert, R. Uecker, P. Reiche, Y. B. Chen, X. Q. Pan, V. Gopalan, L.-Q. Chen, D. G. Schlom, and C. B. Eom, *Enhancement of Ferroelectricity in Strained $BaTiO_3$ Thin Films*, Science **306**, 1005 (2004).

[186] M. Dawber, C. Lichtensteiger, M. Cantoni, M. Veithen, P. Ghosez,

K. Johnston, K. M. Rabe, and J.-M. Triscone, *Unusual Behavior of the Ferroelectric Polarization in $PbTiO_3/SrTiO_3$ Superlattices*, Phys. Rev. Lett. **95**, 177601 (2005).

[187] M. Dawber, N. Stucki, C. Lichtensteiger, S. Gariglio, P. Ghosez, and J.-M. Triscone, *Tailoring the Properties of Artificially Layered Ferroelectric Superlattices*, Advanced Materials **19**, 4153 (2007).

[188] H. J. Kim, S. H. Oh, and H. M. Jang, *Thermodynamic theory of stress distribution in epitaxial $Pb(Zr,Ti)O_3$ thin films*, Applied Physics Letters **75**, 3195 (1999).

[189] G. Catalan, B. Noheda, J. McAneney, L. J. Sinnamon, and J. M. Gregg, *Strain gradients in epitaxial ferroelectrics*, Phys. Rev. B **72**, 020102 (2005).

[190] S.-H. Kim, H.-J. Woo, J. Ha, C. S. Hwang, H. R. Kim, and A. I. Kingon, *Thickness effects on imprint in chemical-solution-derived $(Pb,La)(Zr,Ti)O_3$ thin films*, Applied Physics Letters **78**, 2885 (2001).

[191] A. Hartmann, M. Neilson, R. Lamb, K. Watanabe, and J. Scott, *Ruthenium oxide and strontium ruthenate electrodes for ferroelectric thin-films capacitors*, Applied Physics A: Materials Science & Processing **70**, 239 (2000).

[192] T. Kudo, M. Tachiki, T. Kashiwai, and T. Kobayashi, *Band Diagram of Metal-Insulator-Magnetic Semiconductor ($La_{0.85}Sr_{0.15}MnO_3$) Structure at Room Temperature*, Japanese Journal of Applied Physics **37**, L999 (1998).

[193] M. Copel, P. R. Duncombe, D. A. Neumayer, T. M. Shaw, and R. M. Tromp, *Metallization induced band bending of $SrTiO_3(100)$ and $Ba_{0.7}Sr_{0.3}TiO_3$*, Applied Physics Letters **70**, 3227 (1997).

[194] L. J. Sinnamon, R. M. Bowman, and J. M. Gregg, *Investigation of dead-layer thickness in $SrRuO_3/Ba_{0.5}Sr_{0.5}TiO_3/Au$ thin-film capacitors*, Applied Physics Letters **78**, 1724 (2001).

[195] H. Zheng, J. Wang, L. Mohaddes-Ardabili, M. Wuttig, L. Salamanca-Riba, D. G. Schlom, and R. Ramesh, *Three-dimensional heteroepitaxy in self-assembled $BaTiO_3$-$CoFe_2O_4$ nanostructures*, Applied Physics Letters **85**, 2035 (2004).

[196] J. Li, I. Levin, J. Slutsker, V. Provenzano, P. K. Schenck, R. Ramesh,

J. Ouyang, and A. L. Roytburd, *Self-assembled multiferroic nanostructures in the $CoFe_2O_4$-$PbTiO_3$ system*, Applied Physics Letters **87**, 072909 (2005).

[197] I. Levin, J. Li, J. Slutsker, and A. Roytburd, *Design of Self-Assembled Multiferroic Nanostructures in Epitaxial Films*, Advanced Materials **18**, 2044 (2006).

[198] M. Murakami, S. Fujino, S.-H. Lim, L. G. Salamanca-Riba, M. Wuttig, I. Takeuchi, B. Varughese, H. Sugaya, T. Hasegawa, and S. E. Lofland, *Microstructure and phase control in Bi-Fe-O multiferroic nanocomposite thin films*, Applied Physics Letters **88**, 112505 (2006).

[199] H. Zheng, F. Straub, Q. Zhan, P.-L. Yang, W.-K. Hsieh, F. Zavaliche, Y.-H. Chu, U. Dahmen, and R. Ramesh, *Self-Assembled Growth of $BiFeO_3$-$CoFe_2O_4$ Nanostructures*, Advanced Materials **18**, 2747 (2006).

[200] H. Zheng, Q. Zhan, F. Zavaliche, M. Sherburne, F. Straub, M. P. Cruz, L.-Q. Chen, U. Dahmen, and R. Ramesh, *Controlling Self-Assembled Perovskite-Spinel Nanostructures*, Nano Letters **6**, 1401 (2006).

[201] J. Barbosa, B. G. Almeida, J. A. Mendes, A. G. Rolo, J. P. Araüjo, and J. B. Sousa, *Nanogranular $BaTiO_3$-$CoFe_2O_4$ thin films deposited by pulsed laser ablation*, Journal of Applied Physics **101**, 09M101 (2007).

[202] N. Dix, V. Skumryev, V. Laukhin, L. Fàbrega, F. Sánchez, and J. Fontcuberta, *Sputtering growth and characterization of $CoFe_2O_4$-$BaTiO_3$ nanostructures*, Materials Science and Engineering: B **144**, 127 (2007), eMRS 2007, Symposium H: Nanoscale Tailoring of Defect Structures for Optimized Functional and Multifunctional Oxide Films.

[203] M. Liu, X. Li, H. Imrane, Y. Chen, T. Goodrich, Z. Cai, K. S. Ziemer, J. Y. Huang, and N. X. Sun, *Synthesis of ordered arrays of multiferroic $NiFe_2O_4$-$Pb(Zr_{0.52}Ti_{0.48})O_3$ core-shell nanowires*, Applied Physics Letters **90**, 152501 (2007).

[204] S. Ren and M. Wuttig, *Spinodally synthesized magnetoelectric*, Applied Physics Letters **91**, 083501 (2007).

[205] J. Slutsker, Z. Tan, A. L. Roytburd, and I. Levin, *Thermodynamic aspects of epitaxial self-assembly and magnetoelectric response in multiferroic nanostructures*, Journal of materials research **22**, 2087 (2007).

[206] H. Zheng, J. Kreisel, Y.-H. Chu, R. Ramesh, and L. Salamanca-Riba,

Heteroepitaxially enhanced magnetic anisotropy in $BaTiO_3$-$CoFe_2O_4$ nanostructures, Applied Physics Letters **90**, 113113 (2007).

[207] R. Muralidharan, N. Dix, V. Skumryev, M. Varela, F. Sánchez, and J. Fontcuberta, *Synthesis, structure, and magnetic studies on self-assembled $BiFeO_3$-$CoFe_2O_4$ nanocomposite thin films*, Journal of Applied Physics **103**, 07E301 (2008).

[208] N. Dix, R. Muralidharan, J. Caicedo, D. Hrabovsky, I. Fina, L. Fàbrega, V. Skumryev, M. Varela, J. Guyonnet, P. Paruch, F. Sánchez, and J. Fontcuberta, *Influence of substrate temperature in $BiFeO_3$-$CoFe_2O_4$ nanocomposites deposited on $SrTiO_3$ (001)*, Journal of Magnetism and Magnetic Materials **321**, 1790 (2009), selected papers from the Symposium F "Multiferroics and Magnetoelectrics Materials" of the E-MRS Conference.

[209] N. Dix, R. Muralidharan, J. Guyonnet, B. Warot-Fonrose, M. Varela, P. Paruch, F. Sánchez, and J. Fontcuberta, *On the strain coupling across vertical interfaces of switchable $BiFeO_3$-$CoFe_2O_4$ multiferroic nanostructures*, Applied Physics Letters **95**, 062907 (2009).

[210] N. Dix, R. Muralidharan, B. Warot-Fonrose, M. Varela, F. Sánchez, and J. Fontcuberta, *Critical Limitations in the Fabrication of Biferroic $BiFeO_3$-$CoFe_2O_4$ Columnar Nanocomposites Due to Bismuth Loss*, Chemistry of Materials **21**, 1375 (2009).

[211] K. Postava, D. Hrabovskŷ, O. Životskŷ, J. Pištora, N. Dix, R. Muralidharan, J. M. Caicedo, F. Sánchez, and J. Fontcuberta, *Magneto-optic material selectivity in self-assembled $BiFeO_3$-$CoFe_2O_4$ biferroic nanostructures*, Journal of Applied Physics **105**, 07C124 (2009).

[212] L. Yan, Z. Xing, Z. Wang, T. Wang, G. Lei, J. Li, and D. Viehland, *Direct measurement of magnetoelectric exchange in self-assembled epitaxial $BiFeO_3$-$CoFe_2O_4$ nanocomposite thin films*, Applied Physics Letters **94**, 192902 (2009).

[213] N. Dix, R. Muralidharan, J.-M. Rebled, S. Estradé, F. Peiró, M. Varela, J. Fontcuberta, and F. Sánchez, *Selectable Spontaneous Polarization Direction and Magnetic Anisotropy in $BiFeO_3$-$CoFe_2O_4$ Epitaxial Nanostructures*, ACS Nano **4**, 4955 (2010).

[214] I. Fina, N. Dix, L. Fàbrega, F. Sánchez, and J. Fontcuberta, *Effects of morphology and strain on the dielectric response of multiferroic*

$CoFe_2O_4$-$BaTiO_3$ nanocomposite thin films, Journal of Applied Physics **108**, 034108 (2010).

[215] Y. H. Hou, Y. J. Zhao, Z. W. Liu, H. Y. Yu, X. C. Zhong, W. Q. Qiu, D. C. Zeng, and L. S. Wen, *Structural, electronic and magnetic properties of partially inverse spinel $CoFe_2O_4$: a first-principles study*, Journal of Physics D: Applied Physics **43**, 445003 (2010).

[216] R. C. Casella and S. P. Keller, *Polarized Light Transmission of $BaTiO_3$ Single Crystals*, Phys. Rev. **116**, 1469 (1959).

[217] C. Li, Z. Chen, Y. Zhou, and D. Cui, *Effect of oxygen content on the dielectric and ferroelectric properties of laser-deposited $BaTiO_3$ thin films*, Journal of Physics: Condensed Matter **13**, 5261 (2001).

[218] J. Hiltunen, D. Seneviratne, H. Tuller, J. Lappalainen, and V. Lantto, *Crystallographic and dielectric properties of highly oriented $BaTiO_3$ films: Influence of oxygen pressure utilized during pulsed laser deposition*, Journal of Electroceramics **22**, 395 (2009).

[219] R. Waser, *Dielectric analysis of intergrated ceramic thin film capacitors*, Integrated Ferroelectrics **15**, 39 (1997).

[220] J. F. Ihlefeld, A. M. Vodnick, S. P. Baker, W. J. Borland, and J.-P. Maria, *Extrinsic scaling effects on the dielectric response of ferroelectric thin films*, Journal of Applied Physics **103**, 074112 (2008).

[221] T. Zhao, F. Chen, H. Lu, G. Yang, and Z. Chen, *Thickness and oxygen pressure dependent structural characteristics of $BaTiO_3$ thin films grown by laser molecular beam epitaxy*, Journal of Applied Physics **87**, 7442 (2000).

List of Figures

List of Tables

List of Tables

Glossary

Ferroics

- *Ferroelectric* materials possess a spontaneous polarization that is stable and can be switched hysteretically by an applied electric field.
- *Ferromagnetic* materials posses a spontaneous magnetization that is stable and can be switched hysteretically by an applied magnetic field; *antiferromagnetic* materials posses ordered magnetic moments that can cancel each other completely within each magnetic unit cell.

Ferroelectricity

- *Polarization*: amount of charge per area.
- *Saturation polarization*: polar state in a ferroelectric at which all the electric dipoles are pointing in the direction of an applied electric field.
- *Poling process*: it is that process that brings the ferroelectric to a polar state where the saturation polarization is reached by the application of an electric field.
- *Remanent polarization*: polarization in a ferroelectric at zero electric field, after poling the sample.
- *Coercive electric field*: electric field at which the polarization changes its sign in a ferroelectric.
- *Breakdown field*: electric field at which a dielectric is not more insulating and becomes conductive.

- *Retention time*: the time that a ferroelectric keeps its polarization in the remanent state.
- *Leakage*: is the common name for the current in a ferroelectric due to electronic transport. It is equivalent to the dielectric conductivity.
- *Fatigue*: or aging is the effect that a ferroelectric suffers after being cycled several times, yielding to a decrement in the polarization.

Order parameter coupling

- *Magnetoelectric* coupling describes the influence of a magnetic (electric) field on the polarization (magnetization) of a material.
- *Piezoelectricity* describes a change in strain as a linear function of applied electric field, or a change in polarization as a linear function of applied stress.
- *Piezomagnetism* describes a change in strain as a linear function of applied magnetic field, or a change in magnetization as a linear function of applied stress.
- *Electrostriction* describes a change in strain as a quadratic function of applied electric field.
- *Magnetostriction* describes a change in strain as a quadratic function of applied magnetic field.
- *Magnetoresitance* describes a change in conductivity as a function of applied magnetic field.

List of communications[6]

07/2011 *Efects of strain on the magnetoelectric behaviour of orthorhombic $YMnO_3$ thin films.* I. Fina, X. Martí, L. Fàbrega, F. Sánchez, and J. Fontcuberta. **ISIF 2011**, Cambridge, United Kingdom. Type: Oral.

07/2011 *Tailoring ferroelectricity in $CoFe_2O_4$-$BaTiO_3$ bilayers.* I. Fina, N. Dix, R. Bachelet, L. Fàbrega, F. Sánchez, and J. Fontcuberta. **EMF 2011**, Cambridge, United Kingdom. Type: Poster.

07/2011 *Ferroelectric switching and cycloidal order in o-$YMnO_3$ thin films.* I. Fina, X. Martí, L. Fàbrega, F. Sánchez, and J. Fontcuberta. **ISIF 2011**, Cambridge, United Kingdom. Type: Poster.

06/2011 *Ferroelectricity and Strain Effects in Orthorhombic $YMnO_3$ Thin Films.* I. Fina, X. Martí, L. Fàbrega, F. Sánchez, and J. Fontcuberta. **EMF 2011**, Bordeaux, France. Type: Oral.

06/2011 *Magnetic switching of electric polarization in multiferroic thin films.* I. Fina, L. Fàbrega, F. Sánchez, V. Skumryev, X. Martí and J. Fontcuberta. **Nanoselect 2011**, Sant Feliu de Guíxols, Spain. Type: Oral.

06/2011 *Ferroelectricity and Strain Effects in Orthorhombic $YMnO_3$ Thin Films.* I. Fina, X. Martí, L. Fàbrega, F. Sánchez, and J. Fontcuberta. **EMF 2011**, Bordeaux, France. Type: Poster.

06/2011 *Ferroelectric Switching and Cycloidal Order in $YMnO_3$ Thin Films.* I. Fina, L. Fàbrega, X.Martí, F. Sánchez and J. Fontcuberta. **EMF 2011**, Bordeaux, France. Type: Poster.

[6] As presenting author.

06/2011 *Ferroelectric Properties of $CoFe_2O_4$-$BaTiO_3$ Bilayers.* I. Fina, N. Dix, R. Brachelet, L. Fàbrega, F. Sánchez, and J. Fontcuberta. **EMF 2011**, Bordeaux, France. Type: Poster.

06/2011 *Ferroelectricity and strain effects in orthorhombic $RMnO_3$ thin films.* I. Fina, X. Martí, L. Fàbrega, F. Sánchez, and J. Fontcuberta. **Nanoselect 2011**, Sant Feliu de Guíxols, Spain. Type: Poster.

06/2011 *Ferroelectric properties of multiferroic $CoFe_2O_4$-$BaTiO_3$ layered heterostructures.* I. Fina, N. Dix, R. Bachelet, L. Fàbrega, F. Sánchez, and J. Fontcuberta. **Nanoselect 2011**, Sant Feliu de Guíxols, Spain. Type: Poster.

08/2010 *Ferroelectricity and magnetoelectric coupling in strain engineered orthorhombic $YMnO_3$ epitaxial thin film.* I. Fina, L. Fàbrega, X. Martí, F. Sánchez and J. Fontcuberta. **ISAF-ECAPD 2010**, Edinburgh, United Kingdom. Type: Oral.

08/2010 *Nonferroelectric contributions to the hysteresis cycles in manganite thin films: A comparative study of measurement techniques* . I. Fina, L. Fàbrega, X. Martí, E. Langenberg, N.Dix, F. Sànchez, M. Varela and J. Fontcuberta. **ISAF-ECAPD 2010**, Edinburgh, United Kingdom. Type: Poster.

08/2010 *Ferroelectric properties of $LuMnO_3$ single crystals.* I. Fina, L. Fàbrega, V. Skumryev, V. Laukhin, M. Gospodinov and J. Fontcuberta. **ISAF-ECAPD 2010**, Edinburgh, United Kingdom. Type: Poster.

07/2010 *Low temperature characterization of ferroelectric $LuMnO_3$ single crystals.* I. Fina, L. Fàbrega, V. Skumryev, V. Laukhin, M. Gospodinov, J. Fontcuberta. **Nanoselect 2010**, St. Feliu de Guixols, Spain. Type: Poster.

10/2009 *Control of magnetic and dielectric properties by epitaxial strain in orthorhombic $TbMnO_3$ and $YMnO_3$.* X. Marti, I. Fina, F. Sánchez, L. Fàbrega, and J. Fontcuberta.**WOE2009**, Tarragona, Spain. Type: Poster.

09/2009 *Control of magnetic and dielectric properties by epitaxial strain in orthorhombic $YMnO_3$ films.* I. Fina, X. Martí, F. Sánchez , L. Fàbrega, V. Skumryev, C. Ferreter, M.Varela y J. Fontcuberta. **3rd European School on Multiferroics**, Groningen, Holland. Type: Poster.

07/2009 *Dielectric anomalies and impedance spectroscopy in multiferroic o-$YMnO_3$ thin films.* I. Fina, X. Martí, L. Fàbrega, F. Sánchez y J. Fontcuberta. **Nanoselect 2009**, Manresa, Spain. Type: Poster.

07/2009 *Effects of morphology and strain on the dielectric permittivity of multiferroic $CoFe_2O_4$-$BaTiO_3$ nanocomposites.* I. Fina, N. Dix, V. Laukhin, L. Fàbrega, F. Sánchez and J. Fontcuberta. **Nanoselect 2009**, Manresa, Spain. Type: Poster.

06/2009 *Dielectric and magnetic characterization of multiferroic $CoFe_2O_4$-$BaTiO_3$ nanocomposites.* I. Fina , N. Dix, L. Fàbrega, F. Sánchez y J. Fontcuberta. **EMRS 2009 Spring Meeting**, Strasbourg, France. Type: Oral.

06/2009 *Dielectric anomaly and magnetocapacitance in orthorhombic YMO_3.* I. Fina, X. Martí, L. Fàbrega, F. Sánchez y J. Fontcuberta. **EMRS 2009 Spring Meeting**, Strasbourg, France. Type: Poster.

09/2008 *Dielectric properties of $CoFe_2O_4$-$BaTiO_3$ nanocomposite thin films.* I. Fina, N. Dix, V. Laukhin, L. Fàbrega, F. Sánchez y J. Fontcuberta. **2nd European School of Multiferroics**, Girona, Spain. Type: Poster.

05/2008 *Magnetic and electric properties of $CoFe_2O_4$-$BaTiO_3$ nanocomposite thin films.* I. Fina, N. Dix, V. Skumryev, L. Fàbrega, F. Sánchez y J. Fontcuberta. **EMRS 2008 Spring Meeting**, Strasbourg, France. Type: Poster.

List of publications

- E. Langenberg, I. Fina, P. Gemeiner, B. Dkhil, L. Fàbrega, M. Varela, and J. Fontcuberta, *Ferroelectric phase transition in strained multiferroic* $(Bi_{0.9}La_{0.1})_2NiMnO_6$ *thin films*, Applied Physics Letters **100**, 022902 (2012)
- I. Fina, L. Fàbrega, X. Martí, F. Sánchez, and J. Fontcuberta, *Chiral Domains in Cycloidal Multiferroic Thin Films: Switching and Memory Effects*, Phys. Rev. Lett. **107**, 257601 (2011)
- I. Fina, L. Fàbrega, E. Langenberg, X. Martí, F. Sánchez, M. Varela, and J. Fontcuberta, *Nonferroelectric contributions to the hysteresis cycles in manganite thin films: A comparative study of measurement techniques*, Journal of Applied Physics **109**, 074105 (2011)
- J. Fontcuberta, I. Fina, L. Fàbrega, F. Sánchez, X. Martí, and V. Skumryev, *Ferroelectricity and strain effects in orthorhombic* $YMnO_3$ *thin films*, Phase Transitions **84**, 555 (2011)
- V. Skumryev, V. Laukhin, I. Fina, X. Martí, F. Sánchez, M. Gospodinov, and J. Fontcuberta, *Magnetization Reversal by Electric-Field Decoupling of Magnetic and Ferroelectric Domain Walls in Multiferroic-Based Heterostructures*, Phys. Rev. Lett. **106**, 057206 (2011)
- I. Fina, N. Dix, L. Fàbrega, F. Sánchez, and J. Fontcuberta, *Effects of morphology and strain on the dielectric response of multiferroic* $CoFe_2O_4$–$BaTiO_3$ *nanocomposite thin films*, Journal of Applied Physics **108**, 034108 (2010)
- I. Fina, N. Dix, L. Fàbrega, F. Sánchez, and J. Fontcuberta, *Magnetocapacitance in* $BaTiO_3$-$CoFe_2O_4$ *nanocomposites*, Thin Solid Films

518, 4634 (2010), proceedings of the EMRS 2009 Spring Meeting Symposium H: Synthesis, Processing and Characterization of Nanoscale Multi Functional Oxide Films II

- I. Fina, L. Fàbrega, X. Martí, F. Sánchez, and J. Fontcuberta, *Magnetic switch of polarization in epitaxial orthorhombic $YMnO_3$ thin films*, Applied Physics Letters **97**, 232905 (2010)
- I. Fina, X. Martí, L. Fàbrega, F. Sànchez, and J. Fontcuberta, *Dielectric anomalies in orthorhombic $YMnO_3$ thin films*, Thin Solid Films **518**, 4710 (2010), proceedings of the EMRS 2009 Spring Meeting Symposium H: Synthesis, Processing and Characterization of Nanoscale Multi Functional Oxide Films II
- J. Ventura, I. Fina, C. Ferrater, E. Langenberg, L. Coy, M. Polo, M. García-Cuenca, L. Fàbrega, and M. Varela, *Structural and dielectric properties of (001) and (111)-oriented $BaZr_0.2Ti_0.8O_3$ epitaxial thin films*, Thin Solid Films **518**, 4692 (2010), proceedings of the EMRS 2009 Spring Meeting Symposium H: Synthesis, Processing and Characterization of Nanoscale Multi Functional Oxide Films II
- N. Dix, R. Muralidharan, J. Caicedo, D. Hrabovsky, I. Fina, L. Fàbrega, V. Skumryev, M. Varela, J. Guyonnet, P. Paruch, F. Sánchez, and J. Fontcuberta, *Influence of substrate temperature in $BiFeO_3$-$CoFe_2O_4$ nanocomposites deposited on SrTiO3 (0 0 1)*, Journal of Magnetism and Magnetic Materials **321**, 1790 (2009), selected papers from the Symposium F *Multiferroics and Magnetoelectrics Materials* of the E-MRS Conference
- I. Fina, N. Dix, V. Laukhin, L. Fàbrega, F. Sánchez, and J. Fontcuberta, *Dielectric properties of $BaTiO_3$-$CoFe_2O_4$ nanocomposite thin films*, Journal of Magnetism and Magnetic Materials **321**, 1795 (2009), selected papers from the Symposium F *Multiferroics and Magnetoelectrics Materials* of the E-MRS Conference
- E. Langenberg, M. Varela, M. García-Cuenca, C. Ferrater, M. Polo, I. Fina, L. Fàbrega, F. Sánchez, and J. Fontcuberta, *Epitaxial thin films of $(Bi_0.9La_0.1)_2NiMnO_6$ obtained by pulsed laser deposition*, Journal of Magnetism and Magnetic Materials **321**, 1748 (2009), selected papers from the Symposium F *Multiferroics and Magnetoelectrics Materials* of the E-MRS Conference

- X. Marti, I. Fina, V. Skumryev, C. Ferrater, M. Varela, L. Fabrega, F. Sánchez, and J. Fontcuberta, *Strain tuned magnetoelectric coupling in orthorhombic $YMnO_3$ thin films*, Applied Physics Letters **95**, 142903 (2009)